Functionalized carbon materials for high performances of PEM fuel cells

Yuzhen Xia

École doctorale RP2E

Laboratoire LRGP - UPR 3349

Carbone Fonctionnalisé pour Une Meilleure Performance des Piles à Combustible

Thèse

soutenue publiquement le 16/10/2014

pour l'obtention du diplôme de

Doctorat de l'Université de Lorraine

(spécialité génie des procédés et des produits)

par

Yuzhen XIA

Composition du jury

M. Dominique Bégin	ICPEES, Strasbourg	Rapporteur
M. Boniface Kokoh	IC2MP, Poitiers	Rapporteur
Mme. Deborah Jones	ICGM, Montpellier	Examinateur
M. Sébastien Fontana	IJL, Nancy	Examinateur
M. Gaël Maranzana	LEMTA, Nancy	Examinateur
Mme. Caroline Bonnet	LRGP, Nancy	Co-directrice de thèse, Invitée
M. François Lapicque	LRGP, Nancy	Directeur de thèse

École doctorale RP2E

Laboratoire LRGP - UPR 3349

Functionalized carbon materials for higher performances of PEM fuel cells

Thesis

presented publicly on 16/10/2014

to obtain the diplome of

PHD of Lorraine University

(Specialty engineering process and product)

by

Yuzhen XIA

Composition of the jury

Mr. Dominique Bégin	ICPEES, Strasbourg	Reviewer
Mr. Boniface Kokoh	IC2MP, Poitiers	Reviewer
Mrs. Deborah Jones	ICGM, Montpellier	Examiner
Mr. Sébastien Fontana	IJL, Nancy	Examiner
Mr. Gaël Maranzana	LEMTA, Nancy	Examiner
Mrs. Caroline Bonnet	LRGP, Nancy	Co-director of thesis, Invited
Mr. François Lapicque	LRGP, Nancy	Director of thesis

Résumé

Une pile à combustible est un dispositif électrochimique qui convertit en continu et directement l'énergie chimique d'un combustible en énergie électrique et en chaleur. La première pile à combustible a été inventée par William Grove en 1839, qui s'est inspiré de ses travaux sur l'électrolyse de l'eau en hydrogène et en oxygène, sont produits en consommant de l'électricité. En appliquent le principe inverse, la consommation en hydrogène et oxygène génère de l'électricité et de l'eau. Bien plus tard, des recherches ont été lancées sur la pile à combustible dont différents types ont été fabriqués.

Au début des années 1960, la pile à combustible de type membrane échangeuse de protons (PEMFC, proton exchange membrane fuel cell) a été inventée par des chercheurs de General Electric, qui a développé une membrane de polymère solide en tant qu'électrolyte. Les membranes Nafion®, fabriquées par DuPont en 1966, ont été utilisées pour remplacer celles en polystyrène sulfoné. La PEMFC, opérant à des températures inférieures à 100 ^{o}C, représente une voie prometteuse en raison du rendement élevé, de la conversion énergétique, du faible impact sur l'environnement. Le système ne produit pas de déchets, mais uniquement de l'eau. Toutefois, en raison du coût élevé, il a été limité à des missions spatiales et d'autres applications spéciales. Cependant, cette technologie se heurte à de nombreux problèmes relevant de la durabilité et des coûts d'investissement. Les recherches ont été effectuées afin de développer et d'optimiser ce dispositif tout en minimisant les coûts.

Au cours d'une réaction de la PEMFC, le combustible (hydrogène) et le comburant (air ou oxygène) alimentent chaque compartiment de la pile. Ils passent à travers la couche de diffusion de gaz (gas diffusion layer, GDL) et réagissent sur la couche de catalyseur (catalyst layer, CL). L'oxydation du combustible produit les électrons passant par un circuit externe et des ions H^{+} traversant la membrane électrolytique. Du côté cathodique, les électrons se recombinent avec les protons et les molécules d'oxygène pour former de l'eau.

La GDL sert comme matériau support des catalyseurs dans la préparation de l'électrode à diffusion de gaz (gas diffusion electrode, GDE). Sa nature poreuse

assure la bonne distribution des gaz depuis les canaux de distribution jusqu'aux sites catalytiques. De plus, ses propriétés hydrophobes assurent à la membrane une bonne hydratation tout en prévenant le noyage des électrodes. La GDL, à base de matériaux carbonés, possède une bonne conductivité électronique; une perméabilité de gaz élevée, et haute stabilité chimique et électrochimique. La structure macroporeuse de la GDL est assurée par un tissu, un feutre ou un papier de carbone. Les dernières générations de GDL sont généralement bicouches: une couche microporeuse est déposée sur la couche macroporeuse. Un agent hydrophobe, par exemple, le poly-tétrafluoroéthylène (polytetrafluoroethylene, PTFE), permet d'augmenter l'hydrophobicité de ces matériaux.

La CL est le lieu où les réactions d'oxydo-réduction se produisent. L'encre de catalyseur, contenant du liant, un électrocatalyseur et des solvants, est déposée sur un substrat, GDL ou membrane. Le liant joue un rôle important dans la détermination de la performance de l'électrode. Tout d'abord, il est utilisé pour fixer le catalyseur sur le support, pour maintenir l'intégrité de la structure d'électrode, qui concerne ainsi les propriétés mécaniques de la CL et la perméabilité aux gaz dans l'électrode. L'activité électrochimique de la CL est également influencée par les propriétés du liant. Le PTFE est utilisé comme un liant neutre classiquement utilisé. Cependant, en raison du caractère hydrophobe du PTFE, le catalyseur couvert est imperméable aux protons. L'utilisation du catalyseur dans la réaction électrochimique est réduite. Le Nafion, avec une conductivité protonique élevée et une bonne stabilité mécanique et chimique, est communément utilisé. La presence du Nafion permet d'augmenter l'activité catalytique et contribue également à retenir l'humidité de la membrane, en particulier à des hautes densités de courant. Cependant, le Nafion ne couvre qu'une partie du platine, par suite l'autre partie de catalyseur n'est pas accessible aux protons. Par ailleurs, un excès excessif de Nafion limite le transport de l'oxygène. De nombreux travaux ont été effectués afin d'optimiser la quantité de Nafion dans la CL. Cependant, une quantité optimale n'a pas pu être définie.

Le platine (Pt) et les alliages de Pt sont les catalyseurs les plus couramment utilisés du fait de leur grande activité catalytique, stabilité chimique et densité de courant d'échange (i_0) élevé. Les particules de platine finement divisées, de l'ordre de quelques nanomètres de diamètre, sont déposées sur des matériaux carbonés ayant une grande surface spécifique. Cependant, la pénurie mondiale de Pt contribue au prix élevé de la pile à combustible. Un certain nombre d'études ont été menées afin d'améliorer les activités catalytiques tout en diminuant les quantités: la diminution de la taille de nanoparticules, le développement d'alliages métalliques (en tant que

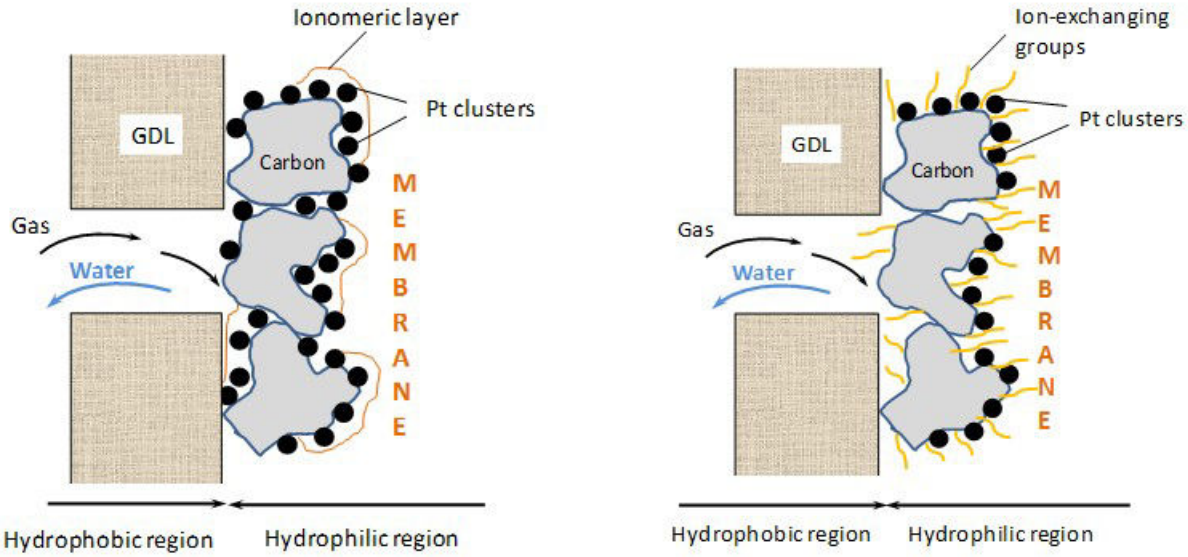

Figure 1: Schéma du catalyseur sulfoné dans la couche catalytique

binaire et ternaire), d'électrocatalyseurs sans Pt, et les particules de Pt dispersées sur les matériaux carbonés conducteurs et poreux.

Des particules de platine dispersées sur du carbone sont généralement utilisées dans les piles à combustible à basse température. Les propriétés des supports carbonés ont une influence forte sur les performances des catalyseurs métalliques supportés. La structure du carbone joue un rôle important dans l'accès des réactifs aux sites catalytiques et le retrait des produits de réaction. Les noirs de carbone (carbon black, CB) sont les supports les plus utilisés pour le Pt et les catalyseurs Pt-alliage, en raison de leur stabilité, de leur bonne conductivité électronique, de leur grande surface, de leur faible coût ainsi que leur disponibilité facile.

Le traitement chimique de la surface du support de carbone permet d'augmenter son activité, en introduisant des groupes fonctionnels ou des polymères sur la surface. Le greffage du support a également un effet sur le caractère hydrophobe / hydrophile des matériaux et sur l'activité électrochimique des catalyseurs. La sulfonation du carbone, qui confère une conductivité ionique au carbone, en plus de la conductivité électronique du carbone, a été pensée comme une voie prometteuse en remplacement du Nafion ajouté pour de la préparation de l'électrode. La présence des groupements sulfonates greffés facilite le transport des protons au cours des réactions de piles à combustible, en améliorant l'accessibilité des protons au platine. Ainsi, le greffage rend l'utilisation de Nafion moins nécessaire, comme illustré par la Figure 1.

Au cours de notre travail, deux types de Pt/Vulcan catalyseurs sulfonés ont été

greffés soit avec du polystyrène sulfonâtes (polymer styrene sulfonate acid, PSSA) soit avec de l'acide 4-phenysulfonique (phenysulfonic acid, PSA). La synthèse de ces matériaux carbonés a été menée à l'Institut Jean Lamour (CNRS-Université de lorraine) à Nancy. Les images de la microscopie électronique en transmission (transmission electron microscopy, TEM) et la diffractométrie de rayons X (X-ray diffraction, XRD) ont montré que la dispersion du platine sur le support n'était pas modifiée après la sulfonation.

L'influence du ratio de greffage, de la qualité de Nafion et du type de GDL a été étudiée en demi-piles et en pile à combustible. Deux types de support carboné, un papier carboné (carbon papaer, CP) ou un papier carboné en couche micro-poreuse (microporous layer coated carbon paper, MCP) ont été utilisés dans la fabrication de disques de demi-pile. La quantité du Nafion ajouté a varié de 0.25 à 0.50 $mg{\cdot}cm^{-2}$.

La demi-pile préparée par pressage à chaud sur un côté de la membrane, a été édutiée dans un système à trois électrodes. La contre-électrode est une feuille de Pt. Une électrode au sulfate mercureux saturé Hg/Hg_2SO_4 placée dans un capillaire Luggins est utilisée comme l'électrode de référence. L'électrolyte liquide, 0.5M de H_2SO_4, alimente en protons, en particulier la réduction d'oxygène. Par la suite, des assemblage membrane-electrodes (AMEs) avec des composants différents ont été préparés et testés en pile complète.

Les méthodes électrochimiques, telles que la voltammétrie cyclique (cyclic voltammetry, CV), la voltammétrie linéaire (linear sweep voltmmetry, LSV), la chronopotentiométrie et la spectroscopie d'impédance électrochimique (electrochemical impedance spectra, EIS), ont été utilisées pour caractériser ces matériaux.

La CV nous permet d'étudier le processus d'adsorption/ désorption de l'hydrogène sur le platine. Ainsi, la surface électrochimique (electrochemical surface area, ECSA) du catalyseur peut être estimée. L'air est fourni au système du côté de la GDL, et les protons traversant la membrane Nafion assurent la réduction de l'oxygène à la CL, en présence du catalyseur. Différentes performances ont été observées par les méthodes de LSV et EIS.

- Type de GDL

L'ECSA des demi-piles a été améliorée en présence de MCP. Concernant la performance de la réduction de l'oxygène (oxygen reduction reaction, ORR), les courbes LSV ont montré que les MCP-électrodes ont une densité de courant supérieure à celles sans MCP. Par ailleurs, les spectres d'impédance ont montré que la résistance au transfert de charge facilement observables de Nyquist des demi-piles préparées avec MCP, confirment les résultats de LSV.

- Catalyseurs greffé du PSSA

Pt/Vulcan catalyseurs ont été greffés des chaines PSSA par polymérisation radicalaire du 5, 10 et 20 wt.% (en masse de catalyseur) 4-styrènesulfonate de sodium. Les performances en demi-pile ont été améliorées par le greffage de 5 ou 10 wt.% PSSA. Cependant, la densité de courant ORR a diminué quand le ratio atteignait à 20 wt.%, inférieur à celle du catalyseur non-fonctionnalisé; les valeurs de la résistance de transfert de charge et de la résistance de diffusion étaient supérieures. Dans les tests en pile, des résultats élevés ont été obtenus après la sulfonation du catalyseur avec 5 et 10 wt.% PSSA, tandis que le greffage avec 20 wt.% PSSA n'a pas bénéficié d'amélioration dans la pile à combustible. L'hydrophilie des catalyseurs greffés avec 20 wt.% PSSA était plus élevée, ce qui a entraîné l'accumulation de l'eau dans l'électrode et gêné le transfert de réactif.

- Catalyseurs greffé du PSA

Dans l'essai en demi-pile, la valeur de l'ECSA a également réduite à cause du greffage de 11.6 et 23.3 wt.% PSA dans le catalyseur. Le catalyseur Pt/Vulcan greffé avec PSA présente un courant d'ORR inférieur à celui obtenu par le catalyseur non-fonctionnalisé. En la présence de MCP, une quantité de 23.3 wt.% PSA greffé sur Pt/Vulcan catalyseur s'avère être meilleure qu'avec des teneurs en PSA plus faibles, 11.6 wt.%. Un courant d'échange plus élevé a être obtenu en LSV, avec une plus faible pente de Tafel. Le diamètre de la boule de Nyquist était inférieur à celui des autres demi-piles. Des AMEs avec 5.8, 11.6, 18.0 et 23.3 wt.% PSA greffé sur le catalyseur ont été étudiés dans une pile à température ambiante. Leurs performances ont été améliorées par la sulfonation. L'AME, ayant des catalyseurs greffé avec 18.0 wt.% PSA et 0.50 mg·cm^{-2} Nafion, a présenté une densité de puissance plus élevée, de 223 mW·cm^{-2}. Sa performance de vieillissement a été étudiée dans 3000 cycles de CV entre 0.1 et 0.9 V. Les courbes de polarisation ont présentées une densité de puissance environ 311 mW·cm^{-2}après 3000 cycles, près de la valeur maximum, 318 mW·cm^{-2} après 1750 cycles.

- Quantité de Nafion

Dans les deux séries des catalyseurs, il y avait une concordance raisonnable dans l'effet du Nafion: moins de Nafion a entraîné une plus faible performance des demi-piles. Contrairement aux résultats obtenus en demi-pile, les AMEs ayant des catalyseurs greffé de 10 et 20 wt.% de PSSA, ont obtenu une densité de puissance plus élevée lors que la quantité de Nafion a diminué de 0.50 à 0.25 mg·cm^{-2}. Les AMEs sulfonés ayant

0.25 mg·cm^{-2} Nafion ont montré une densité de puissance élevé que celui présentant du catalyseur non-fonctionnalisé.

En raison de la présence de PSA ou PSSA, les performances des piles à combustible ont été améliorées. Un meilleur résultat a été obtenu dans les AMEs ayant 0.25 mg·cm^{-2} Nafion par la sulfonation de catalyseurs.

Contents

List of Figures

List of Tables

List of Acronyms

Abbreviations

ADT	Accelerated Durability Test
CBs	Carbon Blacks
CE	Counter Electrode
CL	Catalyst Layer
CPE	Constant Phase element
CV	Cyclic Voltammetry
CP	Cabon Paper
EIS	Electrochemical Impedance Spectra
GDL	Gas Diffusion Layer
GDE	Gas Diffusion Electrode
HOR	Hydrogen Oxidation Reaction
LSV	Linear Sweep Voltammetry
MCP	Micro-porous layered Carbon Paper
MEA	Membrane Electrode Assembly
NHE	Normal Hydrogen Electrode
OCV	Open Circuit Voltage
ORR	Oxygen Reduction Reaction
PEM	Polymer Eletrolyte Membrane
PSSA	Polymer Styrene Sulfonate Acid
PSA	4-phenysulfonic acid
RE	Reference Electrode
TEM	Transmission Electron Microscopy
WE	Working Electrode
XRD	X-Ray Diffraction

Symbols

α	electron transfer coefficient	
b	Tafel slope	mV/dec
C_{eq}	equivalent double layer capacity	mF·cm^{-2}
E_{act}	activation energy	kJ·mol^{-1}
E^0	equilibrium potential	mV
E_r	real potential	mV
E_m	measurement potential	mV
$ECSA$	electrochemical surface area	m^2·g^{-1}catalyst
f_{top}	frequency at the top of the EIS loop	Hz
F_{air}	flow rate of air	mol/s or ml/min
F_{H_2}	flow rate of hydrogen	mol/s or ml/min
G_f	Gibbs free energy	kJ·mol^{-1}
H	enthalpy	kJ·mol^{-1}
i	current density	mA·cm^{-2}
i_{ox}	current density of oxydation reaction	mA·cm^{-2}
i_{ox}	current density of reduction reaction	mA·cm^{-2}
i_0	exchange current density	mA·cm^{-2}
$i_0^\star$	exchange current density at infinite temperature	mA·cm^{-2}
$i_0^{apparent}$	apparent exchange current density	mA·cm^{-2}
I	current	A
J_{H_2}	hydrogen crossover rate	mol·s^{-1}·cm^{-2}
L_{Pt}	Pt loading	g·cm^{-2}
n	number of electrons	
n	pulsation	rad·s^{-1}
P	pressure	Pa
P_H	saturated vapor pressure in the humidifier	Pa
P_W	saturated vapor pressure in the fuel cell	Pa
P_{Pt}	weight percentage of platinum in carbon	wt.%
Q	pseudo capacity	F·rad^{1-n}·s^{1-n}
Q_H	Hydrogen adsorption/ desorption charge	mC·cm^{-2}
T	temperature	K
ϕ	efficiency of the cell	%
ϕ_H	relative humidification	%
ψ	phase	rad

η	overpotential	mV
r	radium of platinum particles	m
ρ	density of platinum	$g{\cdot}cm^{-3}$
R_{ct}	charge transfer resistance	$\Omega{\cdot}cm^2$
R_d	diffusion resistance	$\Omega{\cdot}cm^2$
R_{loop}	loop resistance	$\Omega{\cdot}cm^2$
R_m	membrane resistance	$\Omega{\cdot}cm^2$
R_{por}	porosity resistance	$\Omega{\cdot}\ cm^2$
R_Ω	ohmic resistance	$\Omega{\cdot}cm^2$
S_{tot}	total surface area	$m^2{\cdot}g^{-1}$catalyst
τ_d	characteristic diffusion time	s
u_{Pt}	platinum utilisation	%
w	pulsation	$rad{\cdot}s^{-1}$
λ_{air}	stoichiometric rate of air	
λ_{H_2}	stoichiometric rate of H_2	
Z_{CPE}	CPE impedance	$\Omega{\cdot}cm^2$
Z_W	diffusion impedance	$\Omega{\cdot}cm^2$

Constant

F	Faraday constant	96485 C·mol^{-1}
R	universal gas constant	8.314 J·(mol·K)$^{-1}$

Introduction

A fuel cell is an electrochemical device that continuously and directly converts the chemical energy of externally supplied fuel and oxidant to electrical energy. The first fuel cell was invented by Sir William Grove, by electrolyzing water into hydrogen and oxygen and then observing the reaction in reverse with the right catalyst, producing electricity. After that, researches have been started on practical fuel cell. During this period, coal, the major fuel at that time, was used to replace hydrogen and resulted in the invention of alkaline fuel cells and molten carbonate fuel cells [1].

PEM fuel cell, polymer electrolyte membrane fuel cell or proton exchange membrane fuel cell, was invented at General Electric in the early 1960s. They successfully developed a solid polymer membrane as the electrolyte. Initially, sulfonated polystyrene membranes were used as the solid electrolytes, but these were soon replaced by Nafion® membranes in 1966, which has been proved to be superior in performance and durability, and it is still the most popular membrane in use today. After, PEM fuel cell technology served as a part of NASA's Gemini Program. It was superior to other power converting devices because of its high power and energy densities, simple design, minimum noise and vibration, and reliability. The system produced no waste: only water. However, due to the high cost, it was limited to space missions and other special applications [1, 2, 3].

Fuel cell research and development then remained dormant for about 20 years due to technological obstacles and cost issues. Up to 1980s, many fuel cell companies have been founded. Today, more and more universities and institutes all over the world are becoming involved in PEM fuel cell research and development. So far several key innovations, such as low platinum catalyst loading, novel membranes, and new bipolar plates, make the application of PEM fuel cell systems more or less realistic. Demonstration activities in every corner of the world are overwhelming.

The catalyst, prepared by dispersing small particles of platinum or platinum-based alloy particles on the surface of a carbon support, such as Vulcan, is generally adopted as the electrocatalysts for PEM fuel cells. Much works on preparation of electrodes

with high platinum utilization and sufficient catalytic activity in the reaction have been taken. Besides the discussion of the optimum size of the Pt size particles, it is generally believed that a good carbon support can enhance the catalytic activities and mass transfer. Sulfonation of carbon structures, providing an electronic conductivity of the catalysts have been thought as a promising way. Based on this, the necessity of Nafion ionomer to be added in the preparation of the catalyst layer was reduced.

This research in functionalized carbon materials for efficient PEM fuel cell is a part of the collaboration project "FOCUS", funded by ICEEL (Institut Carnot pour l'Energie et l'Environnement en Lorraine). It has been accomplished in three CNRS-funded laboratories in Nancy. The functionalization of the carbon materials and the preparation of the electrodes are carried out in Institute Jean Lamour (IJL). Functionalization has been considered by sulfonating the carbon support (Vulcan) by two ways: (i) grafting polystyrene sulfonate acid (PSSA) by in situ polymerization of the ionomer; (ii) grafting phenysulfonic acid (PSA) group by the diazonimum synthesis route. This will allow observing the effect of the chain length of the grafted sulfonate.

Moreover, water management at the local state is investigated in the terms of adsorption isotherm and dynamics of the transfer in Laboratory of Theoretical and Applied Energetics and Mechanics (LEMTA). Our work in LRGP (Laboratoire Réactions et Génie des Procédés) concerns the electrochemical characterization of the half cells and fuel cells, together with the observation of aging of the electrodes of a novel technology.

The PhD work consists of four chapters, in addition to general introduction and conclusion. The first chapter introduces the fundamental aspects of fuel cells, including various components of PEM fuel cells, before giving literature data of carbon materials as support of the catalyst and the investigation mode. The second chapter describes the materials and the methods used and developed in this work: functionalized catalysts, half-cell, fuel cell and their installation in the bench, together with the various electrochemical techniques that have been employed to characterize the performance and to describe of the novel material. The third part is dedicated to PSSA grafted carbon catalysts, with the experimental data of the numerous tests with the half-cell, the performances of the materials in the fuel cells and durability tests of the promising materials in fuel cells. Finally, chapter 4 follows the same outline for the second type of the carbon material: the PSA grafted carbon materials, which have also been investigated in half-cell mode and in a single cell.

Chapter 1

Fundamentals and developments

In this chapter, we first introduce the working principles of PEM fuel cell for a brief understanding. The electrochemistry involving in the fuel cell reactions have also been briefly presented in section 1.1. The main components of a PEM fuel cell, including the membrane, the catalyst layer and the gas diffusion layer were introduced in the section 1.2. Our works mainly focus on the platinum catalysts supported on carbon materials. So we gives a short review of the development in the carbon support materials and their functionalization in section 1.3. In the last section, we present a little the systems for the evaluation of the fuel cell materials, half-cell, a single cell and fuel cell stack.

1.1 PEM fuel cell fundamentals

1.1.1 Principles of PEM fuel cell

A schematic representation of a PEM fuel cell is shown in Figure 1.1. The fuel (hydrogen) and oxidant (air/ oxygen) are delivered to each side of the device. At the anode, hydrogen passes through the gas diffusion layer (GDL) and the molecule is decomposed into two positively charged protons and two negatively charged electrons at catalyst layer (CL). Protons pass through the polymer electrolyte membrane and reach the cathode, whereas the negatively charged electrons travel along an external circuit to the cathode, forming an electrical current. At the cathode, the electrons recombine with the protons, and together with the oxygen molecules in the CL, form the product water[1].The chemical equations are given as follows:

Anode:

$$H_2 \longrightarrow 2H^+ + 2e^- \tag{1.1}$$

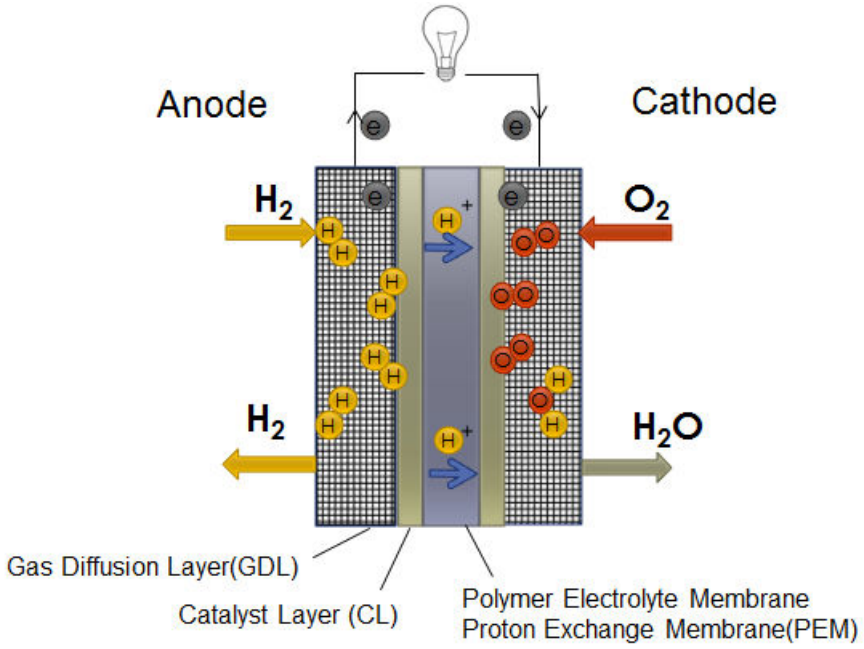

Figure 1.1: A sketch of the principle of a PEMFC

Cathode:

$$O_2 + 4H^+ + 4e^- \longrightarrow 2H_2O \tag{1.2}$$

The total reaction is

$$H_2 + {}^1\!/_2 O_2 \longrightarrow H_2O \tag{1.3}$$

with a theoretical cell voltage to be 1.229 V at 25°C and 1 atm.[3]

Hydrogen Oxidation Reaction (HOR)

In PEM fuel cell technology, H_2 is used as a fuel. The overall reaction of HOR is expressed as Equation 1.1, in which three sequential steps can occur in the presence of platinum[1]:

1) Adsorption step: in the presence of platinum catalyst, a hydrogen molecule is adsorbed on the particle:

$$H_2 + 2Pt \rightarrow Pt - H_2 \tag{1.4}$$

2) Ionization step: there are two possibilities of splitting of adsorbed hydrogen to adsorbed H atom

a) Tafel route

$$Pt - H_2 + Pt \rightarrow 2Pt - H_{ad} \tag{1.5}$$

b) Heyrovsky route

$$Pt - H_2 \rightarrow Pt - H_{ad} + H^+ + e^- \tag{1.6}$$

and followed by Volmer route

$$Pt - H_{ad} \rightarrow Pt + H^+ + e^- \tag{1.7}$$

3) Desorption step: the produced H^+ is desorbed and then transferred into the electrolyte.

In the process, Pt-H_{ad} is the reactive intermediate of hydrogen atom adsorbed on platinum. The overall reaction rate is controlled by the step which is far slower than the others, i.e. the rate determining step (rds).

HOR is also an important process in fuel cell reaction. Moreover, it presents a model system for the fundamental understanding of electrochemical kinetics, electrocatalysis, and electrochemical surface science. Almost all the basic laws of electrode kinetics and the concepts of electrocatalysis were developed and verified by the examination of HOR [1, 2].

Oxygen Reduction Reaction (ORR)

ORR in aqueous solution occurs mainly by

1) direct 4-electron reduction pathway

$$O_2 + 4H^+ + 4e^- \rightarrow 2H_2O \tag{1.8}$$

or 2) 2-electron reduction pathway

$$O_2 + 2H^+ + 2e^- \rightarrow H_2O_2 \tag{1.9}$$

$$H_2O_2 + 2H^+ + 2e^- \rightarrow 2H_2O \tag{1.10}$$

Most researches in MEA have been focused on cathode ORR development because the ORR kinetics is much slower, being the rds of the total reaction. The exchange current density of ORR, even in the presence of platinum based materials, ranges from 10^{-10} to 10^{-8} A·cm^{-2}, while the value of HOR is around 10^{-3}A·cm^{-2}[1, 2].

1.1.2 Electrochemistry in PEM Fuel cell

Enthalpy of Reaction

For the hydrogen/ oxygen cell, the heat or enthalpy of the reaction 1.3 is the difference between the forming enthalpy of products and reactants.

$$\Delta H_f = H_{f,H_2O(l)} - H_{f,H_2} - {}^1\!/_2 H_{f,O_2} \tag{1.11}$$

At 25°C and 1 atm, the value of ΔH_f^0 is -286 kJ·mol^{-1}.

Gibbs Free Energy

The change in Gibbs free energy (ΔG_f) of a reaction is the Gibbs free energy difference between the products and the reactants. So ΔG_f of hydrogen/oxygen fuel cell reaction 1.3 is:

$$\Delta G_f = G_{f,H_2O(l)} - G_{f,H_2} - {}^1\!/_2 G_{f,O_2} \tag{1.12}$$

It is a parameter of temperature and pressure.

For a reversible electrochemical reaction, the Gibbs free energy would be converted to electrical energy. The relation of the voltage of the fuel cell and ΔG_f^0 is given in Nernst equation

$$\Delta G_f = -nFE \tag{1.13}$$

where F is the Faraday constant (96485 C·mol^{-1}) and E is the voltage of the reaction (V); n is the number of electrons in the electrochemical reaction. In the case of a hydrogen fuel cell, for each mole of hydrogen, two moles of electrons pass around the external circuit, n=2.

At 25°C, 1 atm, we obtained a reversible hydrogen/ oxygen fuel cell potential, also called theoretical open circuit voltage (OCV)

$$E^0 = -\frac{\Delta G_f^0}{nF} = -\frac{-237.2}{2 \times 96485} V = 1.229V \tag{1.14}$$

Fuel cell efficiency

The efficiency of an energy conversion device is defined as the ratio between useful energy output and energy input. In fuel cells, the useful energy output is the electrical energy produced, and the energy input is the enthalpy of hydrogen. For a reversible

cell reaction, all the Gibbs free energy can be converted in to electrical energy, the theoretical deficiency at 25°C and 1 atm is

$$\phi_{max} = \frac{\Delta G_f^0}{\Delta H^0} = \frac{-237.2kJ/mol}{-286kJ/mol} = 82.9\%$$

The actual efficiency of the cell is defined as

$$\phi = \frac{V}{\Delta H^0/nF} = \frac{V}{1.48V}$$

where V is the actual cell voltage.

Butler-Volmer Equation

For an elementary reaction,

$$O + ne^- \leftrightarrow R \tag{1.15}$$

The Butler-Volmer equation gives the current-potential relationship:

$$i = i_{re} - i_{ox} = i_0 exp(-\frac{\alpha nF\eta}{RT}) - i_0 exp(\frac{(1-\alpha)nF\eta}{RT}) \tag{1.16}$$

where i is the net current density; i_{re} is the current density in reduction reaction; i_{ox} is the current density in oxidation reaction; i_0 is the exchange current density, which is equal to the current density of reduction or oxydation at equilibrium; α is the electron transfer coefficient, n is the electron transfer number in the rate determining step; and η is the overpotential, which is defined as the potential difference between the electrode potential at a certain current density and the electrode potential at zero current density (reversible potential).

The Butler-Volmer equation is applied to a fuel cell anode and cathode reaction, and the anodic and cathodic kinetic current density, i_a and i_c, are expressed as follows:

$$i_a = i_{0,a} exp(-\frac{\alpha_a n_a F\eta_a}{RT}) - i_{0,a} exp(\frac{(1-\alpha_a)n_a F\eta_a}{RT}) \tag{1.17}$$

$$i_c = i_{0,c} exp(-\frac{\alpha_c n_c F\eta_c}{RT}) - i_{0,c} exp(\frac{(1-\alpha_c)n_c F\eta_c}{RT}) \tag{1.18}$$

where, $i_c = -i_a$; $i_{0,a}$, α_a, n_a, η_a represent the exchange current density, transfer coefficient, electron transfer number in the rds, and overpotential of the anode reaction (HOR), respectively; $i_{0,c}$, α_c, n_c, η_c are the parameter in cathode reaction (ORR).

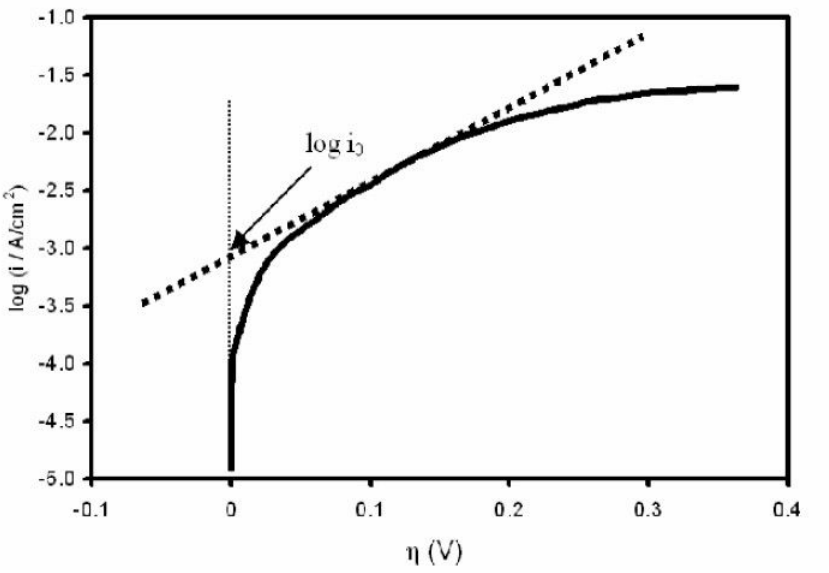

Figure 1.2: A Tafel plot from [1]

Linear Polarization

At lower overpotential ($\eta < 30\text{mV}$), $|\ \frac{nF\eta}{RT}\ | \ll 1$, Equation1.16 is simplified to:

$$i = i_0 \left[(1 + \frac{-\alpha nF\eta}{RT}) - (1 + \frac{(1-\alpha)nF\eta}{RT}) \right] \tag{1.19}$$

that is

$$i = -i_0 \frac{nF\eta}{RT} \tag{1.20}$$

therefore,

$$R_{ct} = -\frac{\eta}{i} = \frac{RT}{nFi_0} \tag{1.21}$$

R_{ct} is the charge transfer resistance, which refers to the barrier across which the electrons passed from the electrode surface to the adsorbed species or from the adsorbed species to the electrode.

Tafel Equation

At high overpotential, one term in the Butller-Volmer equation can be ignored, e.g. the reduction reaction rate is much higher than that of the oxydation reaction, $i_{re} \gg i_{ox}$, so Equation 1.16 is written as

$$i \cong i_{re} = i_0 exp(-\frac{\alpha n F \eta}{RT}) \tag{1.22}$$

$$lni = lni_0 - \frac{\alpha n F \eta}{RT} \tag{1.23}$$

$$\eta = \frac{RT}{\alpha n F} lni_0 - \frac{RT}{\alpha n F} lni \tag{1.24}$$

$$\eta = \frac{2.303RT}{\alpha n F} logi_0 - \frac{2.303RT}{\alpha n F} logi \tag{1.25}$$

as $i_{re} \ll i_{ox}$,

$$i \cong i_{ox} = -i_0 exp(\frac{(1-\alpha) n F \eta}{RT}) \tag{1.26}$$

$$\eta = -\frac{2.303RT}{(1-\alpha) n F} logi_0 + \frac{2.303RT}{(1-\alpha) n F} log(-i) \tag{1.27}$$

Equation 1.24 and1.27 have been expressed as an empirical equation by Tafel:

$$\eta = a + blog \mid i \mid \tag{1.28}$$

This is the Tafel equation. In a certain current density range, the overpotential is linearly dependent on the logarithm of current density, and the slope of the line is Tafel slope b. The exchange current density, i_0, can be obtained from the intercept at $\eta = 0$.

In the reduction reaction, at a given temperature, Tafel slope, $\frac{2.303RT}{\alpha n F}$, is determined by α and n. The higher the Tafel slope, the faster the overpotential increases with the current density. Thus, for an electrochemical reaction to obtain a high current at low overpotential, the reaction should exhibit a low Tafel slope. The charge transfer coefficient, α, is the proportion of the electrical energy applied that is harnessed in changing the rate of an electrochemical reaction. Its value depends on the reaction involved and the materials, in the range of 0-1.0. In anode reaction, its value is about 0.5 for a great variety of electrode materials; at the cathode, it is in the range 0.1-0.5 [3]. For ORR at 25 °C (298K), α_c about 0.50, two Tafel slopes are usually obtained, 60 mV/dec (2-elelctron reduction pathway, n=2) and 120 mV/dec (1-electron reduction pathway, n=1), depending on the electrode materials used and on the potential range [1].

Exchange current density, i_0, is an important kinetic parameter representing the

electrochemical reaction rate at equilibrium. The net current density at equilibrium is zero and the current density of the forward reaction equals that of the backward reaction, which is called exchange current density. The magnitude of the exchange current density determines how rapidly the electrochemical reaction can occur. The exchange current density of an electrochemical reaction depends on the reaction and on the electrode surface on which the electrochemical reaction occurs. For example, on a Pt electrode, the exchange current density of hydrogen oxidation is several orders larger than that of ORR [1].

Besides the electrode materials and the catalyst, the exchange current density is also temperature dependent.

$$i_0 = i_0^{\star} exp(-\frac{E_{act,c}}{RT}) \tag{1.29}$$

where $i_0^{\star}$ is the exchange current density at T= infinite; E_{act} is the activation energy of a reaction.

For electrocatalysts used in PEM fuel cells, such as platinum particles dispersed on carbon materials, the exchange current density is also related to the real electrode area and to the reactant concentration (or partial pressure, for a gas). The nano-Pt particles in the CL have a higher electro-active surface area, which is significantly different from its geometric area, and the partial pressure of O_2 is not 1 atm. Therefore, an apparent exchange current density, $i_c^{apparent}$ is introduced [1]:

$$i_{0,c}^{apparent} = (ECSA)_c i_{0,c} (\frac{P_{o_2}}{P_{o_2}^0})^{\alpha_c} \tag{1.30}$$

where $(ECSA)_c$ is the electrochemical surface area of Pt in the cathode; $P_{O_2}^0$ is the standard O_2 pressure and P_{O_2} is the actual O_2 partial pressure.

Voltage loss

In fuel cell operation at 25^0C, it is found that the real potential is much lower than E^0. The characteristic polarization curve of PEM fuel cell is shown in Figure 1.3. There are four causes of irreversibility, as explained in [3].

Open circuit voltage As it is shown in Figure 1.3, even the open circuit voltage is lower than the theoretical fuel cell potential. It is often reported that the phenomenon is due to the mixed potential and to fuel crossover. In fuel cell cathode, besides ORR on pure platinum catalyst, unavoidable parasitic reactions, which tend to lower the

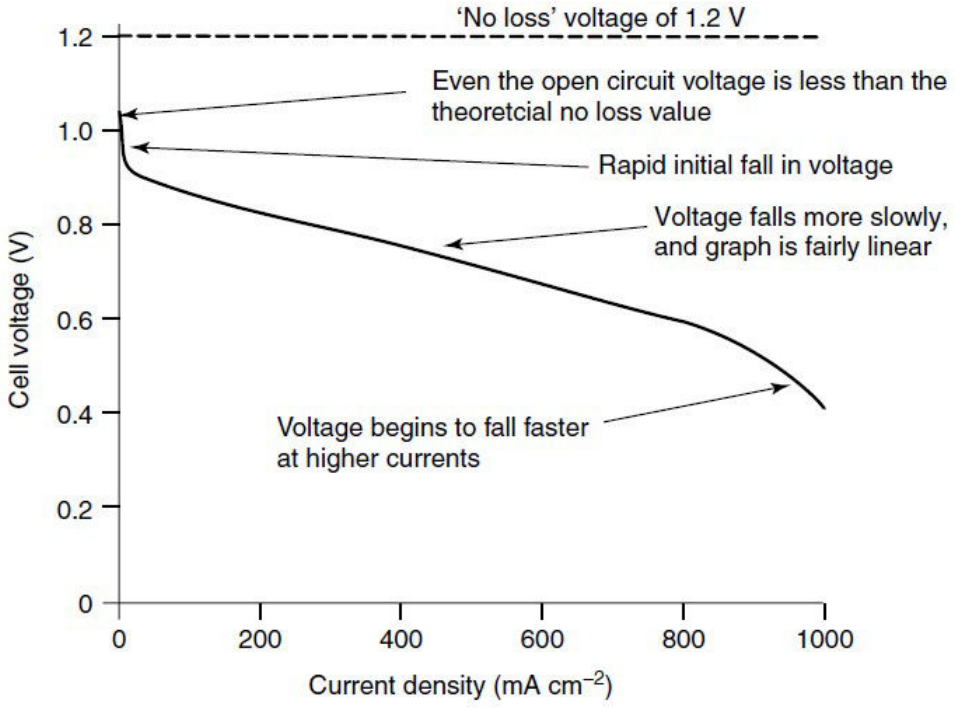

Figure 1.3: Voltage loss in a low temperature PEM fuel cell [3]

electrode potential, occur. The local electrochemical reaction on the Pt surface could create a PtO surface coverage of 30%, with 70% of the surface remaining as pure Pt.

$$Pt + H_2O \rightarrow PtO + 2H^+ + 2e^- \tag{1.31}$$

with $E^0_{Pt/PtO}$= 0.88 V/NHE.

H_2 diffuses through the membrane from the anode to the cathode, and reacts directly with oxygen, i.e. fuel crossover. Otherwise, the reduction of oxygen to H_2O_2, as well as the dissolution of platinum, reduce the OCV [4].

Activation loss At low current densities, the cell potential drops sharply. That is activation loss, activation overpotential, caused by the kinetics of the electrode reactions, especially the sluggish ORR kinetics or low catalyst activity in cathode. In low- and medium-temperature fuel cells, activation loss is the most important irreversibility and cause of voltage drop. The relationship between the activation loss and current density is explained by Tafel's law, Equation 1.24,

$$\Delta E_{act} = \mid \eta_c \mid = \frac{2.303RT}{\alpha_c n_c F} log(\frac{i}{i_{0,c}}) \tag{1.32}$$

The exchange current density of cathodic reaction, ORR, $i_{0,c}$ is the crucial factor in reducing the activation overpotential and in improving fuel cell performance [3]:

i) raising the operation temperature, whose relationship with i_0 has been given in Equation 1.29. In high-temperature fuel cells, for example, $i_{0,c}$ in a 800°C cell is about 10 mA·cm^{-2}, a 100-fold higher than that in a low-temperature cell, about 0.1 mA·cm^{-2};

ii) using more effective catalysts;

iii) improving the roughness of the catalyst layer. In Equation 1.30, it is shown that higher surface area could result in higher apparent exchange current density;

iv) increasing reactant concentration and the oxygen pressure, for example, using pure O_2 instead of air.

Ohmic Loss At intermediate current densities, voltage is nearly in linear to the current. Ohmic loss, also called ohmic overpotential, is due to the ohmic resistance, containing the ionic resistance of the polymer membrane and the electronic resistance of the electrodes and the collector plate. This voltage drop is essentially proportional to current density, linear, given by Ohm's law,

$$\Delta E_\Omega = i \cdot R_\Omega \tag{1.33}$$

where i is the current density flowing through the cell, and R_Ω is the ohmic resistance of the fuel cell, including the ionic, electronic and contact resistances. In most case, electronic resistance can be negligible, while ionic resistance of the membrane is the largest source of ohmic losses. Minimizing the ohmic losses requires effective water management in the membrane, excellent electron conductive materials, and minimal contact resistance [1].

Mass transfer Loss In high current density region, voltage decreases rapidly as the current increases, indicating a voltage loss caused by the concentration gradients of the reactants near the electrode surface, corresponding to local depletion of reactants. As oxygen is supplied to the cathode in the form of air, it is then reduced at CL during the fuel cell operation and there will be a slight reduction in its concentration. The extent of this concentration change will depend on the current and on physical factors relating to how fast oxygen can be replenished. In the result of the failure to transfer sufficient reactant to the electrode surface, this type of loss is called mass transfer loss, as shown in Figure 1.3. To minimize the concentration overpotential requires

good electrode structure as well as effective water management in the catalyst layer and the gas diffusion layer [3].

1.2 Fuel cells materials

1.2.1 Membrane

Many researches on membrane development or technology have been carried out to proceed the commercialization of fuel cell. A membrane used in PEM fuel cells works as the solid polymeric electrolyte between two electrodes. It is a separator of electron or gas on each side, and also an electrolyte for transport of hydrogen ions (protons) during the reaction. An ideal polymer for PEM fuel cell must have excellent proton conductivity, chemical and thermal stability, strength, flexibility, low gas permeability, low water drag, low cost, and good availability [5].

Ionic groups are introduced into the polymer membranes to allow the conductivity in two ways: i) ionic groups are chemically bonded to the side chains of the polymer backbone; ii) ionic materials are physically blended with the membrane matrix. Chemically grafted membranes, homogeneous ion exchange membranes, exhibit good electrochemical properties but low mechanical strength. Comparatively, heterogeneous ion exchange membranes have a good mechanical strength but low electrochemical performance.[6, 7, 8].

Depending on the type of ionic groups transferring, polymer electrolyte membranes are classified into anion exchange membranes and cation-exchange membranes. The cation exchange membranes, containing negatively charged groups on the polymer chain, such as SO_3^-, COO^-, PO_3^-, PO_3H^-, $C_6H_4O^-$, allow the transport of cations. The anion exchange membranes contain positively charged groups, such as NH_3^+, NRH_2^+, NR_2H^+, NR_3^+, PR_3^+, SR_2^+, only allow the passage of anions but reject cations. In moist state, water is absorbed on the polymer, and the gel-like polymeric structures are swollen and carrying fixed positive and negative charges [9, 10].

Nafion is one of the most widely used membranes for PEM fuel cells, created by DuPont company. It was a chemically stable cation-exchange membrane based on sulfonated polytetrafluoroethylene developed in the 1970's. The molecule structure is shown in Figure 1.4, an aliphatic perfluorinated backbone with ether-linked side chains ending in sulfonate cation exchange sites. It is a co-polymer of tetrafluoroethylene and sulfonyl fluoride vinyl ether, with a semi-crystalline structure. The backbone structure, which resembles PTFE, Teflon^{TM}, gives Nafion long-term stability in ox-

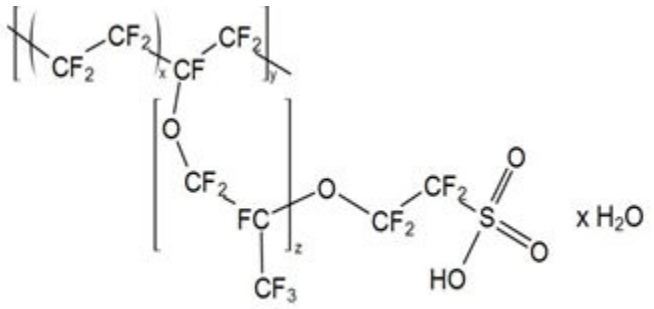

Figure 1.4: Molecular structure of Nafion® membrane

idative or reductive conditions, while the sulfonated side chains could transfer proton in moist state. The ionic groups could absorb large amounts of water, and then the polymer swells and forms proton-conducting channels [1, 11]. The two factors affecting the conductivity of the proton exchange membrane are the hydration level and thickness of the membrane [9, 12].

Due to the high price, insufficient conductivity at low humidification and the difficulty involved in the disposal of Nafion® membrane, investigations for low-cost non-perfluorinated ionomer membranes, which are environmentally disposable have been carried out. Proton conducting membranes investigated to date include polysulfonated triflurostyrene, polyether ether ketone (PEEK), poly(arylene ether sulfone) , PVDF-graft styrene, acid doped polybenzimidazole (PBI), which are cheap and chemically stable but insufficient proton conductivity [13, 14].

To develop the polymer membranes for fuel cells working at temperatures above 100°C, inorganic nanoparticles have been dispersed in the polymeric matrix to improve the proton conductivity. Layered zirconium phosphate (Zr $(O_3POH)_2$, hereafter ZrP) and phosphonates were used as fillers of proton conducting polymeric membranes due to their good chemical and thermal stability [15]. A Nafion/sulfonated poly(phenylmethyl silsesquioxane) (PPSQ) composite membrane is fabricated for direct dimethyl ether fuel cell applications operated above 100°C by Nam et al. [16] Nafion/ TiO_2 [17, 18, 19], Nafion/ SiO_2 [20, 21] membrane were investigated in high temperature PEM fuel cells. Composite membranes, containing, sulfonated poly (arylene ether sulfone) (PAES) copolymers and the incorporation of functionalized MWCNTs, were prepared for high temperature (120 °C) PEM fuel cells by Yu et al. [22].

1.2.2 Catalyst layer (CL)

Catalyst layer, is a thin layer (about 10 μm) applied on a support (GDL), where fuel cell reactions take place. Components contained in a CL are key to the electrochemical reaction: catalyst, carbon support, ionomer and void space [23, 24, 25]. The catalysts will be discussed in Section 1.3.

Generally, for fabricating thin-film CLs fabrication, there are three main procedures [26, 27]: decal transfer method (DT), catalyst coated gas diffusion layer (CCG) and catalyst-coated membrane (CCM). In DT, CLs that are primarily formed over the decal substrates, and subsequently transferred to the membrane by hot-pressing [28]. In CCG, the catalyst ink is coated on the GDL and then hot-pressed onto the membrane to prepare the MEA, which is suitable for large-scale and mass productions. However, a large amount of catalyst may diffuse into the GDL structure, resulting in loss activity. In the CCM method, the CLs are directly applied to both sides of the pre-treated Nafion membrane.

Hot-pressing is an important process in the preparation of MEA. There are three main parameters: temperature, pressure, and duration. Typically, the hot-pressing temperature is selected between the glass transition temperature (T_g, 115°C) of the Nafion and the decomposition temperature (T_d > 280°C). However, dehydration of Nafion membranes is an additional serious problem in the operation of fuel cells at elevated temperatures (>100°C). Additionally, there may be loss of porosity and activity in the CLs. Jung et al. [29] studied T_g of Nafion 117 membranes by step-by-step-DSC during hot-pressing. It is found that, during the pretreatment of the membrane, the value of T_g decreased drastically because of the plasticizer effect of water. In the hot-pressing process, the value gradually increased due to loss of water. When the Nafion 117 membrane was completely dried, it finally reached 132°C. A crystalline morphology was developed in the membrane, which could lead to low water uptake and proton conductivity. Therefore, the thermal heat treatment of the MEA should be carefully controlled in a region slightly above the glass transition temperature, i.e. in the range from 120 to 140°C. On the other side, pressure is also an critical factor in hot-pressing process. A small pressure will not provide enough binding force between the electrodes and the membrane. However, too high pressure could damage the components of MEAs, which in turn, leads to a porosity loss and larger oxygen transfer resistance in CL. It is reported that carbon cloth can be mechanically damaged by pressures exceeding 100 kg cm^{-2}.

Many works have been carried out on the MEA preparation and it is found that the optimum conditions would vary according to the method of the MEA preparation.

Maryam et al. [26] fabricated MEAs with Pt/MWCNTs nanocatalysts by catalyst-coated membrane (CCM) method. The effects of hot-pressing conditions, including temperature (100 and 130°C), pressure (800 and 1000 psi) and time (3 and 5 min) on the performance of MEAs were investigated. It has been found that the CCM-based MEAs hot-pressed at 800 psi and 100 °C for 3 min showed the highest power density, and that pressure was the most effective factor, followed by temperature and time, respectively. Bayrakceken et al. [30] studied the hot-pressing conditions influence on two types of MEA: homemade five-layer (CCG-MEAs) and commercial three-layer (CCM-MEAs). It was observed that hot-pressing of GDL onto the three-layer MEA decreases the fuel cell performance and the best performance was obtained by the CCM-MEAs without hot-pressing. But in the case of five-layer MEA, there was an optimum value for the hot-pressing conditions, 172 $N \cdot cm^{-2}$ (249.4 psi). Mainly, hot-pressing is known as an essential step for the preparation of the MEAs fabricated via CCG-based method. However, in CCM method, it can be eliminated. It has been reported that hot pressing does not significantly influence the cell resistance or methanol crossover, but it can decrease the cell performance by hindering mass transfer in the anode CL. On the other hand, the membranes that had not been subjected to hot pressing could easily be reused, making recycling of membranes and catalysts more feasible [31].

In the fabrication of CL, catalyst ink, containing electrocatalyst, polymeric binder and solvents, is deposited on top of the substrate, being GDL or membrane. Binder, in CL, also plays an important role in determining the electrode performance. First, binder was used to attach the catalyst on support, to maintain the integrity of the electrode structure. It concerns the mechanical properties of CL and the gas permeability in the electrode. Otherwise, as to the the properties of the polymer binder, the electrochemical activity of CL has also been influenced [32].

According to the types of fuel cell, different binders have been selected. For example, in anion exchange membrane fuel cells, anion-conducting ionomers are used to conduct anions [33]. The synthesis and application of an electrode binder in fuel-electrolyte-fed fuel cells, agar chemical hydrogel, has been reported by An et al. [34]. Su et al. [35] investigated the effect of various polymer binders in phosphoric acid doped polybenzimidazole (PBI)-based high temperature proton exchange membrane fuel cells. The results showed that polytetrafluoroethylene (PTFE) and polyvinylidene difluoride (PVDF) are more attractive as CL binders than conventional PBI or Nafion binder. In Wang et al. 's work [36], adjustable Nafion/ PTFE mixed binders have been investigated in air-cathode microbial fuel cells. Jung et al. [29] synthesized

a sulfonated poly(arylene ether sulfone) binder for direct methanol fuel cell, which is found to be more efficient in achieving long-term stability of the cell performance than the conventional Nafion binder.

Poly tetrafluoroethylene (PTFE), a typical neutral binder, was added into CL to serve as an electrode binder [37]. However, since PTFE is impermeable to reactants, the reactants cannot penetrate the PTFE binder on catalyst particles, thereby reducing the catalyst utilization in the electrochemical reaction [34]. Oh et al. [38] studied a hydrophobic blend binder for anti-water flooding of cathode catalyst layers in polymer electrolyte membrane fuel cells. They added a copolymer binder, poly(vinylidene fluoride-co-hexafluoropropylene) copolymer to the existing sulfonated poly(ether ether ketone) (sPEEK) binder. The introduction of the copolymer binder lowered the glass transition temperature of the binder, which contributes to enhancing the adhesion properties between the CLs and membranes.

Nafion, due to its high proton conductivity and good chemical and mechanical stability, has been the commonly used binder. It could increase the catalytic activity and also helps to retain moisture and to prevent membrane dehydration, especially at high current densities [39, 40, 41]. On the other side, excessive loading of Nafion would cause the retardation of oxygen transport. Many works have been undertaken for optimisation of Nafion binder in the catalyst layer. However, each reported result showed slightly different optimum loading in various Nafion incorporating way. Nafion content in a catalyst layer, in spite of its requried presence, affects the electrocatalytic activity and the ionic resistance.

Antolini et al. [42] investigated the effect of Nafion loading in polymer electrolyte fuel cells (PEFCs) and recommended the optimal Nafion loading at $56 \cdot \frac{L_{Pt}}{P_{Pt}}$, where L_{Pt} is the platinum loading ($mg \cdot cm^{-2}$), and P_{Pt} is the weight percentage of metal supported in carbon. A minimum in the polarization resistance and in the oxygen reduction overpotential and a maximum in the electrochemical active area have been found with this Nafion loading. In the work of Passalacqua et al. [43], the influence of Nafion loading on the cell performance, and the effects on pore size distribution and Pt surface area were investigated. It is also indicated that the existence of an optimum Nafion content of 33wt.% for a PEFC catalyst layer. Lai et al. [44] studied the effect of Nafion loading sprayed on the surface of CL in PEMFC. The maximal catalyst activity, and the minimum interfacial resistance were obtained with the electrode prepared with a Nafion loading of 1.0 $mg \cdot cm^{-2}$. Moreover, they found that Nafion loading exceeding 1.0 $mg \cdot cm^{-2}$ is not advantageous in increasing the two-phase interface. Certain channels for the transportation of the reactants were

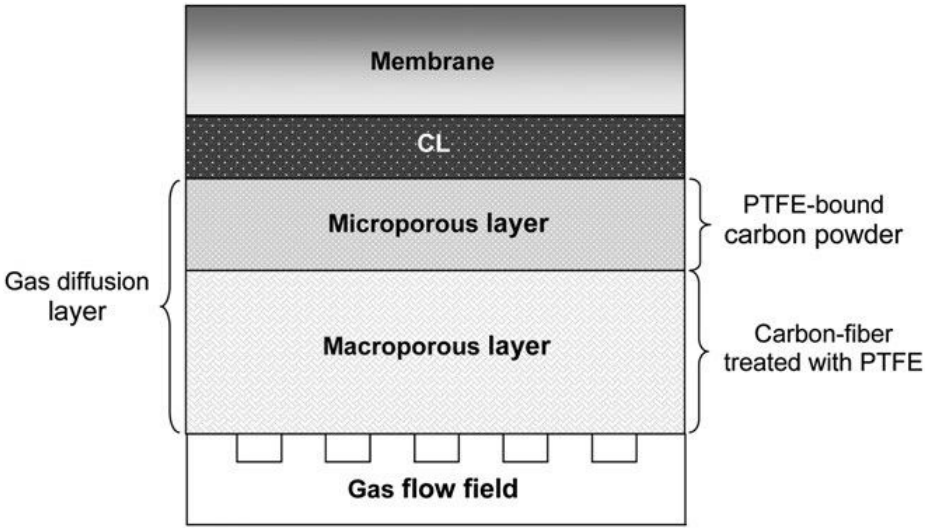

Figure 1.5: Schematic diagram of a dual-layer GDL for PEM fuel cells [49]

actually blocked by the excess Nafion on the surface. Lee et al. [45] prepared the electrodes with various Nafion ionomers inside and/or on the surface in the catalyst layer. They found that, compared to the cells with catalyst layer incorporated inside of the catalyst layer, the cells with catalyst layer coated on the surface showed better performance irrespective of Nafion content. The best cell performance was obtained for electrode with 0.5 mg·cm^{-2} Nafion inside and 1.0 mg·cm^{-2} on the surface.

1.2.3 Gas diffusion layer (GDL)

Gas diffusion layer, also called diffusion media, is another important component in fuel cells, which serves as the backing material for MEA and also the passage for gas supply and water removal. It works as the electrical connections between the carbon-supported catalyst and the bipolar plate or other current collectors. The porous nature facilitates the effective diffusion of each reactant gas to the catalyst layer. In addition, GDL, typically wet-proofed, helps in managing water in the fuel cell. Water is carried to the membrane and carried away from the electrolyte surface by gas, but not accumulated in GDL. An ideal GDL is required to effectively transport the gas reactants to the catalyst layers, with proper hydrophobicity and low electronic resistance [46, 47, 48].

The GDL is usually made of a single layer of porous substrate or a dual layer with a thin micro-porous layer and a macro-porous layer. Single layer carbon-based GDL is a macro-porous production, including woven carbon cloth, non-woven carbon paper, carbon felt and carbon foam, with a thickness from 0.2 to 0.5 mm. It pro-

cesses high chemical and electrochemical stability, high gas permeability and good electronic conductivity. Metal-based GDLs, such as metal mesh, metal foam, and micro-machined metal substrate, have been developed and applied in PEM fuel cells due to their good mechanical strength and high stability over a wide potential range. In a dual-layer GDL, as shown in Figure 1.5, the layer in contact with the flow field is a macro-porous carbon substrate, serving as a current collector, a physical support for the catalyst layer. It also serves as an elastic component of MEA, which is necessary for handling the compression needed to establish an intimate contact. The thinner micro-porous layer in the dual-layer GDL, in contact with the catalyst layer, consists of carbon black powder and some hydrophobic agent, which provides proper surface pore size and hydrophobicity to avoid flooding and to enhance intimate electronic contact at its interface with the catalyst layer [49, 50].

1.3 Fonctionalized Pt/carbon catalyst

The catalyst plays a critical role of reducing the reaction activation barrier. Platinum (Pt) and Pt based alloys are the most commonly used catalysts in fuel cells for high catalytic activity, high chemical stability, high exchange current density (i_0), and superior work function. However, the global scarcity of Pt contributed to the high price of fuel cells [51].

Pt/ Carbon catalyst, platinum particles highly dispersed onto carbon materials with high surface area, are generally used in low temperature fuel cells. Based on that, a number of studies have been taken on the reduction in the electrocatalyst loading and meanwhile improvement of the catalytic activities, by decreasing the electrocatalyst nanoparticles size [52, 53], developing metallic alloys (either as binary and ternary), such as Pt/ Ru [54, 55], Pt/ Cu [56], Pt/ Pd [57], Pt/ Co [58, 59, 60, 61] and Pt-free electrocatalysts [62, 63], and supporting Pt on conductive and porous materials [64].

The properties of the carbon supports have been found to possess strong influence on the performance of the metal supported catalysts, related to their morphology, size distribution and stability [65, 66]. Lo et al. [67] studied the effect of pore size of carbon support on the electrocatalytic performance of DMFC. It was found that the methanol oxidation reaction activity tended to increase with increasing pore size of the carbon supports, while Pt catalyst supported on micro-porous carbon materials had superior stability in terms of tolerance for CO poisoning than those with greater pore size or having meso- and macro-porosity. The carbon structure plays an important

role in the access of the reactants to the catalytic sites and the removal of reaction products. The stability of the carbon support in the fuel cell environment could also affect the durability of catalysts [68, 69, 70].

For fuel cell applications, ideal carbon supports should have several characteristics: i) high electrical conductivity to facilitate the transport of electron during the electrochemical reactions; ii) high specific surface area for dispersing metal particles; iii) available meso-porous structure for efficient diffusion of reactant and by-products; iv) high electrochemical stability [65, 66, 71].

1.3.1 Carbon materials

Carbon blacks (CBs)

Carbon blacks (CBs) are the most commonly used supports for Pt and Pt-alloy catalysts in many studies and commercial applications, due to its stability in both acid and basic media, good electronic conductivity, high surface area, low cost and easy availability. Commercial CBs of turbostratic structures with high surface areas are used to ensure large electrochemical reaction surfaces, such as Vulcan XC-72R (Cabot Corp, 250 $m^2 \cdot g^{-1}$), Shawinigan (Chevron, 80 $m^2 \cdot g^{-1}$), Black Pearl 2000 (BP2000, Cabot Corp., 1500 $m^2 \cdot g^{-1}$), Ketjen Black (KB EC600JD & KB EC600J, Ketjen International, 1270 $m^2 \cdot g^{-1}$and 800 $m^2 \cdot g^{-1}$, respectively) and Denka Black (DB, Denka, 65 $m^2 \cdot g^{-1}$) [71].

In spite of the wide application as catalyst support, CB materials suffer the problems, as follows: i) high content of micro-pores and recesses, where catalyst nanoparticles are trapped and become inaccessible to reactants, resulting in the loss of catalytic activity; ii) significant mass transfer limitations due to its dense structure, leading to a low Pt utilization; iii) the presence of organo sulphur impurities; iv) carbon black undergoes electrochemical oxidation during the fuel cell operation. Vulcan XC-72 (R) is the most commonly used carbon support for PEM fuel cells, because of its high electrical conductivity and high specific surface area. However, it contains a large amount of micropores below 1 nm. With Nafion ionomer binder, because of the micelles (>40 nm) larger than the recesses in the CB material structure, the metal nanoparticles in the pores are not accessible to Nafion ionomer and therefore have no contribution to the electrochemical activity. In other words, the interaction between Nafion ionomer and the catalyst nanoparticles depends on the pore size and pore distribution of CBs [71, 72, 73, 74].

As an effort to overcome these problems, various carbon materials have been tested

to improve both catalytic activity and stability, such as carbon manotubes (CNTs), carbon nanofibers (CNFs), mesoporous carbon and graphene. Nanostructured materials, of unusual catalytic, mechanical, electrical, and optical properties, have been proposed as a promising solution[72, 75, 76, 77].

Nanotubes (CNTs)

Nanotubes, of hollow structure with the walls, are formed by rolling one-atom-thick carbon sheets, called graphene, at specific and discrete ("chiral") angles, and the properties are depended on the rolling angle and radius. Nanotubes are categorized as single-walled nanotubes (SWCNTs) and multi-walled nanotubes (MWCNTs), as shown in Figure 1.6 [78]. A perfect graphene sheet, i.e., a polyaromatic mono-atomic layer consisting of a hexagonal arrangement of sp^2 hybridized carbon atoms, is rolled into a cylinder along a lattice vector (m,n). SWCNTs have a relatively small diameter, close to 1 nanometer, whereas the length can range from a few microns to several millimeters. The conductivity of SWCNT, metallic or semi-conducting, is characterized by the chiral vector (m, n). MWCNT contains multiple rolled sheets in a concentric set of cylinders with a constant interlayer spacing of 0.34 nm. The diameters range from several nanometers to tens of nanometers. It have been reported that MWCNTs are more conductive while SWCNTs have larger surface areas [71, 72].

CNTs have received wide attention in the application as catalyst support in fuel cells, because of their high aspect ratio, good electronic conductivity, high surface area. And it has been shown that CNTs supported Pt catalyst exhibit a better performance and a better durability than that on a carbon black support [79, 80, 81, 82]. However, due to the inertness of CNTs, effective attachment of metal catalysts remains a problem in the application as electrocatalyst supports [82]. Therefore, the surface functionalization of CNTs has been developed to increase the interaction between the catalyst and CNTs and to enable a homogeneous metal deposition. Functional groups, introduced by oxidation treatments, could anchor the catalyst precursor or even the active phase to the support. It has shown that functionalized carbon nanofibers present better performances in a PEM fuel cell [72]. Dameron et al. [79] modified the surfaces of vertically aligned carbon nanotube arrays by plasma and molecular precursor treatments, leading to improved catalyst deposition. It was also found that surface functionalization affects their performance towards oxygen reduction reaction.

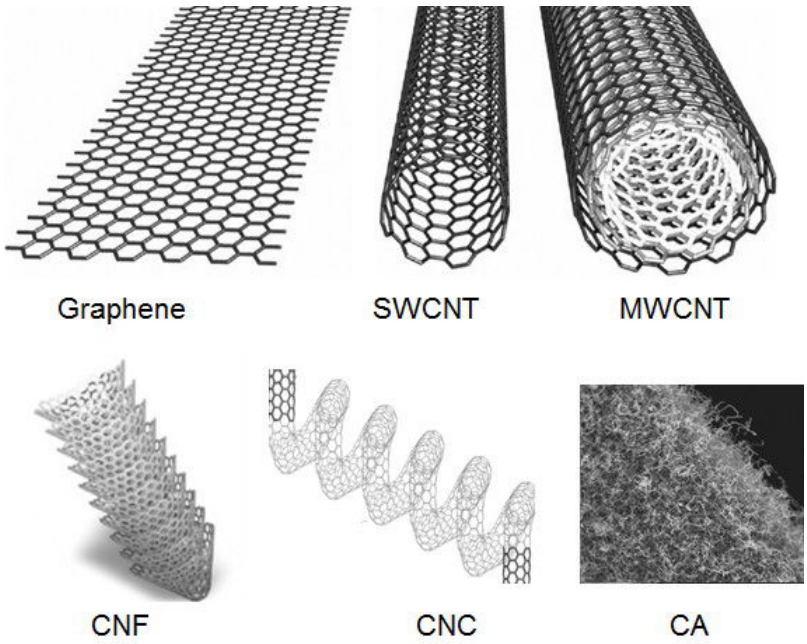

Figure 1.6: Nanocarbon materials [78, 83, 89, 97]

Carbon nanofibers (CNFs)

Carbon nanofibers (CNFs) are sp^2 based linear filaments (diameter ca. 100 nm) with graphene layers arranged as stacked cones, cups or plates, as shown in Figure 1.6 [83]. The graphite-like structure provides a high electrical conductivity and a high oxidation resistance. CNFs, in textural properties, contain low content of micro-pores and impurities. In comparison with Vulcan XC-72R, of a specific surface area about 250 $m^2 \cdot g^{-1}$, the value for CNFs ranges from 90 $m^2 \cdot g^{-1}$ up to 210 $m^2 \cdot g^{-1}$. However, the content of micro-pores in CNFs is less than 1%, while the value of Vulcan XC-72R is around 10%. A high meso-porosity in CNF enhances, in principle, mass transfer through the electrocatalyst layers which in turns enhances the electrochemical performance. Moreover, the ratio of edge atoms to basal atoms of CNFs is controllable, which provides a mean to adjust the deposition and the interaction with the metal. In addition, carbon nanofibers are inexpensive in comparison to carbon nanotubes and can be produced with various controlled structures at relatively high speeds [84, 85, 86].

CNFs are obtained by the decomposition of carbon-containing gases, like methane or carbon monoxide, over small metallic particles as catalysts, typically metals of the iron subgroup. The surface is modified by an oxidation treatment subsequently, in order to introduce oxygen surface groups, for the same reason in the CNTs func-

tionalization. These functional groups, affecting surface properties of the CNFs, can significantly decide the manufacture and performance of electrocatalysts. Therefore, the studies in the application of CNFs as electrocatalyst support are aimed at optimizing their surface chemistry in order to improve the metal-support interaction [87].

Guha et al. [88] studied the effect of various functionalized carbon supports: CNF and amorphous activated carbons with a wide range of surface areas, compared with Vulcan XC-72 carbon. It was found that high surface area supports were not necessary to a higher electrochemical utilization of platinum. Lower ohmic losses were observed for low surface area carbon MEAs, which was explained by the microstructures and intrinsic resistivity of supports. In fuel cell test, the characteristics of the lower surface area supports such as CNF and Vulcan XC-72 carbon do not influence the performance. The influence of the support is more critical when high surface area carbons are used because of the vastly different electrode morphology and resistivity.

Carbon nanocoils (CNCs)

Carbon nanocoils (CNCs) are coiled carbon nanotubes of ca. 10 nm in tube diameter, and 10–20 nm in internal coil diameter [89]. The helical graphitic structure shows a moderate surface area (40-240 $m^2 \cdot g^{-1}$) and a relatively high electrical conductivity (0.1-0.2 $S \cdot cm^{-1}$). Based on that, CNCs have also received great attention as catalytic support in fuel cell electrodes [90, 91, 92, 93, 94, 95].

Sevilla et al. [91] synthesized highly graphitic carbon nanocoils as the support for Pt nanoparticles. A highly dispersed Pt/CNCs catalyst, with Pt diameters in the range of 3.0-3.3 nm, was prepared. A high electro-active Pt surface areas (up to 85 $m^2 \cdot g^{-1}$ Pt) and large catalytic activities towards methanol electro-oxidation (up to 201 $A \cdot g^{-1}$Pt) were achieved. Moreover, a considerably higher resistance against oxidation than that of the Pt/Vulcan system was observed. Park et al. [92] studied the PtRu alloy catalysts supported on newly synthesized carbon nanocoil supports, with variable surface areas and crystallinity. It was found that the PtRu/ CNC catalyst exhibited better electrocatalytic performance compared to the catalyst supported on Vulcan XC-72 carbon in the methanol electro-oxidation. Lazaro et al. [96] studied the Pt electrocatalysts supported on carbon nanocoils (CNCs) for ethanol electro-oxidation. It was found that CO oxidation occurred at more negative potentials on Pt/CNC catalysts than on Pt/Vulcan and Pt/C E-TEK ones. On the other hand, higher current densities for the ethanol electro-oxidation were obtained when CNCs were used as supports .

Carbon aerogels (CAs)

Carbon aerogels (CAs) are nanostructured carbon materials possessing a tunable 3-D hierarchical morphology with ultra-fine cell size and an electrically conductive framework [97]. They are obtained from the carbonization of organic aerogels by sol–gel polycondensation of certain organic monomers which show a great versatility both at the nanoscopic level in terms of the pore texture and at the macroscopic level in terms of form. Thus, the surface area, pore volume, and pore size distribution could be customized in the synthesis and processing conditions. In addition, carbon aerogels can be obtained in the form of monoliths, beads, powders or thin films. All these properties make them promising materials for application in adsorption and catalysis. Similar to CB, CAs are made of small primary carbon particles. The major difference between them is the arrangement of these carbon particles, i.e. their porous structure. While carbon particles in CB aggregates through Van der Waals bonds, carbon aerogel powders are covalently bonded and display monolithic structures at the micrometer scale. Metal-doped monolithic organic aerogels can be prepared by addition of the metal precursor to the initial mixture, by ion-exchange or by deposition of the metal precursor on the organic or the carbon aerogel by one of various methods [98, 99, 100, 101, 102].

Marie et al. [102] studied a highly porous CAs supported Pt catalyst in PEM fuel cells. Higher mass transfer voltage loss was found in cathode with carbon aerogel of higher pore-size. As the consequence of Nafion penetration into the larger pore-size, the prepared catalyst layer showed lower porosity. Job et al. [101] prepared carbon xerogels with various pore textures as supports for Pt catalysts to replace the carbon aerogels. And their results showed that the metal surface actually available for ORR and the voltage losses due to diffusion phenomena strongly depend on the carbon pore texture. Finally, some carbon xerogels yield similar performance than carbon aerogels.

Mesoporous carbon materials

Carbon porous materials, divided into several groups by the pore size, can be micro-porous carbon ($<$ 2 nm), mesoporous carbon (2- 50 nm) or macro-porous carbon ($>$ 50 nm). Iinvestigations on the catalyst support were mostly focused on carbon mesoporous materials with large surface area and 3-D mono-dispersed mesospheres, which facilitates the diffusion of the reactants and by-products [71, 67]. By the final structure and method for preparation, carbon mesoporous materials are divided into

ordered mesoporous carbons (OMC) and disordered mesoporous carbon (DOMC). OMC, consisting of periodic arrays of carbon nanorods with uniform mesopores, are prepared with ordered mesoporous silica templates or templating triblock copolymer structures [103].

Due to the advantages, such as high specific surface areas, uniform pore diameters, high thermal, chemical and mechanical stability, a wide range of applications have been explored for OMC including Li-ion batteries and fuel cells. The studies of Joo et al. presented that the OMC supported Pt catalysts exhibited much higher performance than commercial catalysts in DMFC single cell test, which can be attributed to the high surface area and uniform mesopores networks of OMC [104]. For more effective deposition of metal particles, the surfaces of OMC are modified by oxidation treatments in gas or liquid phase in order to create functional groups. In the investigation of Calvillo et al. [65], higher performance was obtained by using OMC modified in diluted HNO_3 acid for 0.5h as catalyst support.

1.3.2 Functionalization method

In the preparation of carbon supported platinum catalysts, two methods are generally applied: impregnation of carbon support with Pt precursor solution, and adsorption of platinum oxide or platinum metal colloids onto the carbon surface [52, 105, 106, 107]. The dispersion of platinum particles is not only affected by the preparation condition, but also related to the surface chemistry of the support. It has been reported that the surface properties of carbon support have an important effect on the aggregation grade of the platinum particles. The less stable surface oxygen groups on the support decompose during the reduction stage of the metal precursor, which facilitates the mobility and the agglomeration of platinum particles on the support surface. As above discussed, due to the graphitic character of nanocarbon materials, an activation of their surfaces may be necessary in order to achieve the satisfactory catalyst dispersion. Chemical modification is a common and essential method for the deposition of catalysts. On the other side, the most stable oxygenated groups of the support can act as anchorage for the metal particles avoiding their agglomeration [65].

Surface chemical modification, by the use of aggressive acid oxidants (HNO_3 and/ or H_2SO_4), brings in the functional groups such as hydroxyl (-OH), carboxyl (-COOH), and carbonyl (-C=0) groups on the surface [108]. The surface graft of the support had also an effect on the hydrophobic/hydrophilic character of the ma-

terials and the electrochemical activity of catalysts. The electronic interaction between the surface groups of the support and the Pt atoms could favor the electron transportation from catalytic sites to the conductive carbon electrode. However, the functionalization of the support also decreases its electrical conductivity, and hence, the conductivity of the electrode [109]. Meanwhile, functionalization could accelerate the electrochemical corrosion of the support reducing the durability of the catalyst. Therefore, more moderate method have been applied, such as sonochemical treatment, electrochemical modification etc., which would be selected according to the carbon materials [65, 72].

Besides covalent coupling of acid groups on the surface of support materials, polymers were introduced onto the external surface by non-covalent interaction, which is based on Van der Waals forces or stacking interactions. The grafting of polymers has been carried out by two methods: "Graft-onto" and "Graft-from". "Graft-onto" involves the attachment of prepared polymer onto carbon black and "Graft-from" is to attach initiators onto the carbon materials, so that polymer grows directly from the carbon surface, via several polymerization intermediates [68].

Sulfonation of carbon structures, providing an ionic conductivity of the electrode in addition to electronic conductivity have been thought as a promising way [110, 111, 112]. Recently, sulfonated carbon supported catalysts have been prepared in serious modification method and the electrochemical performances in fuel cell have been investigated [113]. Wang et al. [114] prepared sulfonated carbon nanotubes with a high density of sulfonyl acid groups by reacting sulfuric acid with MWCNT for 18h at 250°C under a flow of N_2. It has been observed that the Pt/ sulfonated-MWCNTs catalyst showed have high electrocatalytic activity and excellent electrocatalytic performance for the direct methanol fuel cell. Du et al. [115] prepared a sulfonated carbon-nanotube supported platinum catalyst (Pt/ CNT), by thermal decomposition of ammonium sulfate and in situ radical polymerization of 4-styrenesulfonate, for polymer electrolyte fuel cells. Easier access with protons and better catalyst distribution of the sulfonated Pt/ CNT catalysts were achieved in the electrodes. A sulfonated MWCNTs (grafted with benzenesulfonic groups) supported Pt catalyst, synthetized by in situ radical polymerization of 4-styrenesulfonate and isoamyl nitrite, was studied by Sun et al [116]. The results showed that S-MWCNTs/ Pt exhibited higher electrocatalytic activity, enhanced CO tolerance and better stable life. Compared with traditional sulfonation of MWCNTs, small and uniform dispersion of Pt particles loaded onto the surfaces of sulfonated were achieved in situ radical modification processes. OMCs grafted with benzenesulfonic acid by in situ radical

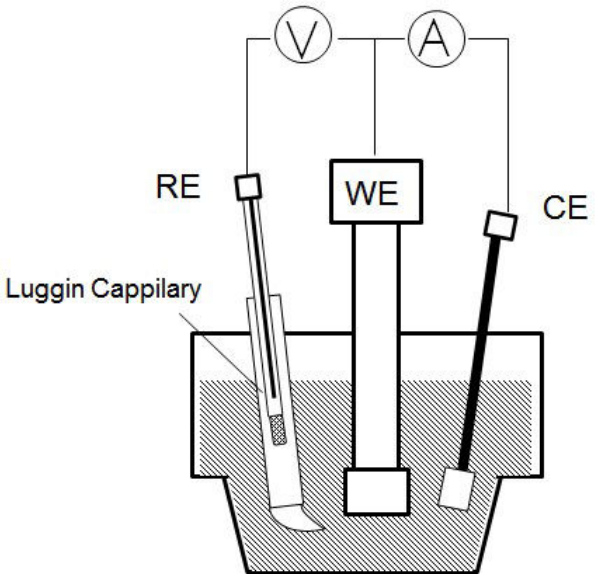

Figure 1.7: Three-electrode system in liquid electrolyte

polymerization of 4-styrenesulfonated and isoamyl nitrite was prepared under ambient conditions by Sun et al. [117]. Kim et al. [118] functionalized the carbon support with sulfonated polymer for direct methanol fuel cells. The MEA with Pt catalyst on functionalized support showed a higher DMFC performance of 30 mW/cm^2 at 50°C without using additional sulfonated polymer, which could be attributed to a better mass transfer which maximize the catalytic activities.

1.4 Electrochemical devices in fuel cell

1.4.1 Half-cell method

For fuel cell applications, half-cell mode is typically used to screen new catalysts or to study reaction mechanisms and kinetics rapidly. This mode is commonly applied in three-electrode system, containing working electrode (WE), counter electrode (CE) and reference electrode (RE) [119, 120, 121]. The working electrode is the electrode of interest, carrying the investigated materials. For the preparation of the rotation disk electrode, catalyst ink is applied directly onto the surface of the working electrode and dried. An additional thin ionomer layer can also be added on top of the catalyst layer to enhance the adhesion [122]. Another way is to prepare a half-cell electrode by hot-pressing gas diffusion electrode on one side of membrane, and then a device was used to hold it with the other side of membrane exposed to the solution. WE

forms a current circuit with a counter electrode, as shown in Figure 1.7. As a current flows, reaction occurs on both electrodes. The most commonly used CE is a piece of Pt coil or sheet with a surface area much larger than that of WE, to ensure that the electrochemical reaction occurring on it is fast enough so that it would not impede the electrochemical reaction occurring on WE. Meanwhile, in order to minimize the impact of the electrolyte solution on the potential of WE, a reference electrode is used to form another circuit with WE. Ideally, RE is non-polarizable and maintains a stable potential, such as normal hydrogen electrode (NHE, Pt/ H_2/ H^+, 0.000 V), saturated calomel electrode (SCE, Hg/ Hg_2Cl_2/ Cl^-, 0.241 V) and silver chloride electrode (Ag/ AgCl/ Cl^-, 0.191V). It is typically hosted in a Luggin capillary whose fine tip can be placed very close to the surface of the working electrode to minimize the impact of the uncompensated electrolyte resistance [1].

The liquid electrolyte used in fuel cell electrode investigation is a dilute aqueous acid solution (e.g. 0.1–1 M), which involves protons, to imitate the fuel cell reactions. Sulfuric acid (H_2SO_4) has been used in many studies, but sulfate anions (SO_4^{2-}) can adsorb onto the surface of the Pt catalyst and affect the reaction kinetics. Perchloric acid ($HClO_4$) offers a better choise, because perchlorate anions (ClO_4^-) do not adsorb onto the surface of Pt catalysts. Since perfluorosulfonic acid ionomer such as Nafion is normally used in CL, trifluoromethane sulfonic acid (CF_3SO_3H) is expected to behave more closely to the ionomer than the inorganic acids. In addition, CF_3SO_3H and its anion ($CF_3SO_3^-$) do not adsorb onto the catalyst and have therefore no effect on the reaction kinetics [1].

In the three-electrode system, the liquid electrolyte temperature, gas flow rate, the inlet and the outlet pressures should be controlled: the flow rate of the gaseous reactant can be measured by a flow meter or a mass flow controller; the inlet and back pressures of the reactant can be managed by pressure regulators. The RH of the half cell system could be regulated by passing the reactant through a humidifier at a pre-determined temperature, such as a sparging bottle containing water.

Half cell is a useful device to mimic the complete polymer electrolyte fuel cell. Electrochemical mehods, such as Cyclic voltammetry (CV), electrochemical impedance spectroscopy (EIS) and linear sweep voltammetry (LSV), have been used to obtain rapid evaluation of the fuel cell material. CV has been frequently used to estimate the surface area of Pt/C catalysts by adsorption of atomic hydrogen in acidic media.

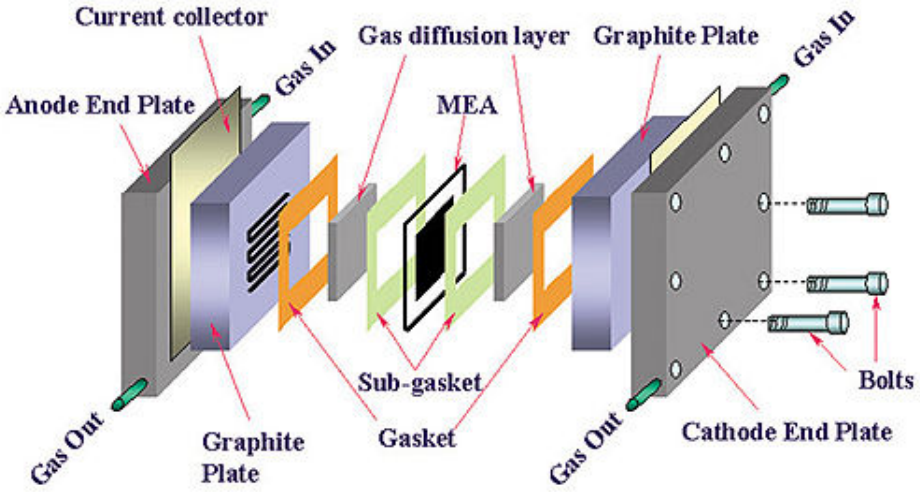

Figure 1.8: A single Fuel cell[124]

1.4.2 Fuel cell operation

A single cell

A single cell can be conveniently used to test a membrane electrode assembly. A sketch of a single PEM fuel cell is shown in Figure 1.8. There is a end plate, a piston, a plastic plate, an anode current collector, a flow field and a gasket on each side. A bladder, with the inlet and outlet of gas, is the outside shell of a fuel cell, to compress and seal the cell assembly. A plastic plate is used to isolate the bladder from the flow field and current collector. Gaskets are used to seal the MEA and prevent the leakage of the reactants.

The flow field, typically made of graphite materials with high corrosion resistance, always plays a critical role in fuel cell. Those made of metallic materials, coated by a corrosion-resistant material, such as gold or metal nitride, could also be used as the current collector. It is recognized that the surface characteristics of the plates have a significant impact on the fuel cell performance, stability and durability [123]. Both highly hydrophilic and hydrophobic surfaces help water removal from the flow-field. On hydrophilic plates, water tends to form a thin layer on it, which would favor the evaporation and removal of water. On the other hand, liquid water has a low affinity on the surface of highly hydrophobic plates, so it is readily blown out by the gaseous exhaust. Moreover, the flow field design, including the the length, width, depth, as well as the flow pattern of the channel, has significant impact on the fuel cell performance. The essential requirement for flow field design is uniform distribution

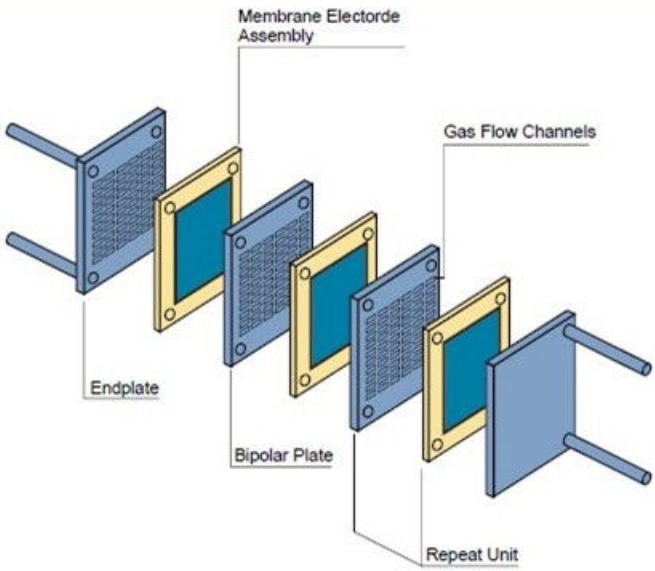

Figure 1.9: A fuel cell stack[125]

of the reactant gases over the respective active electrode surface. A non-uniform distribution will result in a non-uniform current density distribution, leading to low catalyst utilization, low energy efficiency, and a reduced cell life. For a typical planar PEMFC design, feeding channels are designed in structures: serpentine, parallel, or interdigitated. Serpentine flow fields with twists and turns for the flow of the reactants, corresponding to longer paths than straight channels, have large pressure losses between the inlet and the outlet, which could facilitate the remove of liquid water and reduce the risk of flood [1].

Fuel cell stack

Single cells produce electricity with a voltage lower than 1 V, which is far from enough to power a vehicle. In order to produce higher voltages, multiple cells are assembled into a fuel cell stack with the supply of gas in a parallel and/or a series mode. In a parallel gas supply fuel cell stack, all cells are fed in parallel from a common hydrogen/ air inlet. In the serial configuration the gas from the outlet of the first cell is fed to the inlet of the second cell and so on until the last cell, which helps to prevent non-uniform gas distribution. A fuel cell stack in series is shown in Figure 1.9. Bipolar plates, made of graphite or stainless steel with suitable surface treatment, are designed to connect the single cells. It makes electrical connections between one cathode and the anode of the next cell, meanwhile, it serves as the flow field of oxygen to the cathode and fuel gas to the anode [1].

For fuel cell stacks, a test station is required to assist the fuel cell operation by i) controlling the work situation : temperature, pressure, humidity, and flow rates of reactants and the coolant, and ii) measuring the current and voltage of the fuel cell. Usually, a test station system consists of gas control station, load bank, data acquisition/control unit, as well as control software[126, 127]. Sometimes, a coolant subsystem is needed, especially for large surface fuel cell stack testing. The gas control stations (including gas meter unit and humidifier) are used to regulate the gas flow to the cell inlet.[126, 127]

Chapter 2

Materials and methods

In this part, we have introduced the materials and investigation methods applied to this work. First, the preparation of Pt/ Vulcan catalyst and the following functionalization, carried out in IJL, has been explained. XRD and TEM have been used in the characterization of the catalysts before and after the sulfonation step. The half-cell disks, with various catalysts, Nafion amount and GDL types have been fabricated in IJL. For MEA preparation, the electrodes with different components have been used as the cathodes in PEM fuel cells. They were hot-pressed with commercial electrodes, as anodes, in LEMTA.

Both half cell system and a single cell station have been applied in the investigation of electrochemical performances. The electrochemical methods, such as cyclic voltammetry (CV), linear sweep voltammetry (LSV) , chronopotentiometry and electrochemical impedance spectra (EIS), have been used. The principle of each method and the condition applied was introduced in this chapter.

2.1 Sulfonated Pt/ Vulcan catalyst

The development of sulfonated Pt/ Vulcan catalysts aims at reducing the ionomer addition in the electrode, while improving the electrochemical activity. Two sulfonation methods of Pt/Vulcan catalyst are considered, involving the grafting of sulfonated functions with a longer or a shorter spacer, as shown in Figure 2.1.

The preparation of the Pt/ Vulcan catalysts and their functionalization were carried out in IJL. The deposition of platinum particles onto Vulcan® XC-72R was carried out by polyol method: 1g Vulcan was dispersed in 100 mL ethylene glycol in a 3-neck round-bottomed flask equipped with a condenser. A solution of 0.6 g $H_2PtCl_6 \cdot 6H_2O$ in 20 mL deionized water was added drop by drop under inert at-

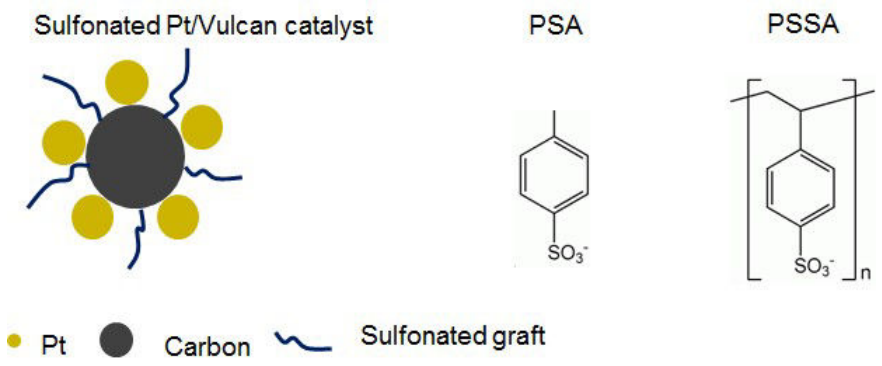

Figure 2.1: Sulfonated Pt/Vulcan catalysts

mosphere. The pH was adjusted to 11 and the mixture was then heated at 140°C for 3 hours. The resulting dispersion was finally filtered and dried overnight. As all the $H_2PtCl_6{\cdot}6H_2O$ was converted to Pt, the Pt content deposited on 1 g Vulcan was around 0.23 g, 19 wt.% of the catalysts.

2.1.1 Preparation of PSSA-Pt/ Vulcan catalyst

Sulfonation of Pt/ Vulcan catalysts with PSSA were achieved by in-situ radical polymerization method as described by Du et al. [115]. A mixture of 500 mg Pt/ Vulcan catalyst, 100 mL distilled water and sodium styrene sulfonate (25, 50 and 100 mg, respectively) was stirred for 10h. The initiator, potassium peroxodisulfate, was added and then the flask was heated to 65°C. After 48h, the dispersion was filtered and washed with distilled water. The solid obtained was poured into a flask and stirred with concentrated sulfuric acid for 24h to exchange sodium for proton. The mixture was filtered, washed with distilled water and dried in an oven at 100 °C for 48h.

The weight amounts of sodium styrene sulfonate in comparison to the mass of catalyst introduced in the vessel were 5, 10 and 20wt.%, respectively. Elemental analysis of the modified catalyst yielded the amount of sulfur: after subtraction of the sulfur quantity contained in the pristine Vulcan material, the amount of sulfur grafted during the sulfonation step was shown to be very close to that introduced in the reactor. The contents of sulfonate groups were around 0.24, 0.48 and 0.96 mmol per 1g catalysts.

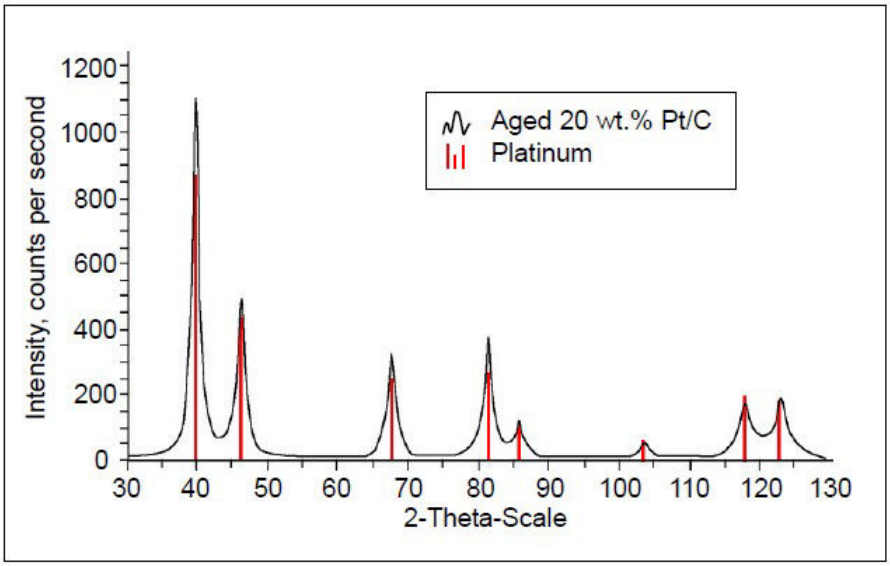

Figure 2.2: XRD data for an aged 20wt.% platinum/carbon electrocatalyst from [129]

2.1.2 Preparation of PSA-Pt/ Vulcan catalyst

PSA functionalized Pt/ Vulcan catalysts were prepared via diazonium ion reduction, developed by Weissmann et al. [128]. The experimental conditions must be carefully controlled because the reactions may be highly exothermic and cause the deterioration of the carbon support and platinum particles.

A suspension containing 4-aminobenzene sulfonic acid (17.5, 35.0, 54.0, or 70.0 mg), 50mL of 0.5M HCl and 300 mg of Pt/Vulcan catalyst was stirred for half an hour. Then, $NaNO_2$, up to a concentration twice that of 4-phenysulfonic acid, was dissolved in 15 mL water and added drop-wise to the suspension. This mixture was stirred for 24h and then filtered and rinsed thoroughly with deionized water. The washed residue was then placed in an oven at 100°C for 48 h. The weight amounts of 4-aminobenzene sulfonic acid were 5.8, 11.6 18.0 and 23.3wt.% of the mass of catalyst, corresponding to the amounts of grafted sulfonate groups around 0.32, 0.62, 0.98 and 1.3 mmol per gram of catalyst, respectively.

2.2 Methods for characterizing the prepared catalysts

2.2.1 X-Ray Diffraction (XRD)

X-ray crystallography (XRD) is a non-destructive characterization technique to determine the atomic and molecular structure of a crystal. A beam of monochromatic X-rays of known wavelength, generated by the filament X-ray tubes, passes through difference limiting slit, bombards the sample at a certain angle and reaches the detector through a receiving slits. Spots appearing in specific directions are observed on the diffraction pattern.

XRD, carried out in Institute Jean Lamour, has been used to determine the morphology and crystallinity of the Pt/ Vulcan catalyst. The dispersion and the mean size of the platinum particles is identified along with the results in TEM images. The super-Lorentzian peak shapes of a pure platinum and aged Pt/C are presented in Figure 2.2 [129].

2.2.2 Transmission electron microscopy (TEM)

Transmission electron microscopy (TEM) is a microscopy technique in which a beam of electrons is transmitted through an ultra-thin specimen, interacting with the specimen as it passes through. The electrons are generated by a process called thermionic emission from a tungsten filament and are aligned and accelerated as they pass through numerous intermediate and projector lenses. As they cross through the specimen, an image is formed from the interaction; the image is magnified and focused onto the imaging device, such as a fluorescent screen, on a layer of photographic film, or to be detected by a sensor such as a charge-coupled device camera [130].

In this study, TEM was utilized to view the surface morphology of the Pt/ Vulcan catalyst before and after the functionalization, to verify the presence and dispersion of platinum particles on the carbon support. This was performed on a TEM CM20 (200 kV). A small amount of sample powder is dispersed in ethanol by ultrasound. A drop of the suspension thus obtained is deposited on a copper grid and dried in air. The grid is then placed on a single tilt sample holder introduced into the column microscope. The microscope used is coupled to a spectrometer dispersion wavelength (EDS) to analyze the local composition of the samples.

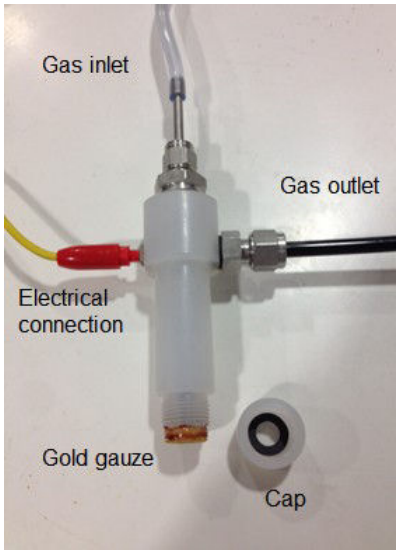

Figure 2.3: Working electrode device for half-cell test

2.3 Half cell investigation

2.3.1 Half-cell electrodes

The half-cell electrodes, with sulfonated Pt/ Vulcan catalysts and various Nafion distribution, were loaded onto two GDLs: carbon paper (CP) and micro-porous layered carbon paper (MCP).

For the preparation of CP-electrodes, catalyst ink, containing 16 mg catalyst, 50 μL deionized water, Nafion® dispersion (0, 40 or 80 μL, in water, 10wt.%, Aldrich Chemical) and solvent (280 μL isopropanol and 280 μL glycerol), was ultra-sonicated for 30 min, and then coated on a Teflon impregnated carbon paper (Toray Carbon Paper TGP-H-60). The catalyst ink was pipetted, 70 μL, and deposed on the two GDLs, respectively, in the form of 14 mm disks. From the amount of ink deposited, the Pt loading was estimated to be 0.20±0.02 mg·cm^{-2}and the Nafion amount is 0, 0.25 and 0.50 mg·cm^{-2}, as 0, 40 and 80 μL Nafion® dispersion was added in the ink, respectively. For the fabrication of the Nafion coated electrodes, Nafion dispersion was deposited onto the dried CL.

In the fabrication of MCP-electrodes, Teflon incorporated carbon papers with a micro-porous layer, SIGRACET® 10BB, was used as GDL. Because of the micro-porous layer on carbon paper, a solvent, 560 μL isopropanol, was used to prepare a catalyst ink with lower viscosity. The catalyst ink was also ultra-sonicated and then deposed on MCPs. The prepared disk, dried at ambient temperature, was then hot-pressed onto Nafion® membrane NRE-212. Electrodes hot-pressed at various

condition have also been fabricated, in the region of 135-140°C, 35-50 bar, 4-10 min.

The influence of electrode composition, graft ratio, Nafion amount and GDL type was investigated in half-cells. More than 3 electrodes pieces with the same components were prepared and tested to obtain repeatable data in the electrochemical studies.

2.3.2 Half-cell device

As described in Chapter 1, half-cell is a simple and rapid method to characterize the MEA materials in electrochemical mode. Prepared electrodes were studied as working electrode in a device, first designed by CEA (Le Commissariat à l'énergie atomique et aux énergies alternatives) then developed by Institute Jean Lamour, as shown in Figure 2.3. A half-cell disk, with the backside of carbon paper connected to the gold gauze (the current collector) and the membrane in contact with the liquid solution, was placed in the cap. The surface area exposed to the solution is 0.503 cm^2 (diameter 8mm).

The gas flow was controlled by a flow meter, at around 60 $mL \cdot min^{-1}$. The gas pressure in the working electrode was controlled by a bubbler. The height of the water in the bubbler was around 7cm.

Figure 2.4 presents the three-electrode system in 0.5 M H_2SO_4 solution. A stop-cock was used to regulate the gas feeding into the solution. The reference electrode was a saturated mercurous sulfate Hg/ Hg_2SO_4, with a potential at 0.69 V/NHE, placed in a Luggin capillary, and the counter electrode was a platinum electrode. The three electrodes are connected to the potentiostat VoltaMaster 402.

2.4 Fuel cell investigation

2.4.1 MEA preparation

The catalyst ink containing catalyst, deionized water, Nafion dispersion and solvent isopropanol, was ultra-sonicated and then sprayed onto a Teflon incorporated carbon paper with a micro-porous layer (SIGRACET® 10BC) with a airbrush (Colani, Harder & Steenbeck). The amount of catalyst ink required for 15cm^2 GDL is 1000µL, corresponding to a Pt loading around 0.3 $mg \cdot cm^{-2}$. Due to the loss of ink in the spray, the obtained MEAs have actually a Pt loading around 0.2±0.02 $mg \cdot cm^{-2}$. A prepared GDE (cathode) and a commercial electrode (anode, Paxitech, Pt loading of 0.5 $mg \cdot cm^{-2}$) of 2.5×3cm^2, was hot-pressed on the two sides of Nafion® membrane NRE-212 at 135°C, 35 bar, 3min to obtain the cell MEA.

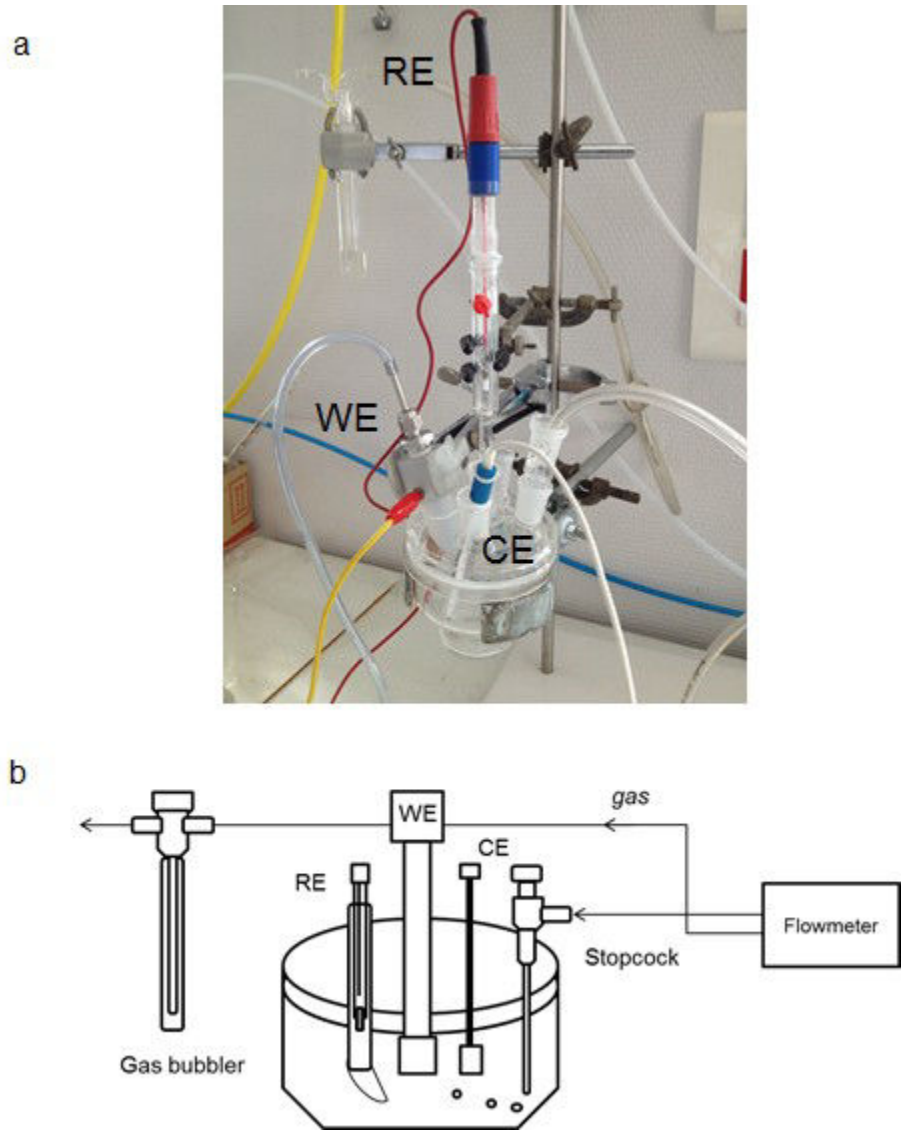

Figure 2.4: The half-cell test system

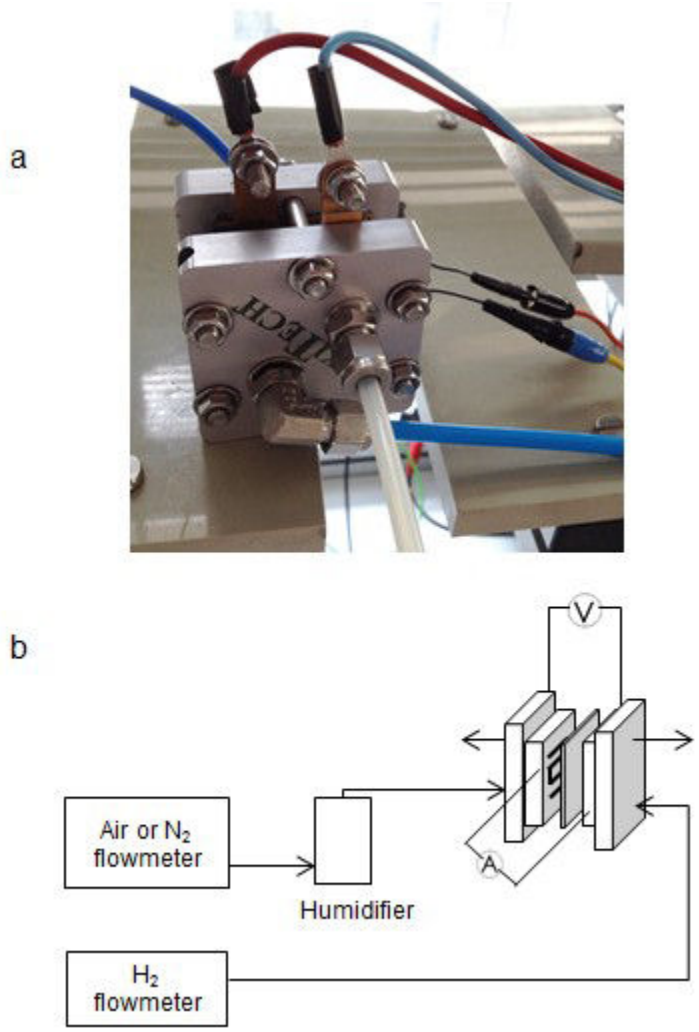

Figure 2.5: The single cell test system

The electrochemical performances were carried out in more than 2 pieces MEAs with the same component to ensure the repeatability of the measurements.

2.4.2 Fuel cell device

A single 5cm^2 cell of from Paxi Tech was used in our test. The cell consists of aluminum end-plates, graphite monopolar plates and single channel serpentine gas flow field (1mm x 1mm), gold plated copper current collector plates. The fuel cell was heated with two heating cartridges, diameter 6.5 mm, which were inserted into the holes provided in the aluminum end plates.

The proton conductivity of the Nafion membrane is directly proportional to the water content. Air supplied to the cathode passed through a bubble chamber full of

deionized water. The humidified air was driven to the interface between the cathode and the membrane. Water diffused from the cathode side to the anode, and a suitable state of hydration of the membrane could be achieved [3].

The humidification of air was expressed by the saturated vapour pressure, which is the partial pressure of water in saturated air at the considered temperature. Therefore, the relative humidification of a fuel cell operation was given by:

$$\phi_H = \frac{P_H}{P_W} \times 100\% \tag{2.1}$$

where P_H is the saturated vapour pressure in the humidifier, and P_W is saturated vapour pressure in the fuel cell, depending on the working cell temperature, respectively.

In our fuel cell tests, both the humidifier and fuel cell were working at ambient temperature (25^{o}C), and ϕ_H was equal to 100%.

The usage of the cathode and anode reactants can be calculated based on Faraday's law. According to Equation 1.3, for each mole of oxygen, four electrons are transported, the flow of O_2 or air (mol/s) is:

$$F_{O_2} = \frac{I}{4F} \tag{2.2}$$

$$F_{air} = \frac{I}{4F} \cdot \frac{1}{0.21} \tag{2.3}$$

Since for each mole of oxygen, four electrons are transported, the flow of H_2 (mol/s) is equal to:

$$F_{H_2} = \frac{I}{2F} \tag{2.4}$$

The reactant flow rate at the inlet must be equal to or higher than the theoretical consuming rate of the reactant in the fuel cell reaction. Stoichiometric rate is the stoichiometric gas factors, λ_{air} and λ_{H_2} , were defined. The flow rates (mol/s) are :

$$F_{air} = \lambda_{air} \cdot \frac{I}{4F} \cdot \frac{1}{0.21} \tag{2.5}$$

$$F_{H_2} = \lambda_{H_2} \cdot \frac{I}{2F} \tag{2.6}$$

The molar volume of an ideal gas at 25°C, 1 atm, is 24.5 L/mol. The volume flow rates (ml/min) are

$$F_{air} = 18.1\lambda_{air}I \tag{2.7}$$

$$F_{H_2} = 7.6\lambda_{H_2}I \tag{2.8}$$

In the tests presented here, the stoichiometric factor of H_2 and air were at 1.5 and 2, respectively. At 2A, the flow rates of H_2 and air are 23 and 72ml/min, respectively.

2.5 Electrochemical measurements

The electrochemical properties of half cell electrodes were tested in a three-electrode system using a potentiostat (Voltalab PGZ 402). The MEA investigation was carried out on a potentiostat (Autolab PGSTAT20) with a booster (Autolab BSTR 10A).

2.5.1 Polarization Curves

In half-cell mode, the polarization curve (current-voltage) in ORR of each electrodes has been studied by linear sweep voltammetry (LSV). It was employed with air feed to determine the performance of ORR between -50 mV and 850 mV/ NHE with a scan rate of 5 $mV{\cdot}s^{-1}$. The potential given in the LSV plots, called measured potential, E_m (mV/ NHE) is not the real potential at the working electrode, E_r (mV/ NHE). The potential drop, ΔE, between the half-cell device and RE, had to be subtracted from E_m , to obtain the real potential E_r (mV/ NHE).

$$E_r = E_m - \Delta E \tag{2.9}$$

In the present case, the potential drop mainly results from the ohmic resistance, R_Ω, obtained in EIS.

In fuel cell test, polarization curve is the most common indicator for fuel cell performance. The chronopotentiometry procedure has been applied by adjusting the current density (i) in a logarithm variations. Every current density step is lasted for 1 min and the cell voltage is recorded. After a series of current and voltage values are collected, the cell voltage will be plotted as a function of current density. MEA power density, equal to the $i \cdot E$ can be plotted as a function of current density, accordingly.

2.5.2 H_2 crossover

In PEM fuel cell, membranes are used as the electrolyte to transport protons from the anode to the cathode and a barrier of electrons and reactants on each sides of the cell. However, gases inevitably diffuse through the membrane, due to concentration and pressure gradients, especially in thin membranes pursued for their significant electrical efficiency benefits [135]. H_2 permeates from the anode to the cathode, as well as nitrogen and oxygen transfer from the cathode to the anode side . As hydrogen transfer through the membrane and reacts directly with oxygen at the cathode, the open circuit of the fuel cell decreased. In the fuel cell investigation, hydrogen crossover, in result of the degradation of membrane, causes the inefficiency of a fuel cell [131, 132, 133].

Linear sweep voltammetry (LSV) is the most frequently used electrochemical method to estimate the gas crossover though the membrane. A LSV curve on MEA containing 18.0 wt.% PSA grafted catalyst and 0.5 mg·cm^{-2} Nafion after 2000 cycles is shown in Figure 2.6. H_2 and N_2 is supplied to the anode and the cathode, respectively. A linear potential scan, in a potential range (e.g. 0-0.5 V), with a low scan rate (e.g. 4 mV·s^{-1}), is applied to the fuel cell electrodes[134]. The current recorded is due to the electrochemical oxidation of H_2, permeating though the membrane from the anode. As shown in Figure 2.6, the hydrogen crossover current attains a limiting value, around 0.3-0.35V, due to the mass transfer limitation [135].

The hydrogen crossover rate J_{H_2} (mol·s^{-1}·cm^{-2}) can be determined by Faraday's law,

$$J_{H_2} = \frac{i_{H_2}}{nF}$$

where $i_{H_2}$the hydrogen crossover current density, equal to the limiting value shown in LSV; the number of electron, n, for HOR, is equal to 2; F is Faraday's constant (96485 C·mol^{-1}).

The LSV investigation was used to evaluate the membrane degradation during the ageing test at room temperature. The gas flux rate of H_2 and N_2 is 60 ml·min^{-1}. A linear potential was scanned from 0.05 to 0.5V, with a scan rate of 2 mV/s,

2.5.3 Electrochemical surface area ($ECSA$)

The electrochemical surface area ($ECSA$, m^2·g^{-1} catalyst), also called electrochemical active surface (EAS, m^2·g^{-1} catalyst), is an important factor to evaluate the activity

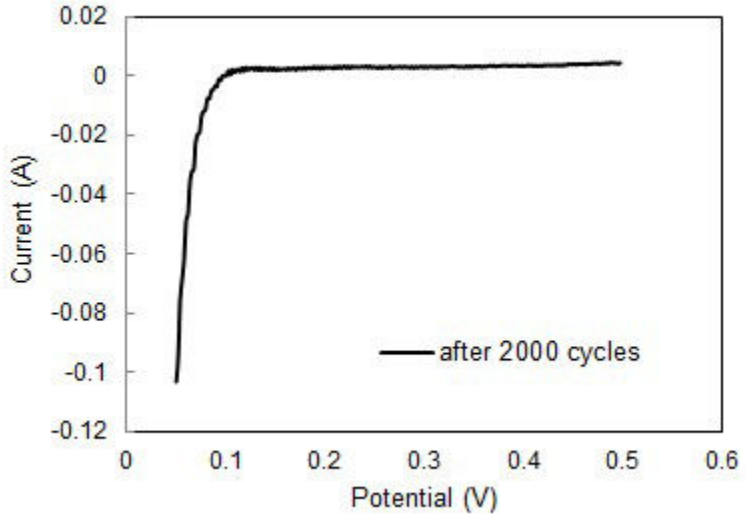

Figure 2.6: Linear sweep voltammogram on MEA containing 10 mmol·g^{-1} PSA grafted catalyst and 0.5 mg·cm^{-2} Nafion after 2000 cycles, with a scan rate of 2mV·s^{-1}, at room temperature

of Pt catalysts. The value can be measured by cyclic voltammetry (CV), which is one of the most widely used electrochemical techniques to study the equilibrium potentials of redox reactions and the kinetics of heterogeneous electron-transport reactions, as well as coupled chemical adsorption and reactions [1].

Figure 2.7 shows a typical CV curve on Pt/Carbon catalysts. The peaks above the current axis at 0.05-0.45 V/NHE for increasing voltages correspond to the hydrogen adsorption on Pt (100) and Pt (111) crystal surfaces with adsorption charge:

$$Pt + H^+ + e^- \rightarrow Pt - H_{ad} \tag{2.10}$$

In the same potential region, peaks appearing below the current axis presents the hydrogen desorption on Pt (100) and Pt (111) crystal surfaces, with a hydrogen charge, a Volmer route in Equation 1.7.

The oxidation peak starting from 0.8 V/NHE corresponds to the oxidation of platinum:

$$Pt - H_2O \rightarrow PtO + 2H^+ + 2e^- \tag{2.11}$$

Therefore, the peak between 0.8-0.5 V/NHE is related to the reduction of platinum oxide

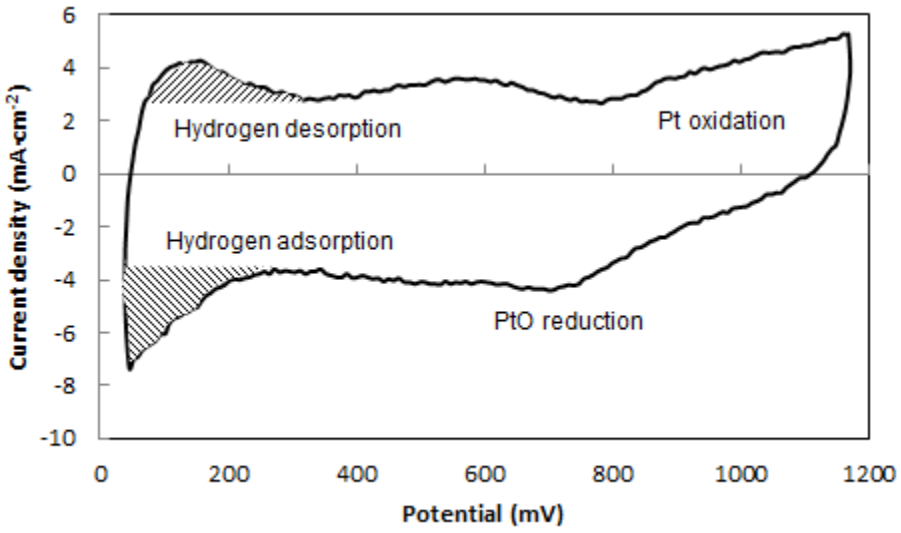

Figure 2.7: Hydrogen adsorption/desorption curve of the half-cell (prepared with 5wt.% PSSA grafted Pt/Vulcan catalyst and 0.50 mg·cm^{-2} Nafion in the catalyst layer) after 100 cycles from 0-1.2V with a scan rate of 50 mV·s^{-1}

$$PtO + 2H^+ + 2e^- \rightarrow Pt - H_2O \tag{2.12}$$

Therefore, $ECSA$ (m^2·g^{-1}) can be estimated by integration of the hydrogen adsorption or desorption peak after subtraction from the double layer charging current in the potential range 0.05-0.45V/NHE, and assuming a charge value of 0.210 mC·cm^{-2} for the oxidation of a monolayer of adsorbed hydrogen on polycrystalline Pt (atom surface density of 1.3×10^{15} atoms per cm^2).

$$ECSA = \frac{Q_H}{0.21 \cdot L_{Pt}} \tag{2.13}$$

where, Q_H is the average of adsorption and desorption charge estimated, mC·cm^{-2}, and L_{Pt} is the Pt loading in the electrode, around 2.0 g·m^{-2} in prepared GDEs.

In the three-electrode system, hydrogen adsorption/desorption curves have been obtained by cyclic voltammetry (scan rate 50 mV/s, in the range 0.05-1.2 V/NHE).

The Pt utilization is defined as:

$$u_{Pt} = \frac{ECSA}{S_{tot}} \tag{2.14}$$

where S_{tot}, the total surface area, is obtained from the mean particle size, assuming the Pt particles are spheres with surface area $4\pi r^2$.

$$S_{tot} = \frac{1}{{}^{4}/_{3}\pi r^3 \cdot \rho} \cdot 4\pi r^2 = \frac{3}{r\rho} \tag{2.15}$$

where the radium of the platinum particles, was estimated at 2 nm, as detected in XRD and TEM, ρ is the density of platinum, 21.45 g·cm^{-3}. So we obtain S_{tot}=70.0 m^2·g^{-1} .

2.5.4 Electrochemistry Impedance Spectra (EIS)

Electrochemical impedance spectroscopy, EIS, is a technique used for investigating the double-layer capacitance of an electrode/ electrolyte interface, in addition to giving access to both diffusion and charge transfer resistance. A small AC amplitude perturbation is added to a constant direct current or potential signal with a changing frequency. By scanning the frequency, the impedance change can be recorded and each component value can be obtained for all frequencies investigated [2].

As a sinusoidal current density $i(t)$ with an amplitude i', in mA·cm^{-2}, is applied between WE and CE, the corresponding sinusoidal $E(t)$, with an amplitude E' in mV, between the WE and the RE is recorded. The impedance $Z(t)$, in Ω·cm^2 is defined as the impedance

$$i(t) = i'sin(wt) \tag{2.16}$$

$$E(t) = E'sin(wt + \psi) \tag{2.17}$$

$$Z(t) = \frac{E(t)}{I(t)} \tag{2.18}$$

where w is the pulsation (rad·s^{-1}) and ψ is the phase (rad).

EIS applied in the fuel cell tests is to obtain the detailed information in a broad range of characterized time (equal to the reciprocal of the frequency). Here the reference electrode is the anode, so the signal recorded covers the two electrodes of the cell. The processes occurring in the fuel cell electrode/ membrane surface mainly involve adsorption of electroactive species, charge transfer at the electrode surface, proton transfer in electrolyte, and mass transfer to the electrode surface. Each process can be represented as an electric component and the whole reaction is often modeled by an electric circuit composed of resistances, capacitors, or constant phase elements combined in parallel or in series. The various electric components are briefly presented

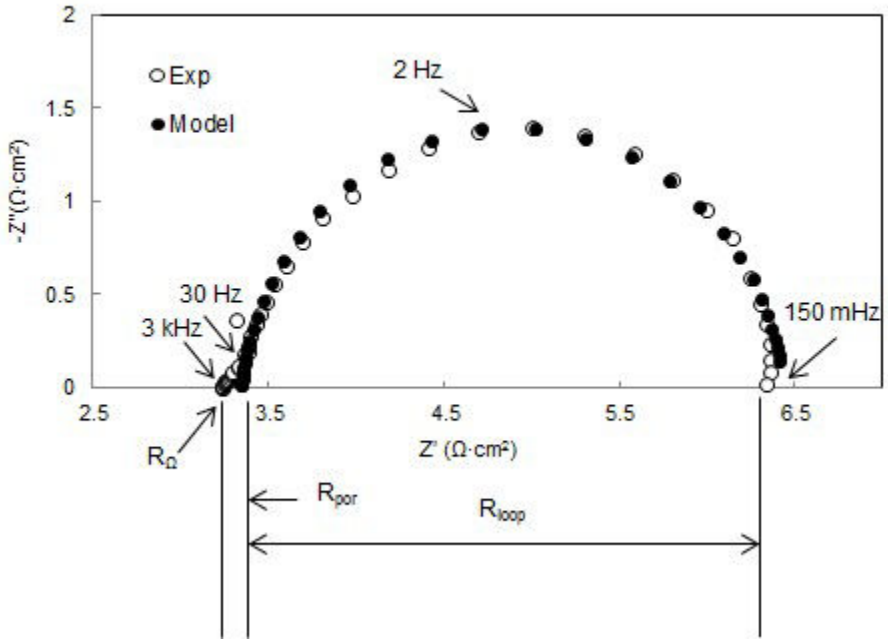

Figure 2.8: Impedance spectrum of a half cell at 10 mA·cm^{-2}(Exp) and the fitted spectrum (Model)

below:

Ohmic resistance

In general, the intercept at high frequency ($>$ 1 kHz) is associated with its ohmic resistance R_Ω (Ω·cm^2). In half cell mode, the liquid solution between WE and RE, as well as the interface of membrane-CL, contributes to the ohmic resistance. In fuel cell tests, it consists of the membrane resistance, contact resistance of the different layers and those of cables and electrical connectors[137, 138].

Charge transfer resistance

Charge transfer resistance is defined as the derivative of the potential with respect to the current density at constant concentration of reactants at the interface:

$$R_{ct} = \frac{\partial E}{\partial i} = \frac{\partial \eta}{\partial i} \tag{2.19}$$

In high overpotential range, η is limited to current density i, given by Tafel's law, Equation 1.24. Therefore, R_{ct} can be shown to be a decreasing function of the current density as:

$$R_{ct} = \frac{RT}{n\alpha F} \cdot \frac{1}{i} \tag{2.20}$$

where n is the number of electrons involved in the rds. R_{ct} varies linearly to $1/i$ for sufficient overpotential (in absolute value), with a slope equal to $b/2.303$.

R_{ct} ($\Omega{\cdot}cm^2$) is a resistance term linked to the reaction kinetics. In half-cell investigations, R_{ct} of ORR was depicted in the impedance plots. In the studies in fuel cell reaction, the anode resistance $R_{ct,a}$ is often 5-10 times lower than the resistance in the cathode $R_{ct,c}$, so we fixed $R_{ct,a}$ at one tenth of $R_{ct,c}$ in the fitting.

Diffusion impedance

Diffusion impedance, Z_d ($\Omega{\cdot}cm^2$) is due to the diffusion and convection of reactant occurring in the vicinity of the electrode. Compared to the charge transfer, the diffusion of reactant is relatively slow, so usually observed at low frequency. Depending on the variety of reactant concentration in diffusion layer, different models have been applied in the description of the diffusion impedance [2]. In our case, we use the model of a linear but finite diffusion, where the concentration is constant in the electrolyte and varies linearly in the diffusion layer. The diffusion impedance element is symbolized by W with an impedance [137]:

$$Z_W = R_d \frac{tanh(\sqrt{j\tau_d w})}{\sqrt{j\tau_d w}} \tag{2.21}$$

where R_d ($\Omega{\cdot}cm^2$) is the diffusion resistance, τ_d is the characteristic diffusion time, depending on the thickness of the layer and gas diffusion coefficient.

Constant phase element

The constant phase element (CPE) is used to replace double layer capacitance, taking into account the electrode surface roughness or distribution/ accumulation of charge carriers. The parameters Q ($F{\cdot}rad^{1\text{-}n}{\cdot}s^{1\text{-}n}$) and n ($rad{\cdot}s^{-1}$) are the pseudo-capacity and pulsation, respectively. The impedance of a CPE is expressed as:

$$Z_{CPE} = \frac{1}{Q(jw)^n} \tag{2.22}$$

Depending on the frequency of the fluctuating signal, more or less current accumulates into the pores on the double layer. The parameter n reflects the deviation from real capacitance: the closer to 1, the electrode is more flat. The equivalent double layer capacity can be estimated with the formula given below [137]:

$$C_{eq} = (2\pi f_{top})^{n-1} \cdot sin(\frac{n\pi}{2}) \cdot Q \tag{2.23}$$

where f_{top} is frequency at the summit of the high frequency loop.

In experimental work, both potentiostatic EIS and galvanostatic EIS procedure have been applied within the frequency range of 10 kHz -50 mHz. For the first one, the working electrode potential is modulated sinusoidally with respect to the RE. The corresponding sinusoidal current flowing between the WE and the CE was recorded. Half cell electrodes were studied by potentiostatic EIS in the range of 250-600 mV/NHE, with am amplitude of 10 mV. In galvanostatic EIS procedure, the impedance spectra at various reduction currents were measured, with 10% amplitude of the steady current.

A typical impedance spectrum of a GDE mounted in the half-cell system is presented in Figure 2.8, consisting a 45° inclined linear part at high frequency followed by a large loop at medium and low frequency. The intercept on Z' part at high frequency, corresponds to R_Ω. The high-frequency 45° angle line has been attributed to the porous structure of the electrode by Hitz [136]. In the two equivalent circuits for half cells, shown in Figure 2.9(a) and (b), Z_{por} is the porosity impedance. R_{por} presents the porosity resistance, equal to the real part of the 45° angle line.

The impedance of model (a) is:

$$Z(w) = R_\Omega + R_{por} + \frac{1}{Q(jw)^n + R_{ct}^{-1}} \tag{2.24}$$

Equivalent circuit (a) is based on the conventional Randles model, in which a double layer capacity is in parallel with a charge-transfer resistance R_{ct}. CPE (Q, n) was used to replace the double layer capacitance.The Nyquist plot of circuit (a) is a compressed half-circle, whose intercept at high frequency is equal to the sum of R_Ω and R_{por}. When the intercept of the real Nyquist plot is subtracted, R_{por} is estimated.

The impedance of model (b) is:

$$Z(w) = R_\Omega + R_{por} + \frac{1}{Q(jw)^n + (R_{ct} + R_d \cdot \frac{tanh(\sqrt{j\tau_d w})}{\sqrt{j\tau_d w}})^{-1}} \tag{2.25}$$

The two equivalent circuits (a) or (b) are selected for fitting the loop in Nyquist plots depending on whether the diffusion impedance was considered or not .

The equivalent circuit used in a single cell investigation is shown in Figure 2.9(c). At the anode, there are $R_{ct,a}$ the charge transfer resistance and a constant phase

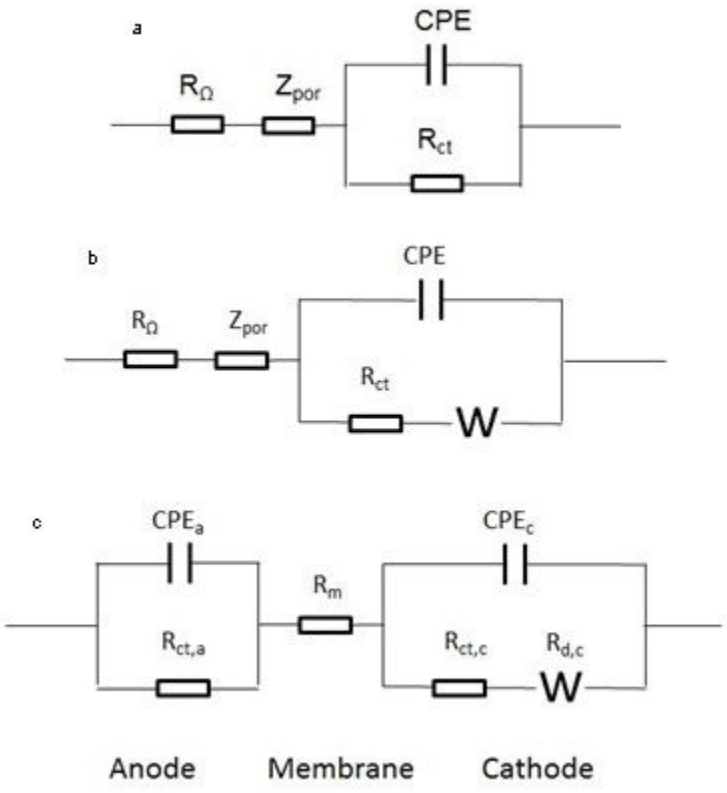

Figure 2.9: The equivalent circuit for ORR in half-cell (a, b) and a single cell (c);

element $\mathrm{CPE_a}$ (Q_a, n_a). R_m is the membrane resistance, which contributes the most part of the ohmic resistance in the system. In the cathode, there are three components, $R_{ct,c}$, $\mathrm{CPE_c}$ (Q_c, n_c) and $Z_{d,c}$ ($R_{d,c}$, $\tau_{d,c}$) with the same meaning as in Figure 2.9(b). The impedance of model (c) is:

$$Z(w) = R_m + \frac{1}{Q_a(jw)^{n_a} + R_{ct,a}^{-1}} + \frac{1}{Q_c(jw)^{n_c} + (R_{ct} + R_{d,c} \cdot \frac{tanh(\sqrt{j\tau_{d,c}w})}{\sqrt{j\tau_{d,c}w}})^{-1}} \tag{2.26}$$

In the EIS measurement, the real and imaginary part of impedance, $Z'(w)$ and $Z''(w)$ at every w are given. In the equivalent circuit established for modeling the real data, $Z'_{model}(w)$ and $Z''_{model}(w)$ present the real and imaginary part of impedance. The variance, $e(w)$, was used to estimate the difference between the experimental data and those in model:

$$e(w) = \sqrt{(Z'(w) - Z'_{model}(w))^2 + ((Z''(w) - Z''_{model}(w))^2}$$

The fitting was carried out in Excel file with the program "solver" by optimizing each factor in the equivalent circuit to minimize the sum of $e(w)$ in the frequency range.

2.5.5 Durability tests

The durability test is the method carried out to estimate the lifetime of a MEA or a fuel cell stack. The simplest method is to run the fuel cell under regular, actual operation conditions, hour by hour, to record the performance along time. But this method is time-consuming. As the durability of a hydrogen single cells can exceed 10000h, most investigations have been carried out in the order of 2000h. Aging tests at constant current density are only considered for fuel cells under more extreme conditions. Accelerated durability test (ADT) methods, operated under more "stressful" conditions compared to actual using conditions, have been developed to accelerate fuel cell failure [139]. Time variation of one electrical variable (E or i), have been applied by driving cycles. Operations with H_2/air (or oxygen) , with cathode potentials below OCV, 0.95-1.0V, have been used to imitate the real fuel cell operation. While inert gas, nitrogen or helium, was supplied to the cathode to reduce chemical corrosion in the presence of air, the carbon corrosion could be studied up to 1.5V [139].

In the research of the DOE Fuel cell program and the USFC in USA, different protocols for cell degradation have been designed in order to isolate the effects and failure mode in a fuel cell, as each component experiences different degradation mechanisms under different conditions [140]. For example, the electrocatalyst cycle is different from the catalyst support cycle. The ageing of catalysts contains by platinum (Pt) sintering, particle growth, and dissolution, especially at high electrode potentials. The protocol for electrocatalyst accelerated stress test was performed by step change for 30000 cycles: 30 s at 0.7 V and 30 s at 0.9 V, in H_2/N_2. The evaluation of carbon support durability is performed with a steady-state potential at 1.2 V for 200 hours. The membrane/MEA chemical degradation is distinguished from the mechanical degradation by RH cycling. The membrane swells at high RH as it absorbs water and shrinks as it loses water at low RH. This swell/shrink cycling results in the mechanical failure, detected by the gas crossover across the membrane.

In nitrogen circumstance, CV in the range of 0-1.2V, with a scan rate of 50 mV/s, was used to investigate the durability of half-cells in 500 cycles. The value of $ECSA$ at every 100 cycles was presented in [141]. In fuel cell operation, while air and hydrogen was supplied to the cathode and anode, CV was applied in the potential range of 0.1-0.9V for 4000 cycles, with a scan rate of 5mV/s. The polarization curves and impedance spectra were recorded every 1000 cycles.

Chapter 3

PSSA grafted Pt/Vulcan catalysts

The Pt/Vulcan catalysts were grafted with PSSA groups by in-situ radical polymerization with 5, 10 and 20 wt.% sodium styrene sulfonate. The dispersion of the platinum particles were investigated by XRD and TEM, before and after the functionalization. The electrochemical properties of the prepared catalysts were then studied in half-cell mode and in a single cell. The effects of graft ratio, as well as the Nafion amount in CL (0.25 or 0.50 $mg{\cdot}cm^{-2}$) and GDL types on the performances in three-electrode system were presented in section 3.2. The values of ECSA were estimated by CV in nitrogen. And the ORR properties were studied by LSV and EIS as air feeding.

MEAs with various catalysts and Nafion addition were prepared and investigated in a single cell tested at ambient temperature (25 ^{o}C), under 100% relative humidification. Their polarization curves and Nyquist plots at various current density (0.05, 0.1, 0.15 and 0.2 $A{\cdot}cm^{-2}$) were presented in section 3.3. At the end, some conclusions were given in the optimum amount of graft ratio and Nafion addition in the CL.

3.1 Physical Characterization

The prepared Pt/Vulcan catalyst was investigated by XRD. The dispersion and the mean size of the platinum particles is identified along with the results in TEM images, with a diameter around 4nm.

The TEM image of Pt/ Vulcan catalyst non-functionalized is presented in Figure 3.1(a), and those of Pt/ Vulcan catalysts with various PSSA graft ratio are shown in Figure 3.1(b-d).

After the sulfonation, no obvious aggregation of Pt particles was revealed in the TEM images. The diameter of platinum particles in sulfonated catalyst presented by XRD remained at around 4nm. It indicated that the polymerization process did not

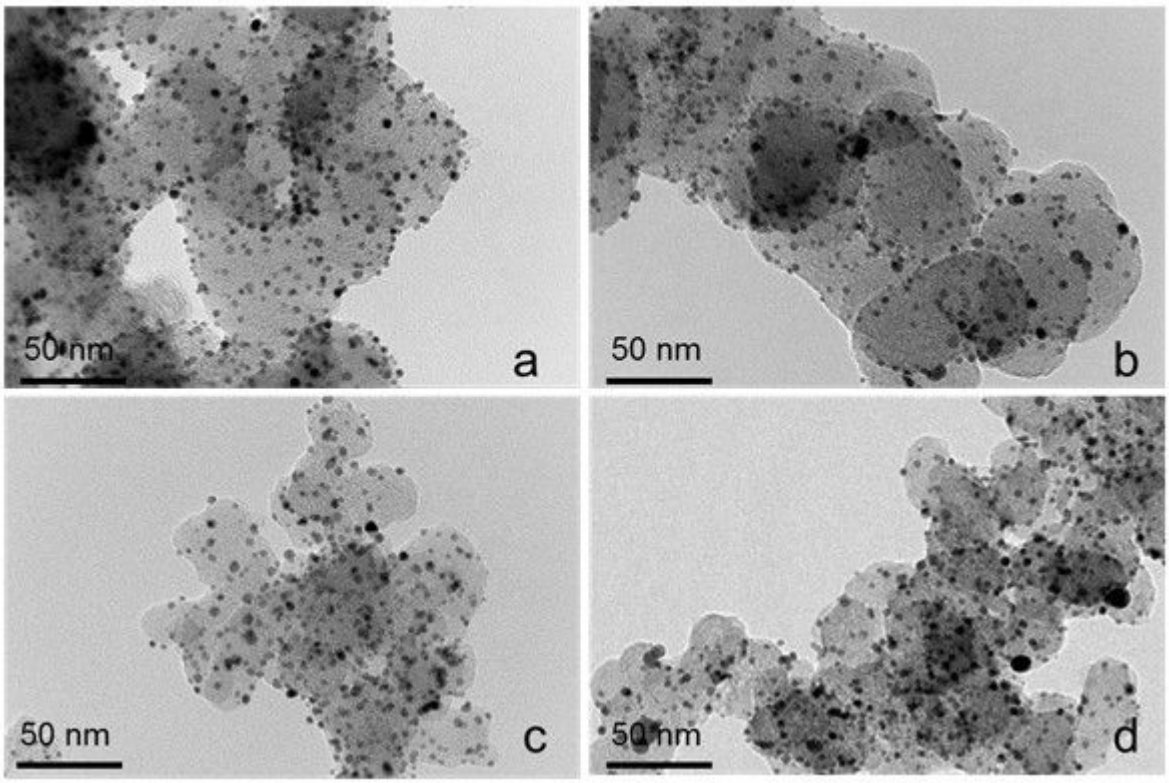

Figure 3.1: TEM images of Pt/ Vulcan catalysts with various PSSA graft ratio: a, 0wt.%; b, 5wt.%; c, 10wt.%; d, 20wt.%

obviously change the particles distribution on Vulcan materials.

3.2 PSSA-catalysts in CP-half-cells

Catalyst inks with different PSSA grafted catalysts and various amounts of Nafion were deposited onto PTFE incorporated carbon paper. The sulfonated Pt/ Vulcan catalysts, grafted with 5, 10 and 20wt.% PSSA, were added to the inks, respectively. The effect of Nafion amount was studied in the GDEs with 100% (0.50 mg·cm^{-2}), 50% (0.25 mg·cm^{-2}) and 0% Nafion added into the catalyst layer, whereas the usual amount is 1.0 mg·cm^{-2}[41]. The prepared electrodes were named of the amount of PSSA and the Nafion percentage, for example, "P5-100" was the GDE prepared with 5wt.% PSSA grafted Pt/Vulcan catalyst and 100% Nafion addition. An electrode with non-functionalized catalyst and 100% Nafion, named 0-100, was used as the reference sample.

Every component effect was studied in more than three half-cell disks in order to

obtain repeatable data. Besides, the repeatability of the measurement significantly depends on the stability of the membrane-CL interface. Hot-pressing condition have been optimized to improve the interface performances, at 135^{o}C, 40bar for 6min [141]. However, membrane hot-pressed onto the GDEs with less Nafion addition in CL tended to bulge out in liquid solution, so the performances of the less-Nafion GDEs , P10-0, P20-50, P20-0, have not been presented in three-electrode system, with an exception of P5-0 and P10-50. In hydrophilic CL, with PSSA grafted catalyst, a minimum Nafion amount is required for mechanical cohesion on the hydrophobic GDL structure. This effect, visible with 10 and 20wt.% grafting, could be less pronounced with only 5wt.% grafting, which could accommodate the GDL with Nafion.

The electrochemical activity of the prepared GDEs were studied by CV. LSV and EIS have been used to investigate the ORR performances in air.

3.2.1 *ECSA* in CP-half-cells

The catalytic activity in each electrode with different Pt/Vulcan catalysts and Nafion amount (0.25 or 0.50 mg·cm^{-2}) was investigated by CV. *ECSA* , based on the desorption charge in hydrogen adsorption/ desorption curves was deduced from CV. The set of data has been given in Figure 3.2. The values of the GDEs without Nafion addition have not been presented because of the unstable membrane-CL interface: the membrane actually absorbed water and bulged out from the surface of CL during the CV cycles.

First, among the four electrodes with 0.50 mg·cm^{-2} Nafion (dark column in Figure 3.2), higher catalyst activities were obtained after sulfonation. The value increased as the graft ratio increased from 0 to 5 wt.%. However, *ECSA* slightly decreased as the PSSA grafting increased to 10wt.%. And the highest *ECSA* was achieved in Pt/ Vulcan catalyst, grafted with 20 wt.% PSSA, around 24 m^{2}·g^{-1}. This variation of P10-100 was in the error range, affected by the dispersion of the catalyst particles in the pores of GDL. In less-Nafion electrodes with 0.25 mg·cm^{-2}, similar influence of PSSA graft ratio on *ECSA* was observed. The sulfonated electrodes performed higher catalyst activities than that of non-functionalized catalyst with 0.25 mg·cm^{-2} Nafion, and the largest *ECSA* was given by P20-50.

3.2.2 ORR performances in CP-half-cells

In three-electrode system supplied with air, the potential was scanned between WE and the RE from -50 to 850 mV/ NHE with a scan rate of 5 mV/s, and the current

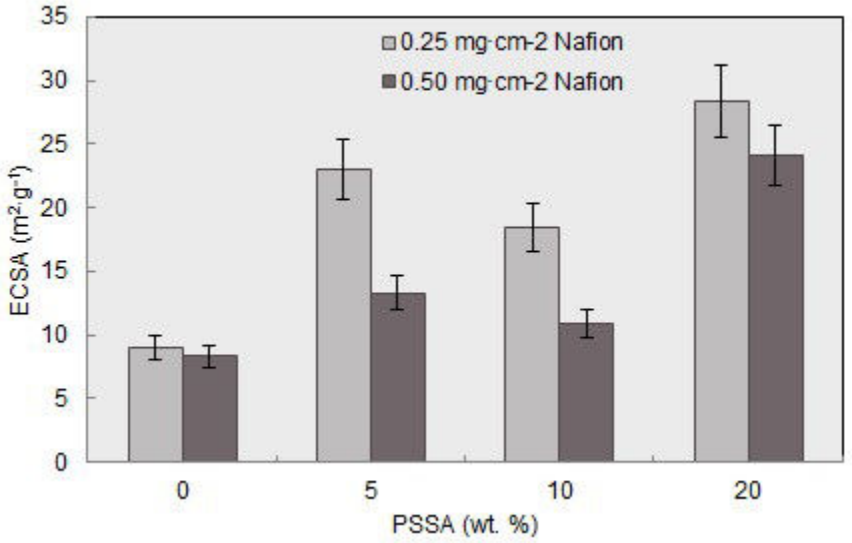

Figure 3.2: *ECSA* of PSSA-Pt/ Vulcan in CP-half cells

between the WE and the CE was recorded. As we previously discussed, the real potential on the working electrode differs from the measured potential. The potential in polarization curves has been corrected by subtracting the ohmic drop, with ohmic resistance R_Ω obtained in EIS measurement.

At 25^{o}C and 1atm, the equilibrium potential of ORR is equal to 1.229V. In 0.5 M H_2SO_4 solution at 25^{o}C, the value is calculated by Nernst equation, approximately varying with the H^+ concentration:

$$E^0 = 1.229V - \frac{RT}{F} ln \frac{1}{a(H^+)} \tag{3.1}$$

The pH of 0.5 M sulfric solution is equal to 0.3 [143], therefore, the value of $a(H^{+)}$ is around 0.50 M. The value of E^0 is 1.211 V.

Overpotential, η, is the difference between the real, corrected potential and the equilibrium potential, E^0.

$$\eta = E_r - E^0 \tag{3.2}$$

The obtained $E_r - i$ and $\eta - logi$ plots were shown in Figure 3.3.

Figure 3.3(a) shows four voltammetry curves, corresponding to the four electrodes with various PSSA functionalized catalysts and 100% Nafion, 0-100, P5-100, P10-100 and P20-100. At 500 mV/ NHE, the reduction current densities were measured at 83, 120, 62 and 53 mA·cm^{-2}, respectively. As the PSSA percentage in catalyst increased

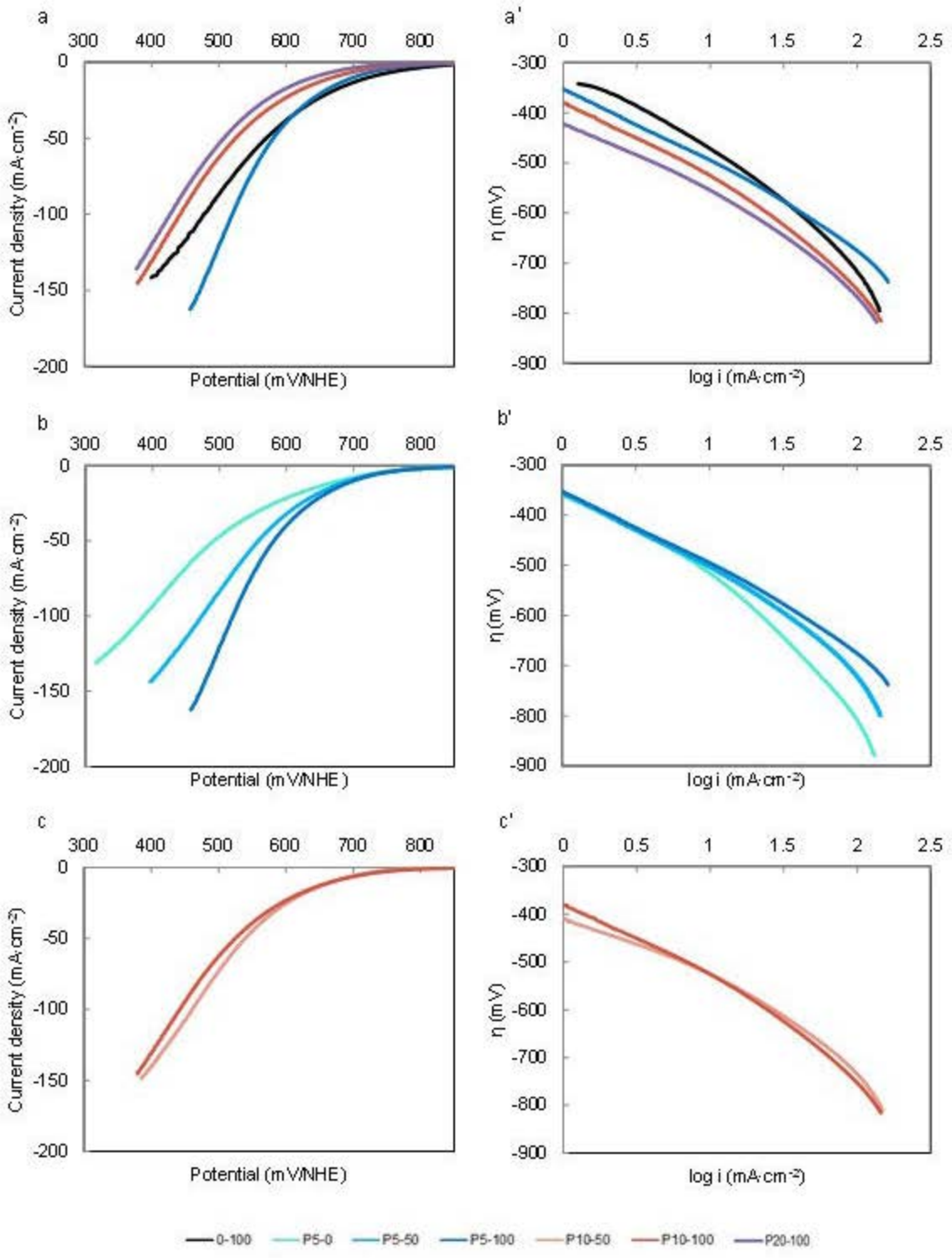

Figure 3.3: LSV curves and η-logi plots of PSSA-Pt/ Vulcan in CP-half cells

from 0 to 5 wt.%, larger ORR current densities were measured. However, as the graft ratio further increased to 10 or 20 wt.%, i decreased.

In there-electrode systems, the working electrode is tested with one side of the membrane facing to water solution. During ORR investigation, H^+ transfers from the acid solution to CL, and water is produced in the electrode. The sulfonation of the catalyst would bring higher ionic property and hydrophilicity to the electrode. Highly hydrophilic catalyst, with 20 wt.% PSSA would hinder the water removing from CL, which is to result in flooding in the electrodes.

The Nafion effect on the ORR properties was studied in half-cell electrodes with 5wt.% PSSA-Pt/ Vulcan catalyst addition. As shown in Figure 3.3(b), reduction current density at 500 mV/ NHE decreased as the Nafion loading reduced, indicating the necessity of Nafion addition in half-cell electrodes. On the other hand, it is shown that P5-50 performed a curve similar to that of "0-100", which may be due to the ionic conductivity of PSSA grafted catalyst. While less Nafion loading was applied in the CL, the PSSA graft on the carbon support transported the proton during the reaction as the function of Nafion ionomer. In P5-0, relatively lower ORR current density was observed.

The Nafion effect was also discussed between P10-100 and P10-50. Different from that found in P5-electrodes, ORR performance was slightly improved when the amount of Nafion added decreased from 0.50 to 0.25 mg·cm^{-2}, indicating that the sulfonation of catalyst with 10 wt.% could reduce the Nafion application in CL. Only half of the Nafion amount in P10-100, was added into P10-50, one quarter of the usual amount 1.0 mg·cm^{-2}and the current density at 500 mV/NHE was 72 mA·cm^{-2}.

According to Tafel equation, at high overpotential region, the overpotential varies linearly with the logarithm of current density. Their η-logi plots have been presented in Figure 3.3(a'), (b') and (c'). The kinetic parameters, b and i_0, characterize the real i. Their values in two current ranges, logi =0-1 and logi=1-2, are given in Table 3.1.

For ORR at 25 °C (298K), α_c about 0.50, two Tafel slopes ($2.303 \cdot \frac{RT}{\alpha F}$) are usually obtained, 60 mV/dec (2-elelctron reduction pathway, n=2) and 120 mV/dec (1-elelctron reduction pathway, n=1) [1]. The value of Tafel slope, relating to n, may indicate different reduction path of oxygen. In the region of *logi* between 0 and 1, the value of Tafel slope in Table 3.1 varies in the range from 160 to 110mV/dec. It may be concluded that ORR occurred with one electron exchanged in the rate controlled process. In Figure 3.3(a'), the four curves are nearly parallel, and their Tafel slopes decrease from 160 to 130 mV/dec as the PSSA ratio in Pt/ Vulcan catalyst increase from 0 to 20 wt.%. Meanwhile, the exchange current density decreased as

Table 3.1: ORR kinetic parameters of PSSA-Pt/ Vulcan in CP-half cells

GDEs	i_0(±15%) (logi=0-1) (10^{-3}mA·cm^{-2})	b(±5) (logi =0-1) (mV/dec)	i_0(±15%) (logi=1-2) (mA·cm^{-2})	b(±5) (logi =1-2) (mV/dec)
0-100	12	160	0.08	220
P5-0	5	155	0.2	281
P5-50	4	150	0.03	200
P5-100	3	142	0.02	180
P10-50	0.2	110	0.03	202
P10-100	2	143	0.05	220
P20-100	0.6	130	0.02	200

the PSSA ratio increased, whose contribution to i-E_r was compensated by the value of b. According to Equation 1.30, the exchange current density of one reaction varies linearly to the true active area at a given air pressure. Although the largest $ECSA$ has been observed in P20-100, the value of i_0 is lower than that of P5-100 or P10-100. In Figure 3.3(b'), it is shown that the three curves overlap each other in the range of logi= 0-1. While their values of i_0 are very close, b slightly decreased with the Nafion amount increased. Figure 3.3(c') presents the $\eta - logi$ plots of P10-100 and P10-50. The values of b and i_0 increase as Nafion amount increased.

In the region of logi between 1 and 2, the Tafel slope of each half-cell is around 1.5 of the value at log i =0-1, from 180-281mV/dec, corresponding to higher i_0 value. The value of b, more or less two times larger than 120mV/dec, may indicate that ORR is partly controlled by diffusion at current density over 10mA·cm^{-2}. In Figure 3.3(a'), while the overpotential of 0-100, P10-100 and P20-100 increase rapidly with logi, P5-100 has a Tafel slope at 180 mV/dec, relatively lower than the value of other three GDEs. In Figure 3.3(b'), the Nafion effect presented in η-logi plots tends to be larger at high currents or high absolute overpotential region. It is shown that the overpotential of P5-0 increase dramatically as the current density increased, with a Tafel slope at 281mV/dec. Finally, comparing the two electrodes with 10 wt.% PSSA grafted catalyst, the one with less Nafion, 0.25 mg·cm^{-2}, has lower i_0 and b constant with that shown in logi =0-1.

EIS method was applied to investigate the ORR performances of the sulfonated catalyst. Impedance tests were carried out by decreasing the steady potential: 550, 450, 350, 250 mV/NHE, and then increasing: 300, 400, 500 , 600 mV/ NHE. The spectra obtained at various potentials are shown in Figure 3.4. So it seems that the profiles of the spectra varies regularly with the potential, irrespective of the variation

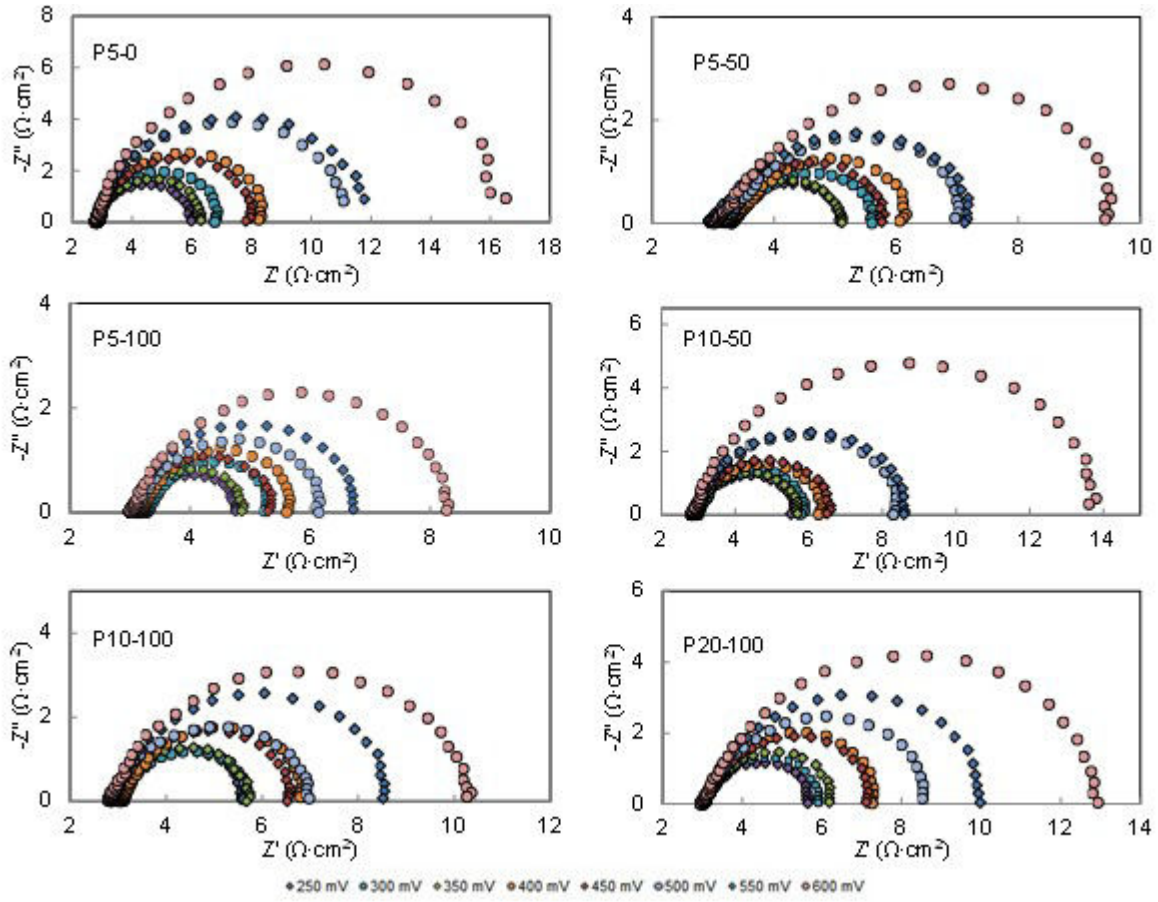

Figure 3.4: EIS plots of PSSA-Pt/ Vulcan in CP-half cells measured at various potential

process (decreasing or increasing), which indicating the stable state of the half-cell.

First, the ohmic drop, $R_\Omega \cdot i$ (due to ohmic resistance), was estimated by EIS. The ohmic resistance, R_Ω, equal to the intercept of the Nyquist plot at high frequency, represents the electric resistance of liquid electrolyte between RE and WE, depending on their distance, and the membrane-CL resistance. A Luggin capillary has been used, whose tip was close to the surface of the working electrode, membrane side, to minimize the influence of the solution. Besides, due to the variety of catalyst and the Nafion ratio in each CL, the attachment between CL and membrane could vary, so the prepared electrodes could establish different membrane resistance. For some tests, it was found that there was a slight change in the value of ohmic resistance during the test, which may be due to the difference in the humidity of membrane. The value of intercept increased as the measured potential decreased from 550 to 250 mV/NHE (overpotential increasing). When the potential increased from 250 to 300 mV/NHE, R_Ω continued to decrease. R_Ω started decreasing while the potential increased from

400 to 600 mV/NHE. The variations of ohmic resistance along the procedure were shown in Figure 3.5(a). The ohmic resistance averaged over the potential was applied in the estimation of ohmic drop.

In the measured potential range of 600- 250 mV, current densities allowed by the electrodes varied in the range of 10-100 mA·cm^{-2} (1$<$ logi$<$ 2). At a given E_m, the reduction current density on each electrode was different due to the various properties of catalysts and interface performance. As a result of the i and R_Ω of each electrode, the real potential varied from 650 to 460 mV/NHE. The $E_r - i$ relationship for each electrode has been shown in Figure 3.5(b). The results presented was mostly consistent with that in LSV.

In the impedance spectra presented in Figure 3.4, the 45° line at high frequency was negligible compared to the diameter of half-circle, so we disregarded the porosity effect in the EIS investigation of PSSA-CP-half cells.

As the measured potential decreased from 550 to 250 mV/NHE, the diameter of the half circles decreased; and then the value increased as the potential back increased from 300 to 600 mV/NHE. For a pure electron-transfer reaction, the diameter of the half-circles, corresponding to charge transfer resistance R_{ct}, decreases as the overpotential increases. However, in the Nyquist plots of MP5-0, the diameter at 350, 450, 550 mV/NHE was lower than that at 300, 400, 500 mV/NHE, respectively. This phenomenon could demonstrate the presence of diffusion resistance, together with R_{ct}, contributing to the half-circle in AC impedance. In three-electrode systems, water accumulated in the membrane not only as the product of ORR but also from the electrolyte. On one side, the membrane was humidified, which could facilitate the proton transfer to CL. On the other side, water in the electrode would hinder the reactant transfer and contribute to the flooding, both resulting diffusion resistance R_d. After the EIS test at 250 mV/NHE, large amounts of water was produced, which reached the carbon paper and hindered the transfer of reactant. Therefore, larger R_d would be present in the following impedance spectra at 300, 400, 500, 600 mV/NHE . However, only one loop was observed in the Nyquist plot, with the charge transfer loop and the diffusion loop overlapping each other, and it was difficult to distinguish the two.

As the diameter of the loop, R_{loop}, was close to the sum of R_{ct} and R_d, the equivalent circuit in Figure 2.9(a) was used in the fitting to estimate the value of R_{loop}. The double layer capacity, C (mF·cm^{-2}), was estimated from CPE. The variation of capacity was shown in Figure 3.5(c). The value is related to the ratio between the effective electrode area and double layer thickness[142]. For GDEs with various Nafion

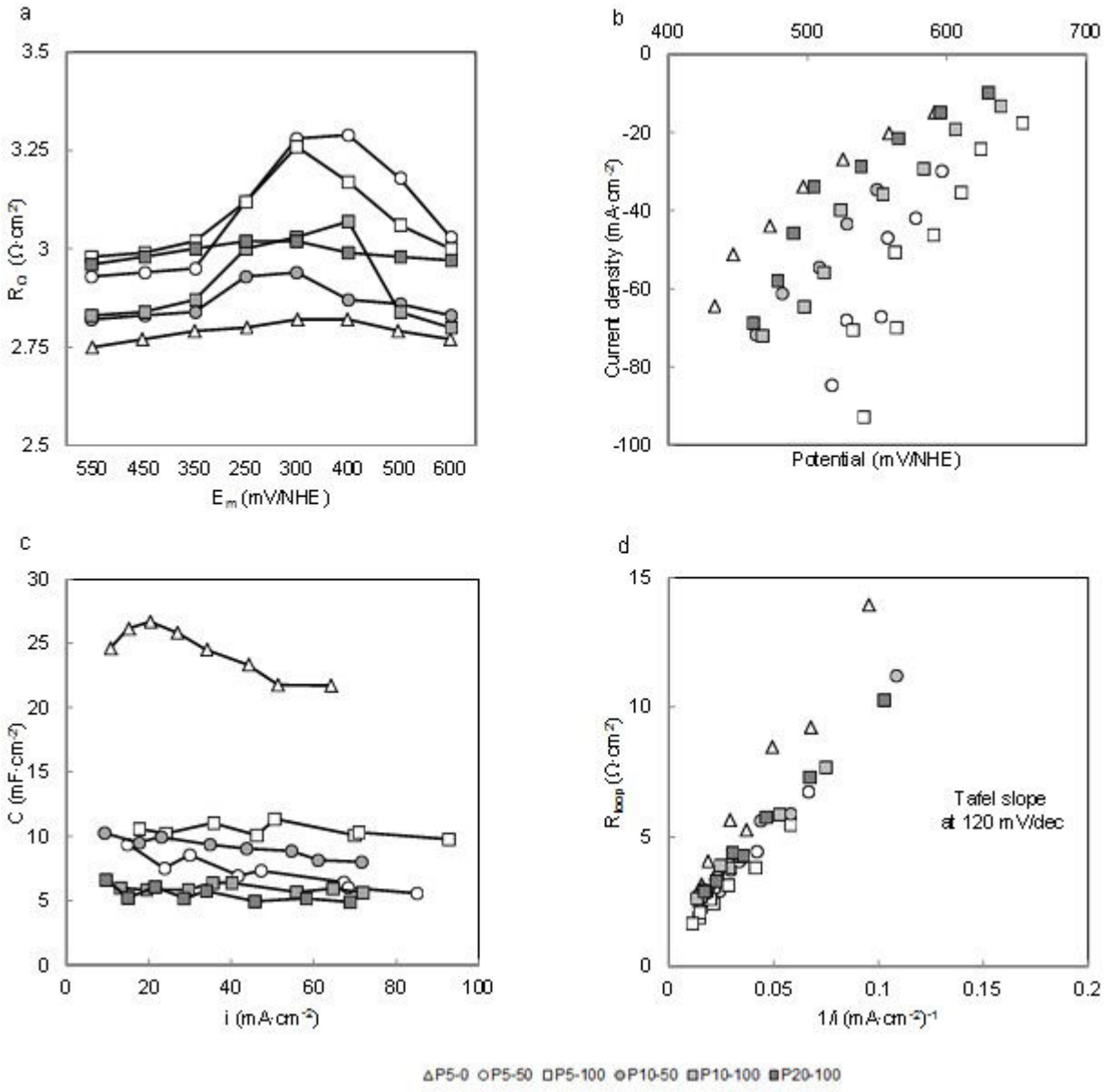

Figure 3.5: EIS parameters of PSSA-Pt/ Vulcan in CP-half cells

amounts and catalysts, the value reflected the catalyst layer morphology. For most electrodes, the value of C was consistent at different reduction current. Moreover, significantly higher value was exhibited by P5-0.

In Figure 3.6(d), the variation of R_{loop} to $1/i$ was shown, with a line of $R_{ct} - 1/i$ as Tafel slope is equal to 120 mV/dec. According to Equation 2.20, the value of R_{ct} varies linearly to $1/i$, with a slope equal to $b/2.303$. In the measured potential range from 250 to 600 mV/NHE, the current density in each GDE varied from 10 to 100 mA·cm^{-2} . Therefore, the value of b at logi =1-2 was used in the estimation of the theoretical value of R_{ct}^0 , whose variation to $1/i$ was shown in Figure 3.6(a) and (b). For further discussion of the contribution of R_{ct}^0 in R_{loop}, the variation of $R_{ct}^0/R_{loop} - i$ was presented in Figure 3.6(c) and (d). The percentage of R_{ct}^0 decreased as the current density increased, due to the increasing contribution of mass transfer resistance at high current. The effect of procedure discussed above appeared to be more significant in the variation of P5-0, with the measured potential (in mV/NHE) labeled in the figure. The value of R_{ct}^0/R_{loop} first increased as potential decreased from 550 to 450, 350 and 250 mV/NHE, subsequently and then increased as the potential increased from 300 to 400, 500 and 600 mV/NHE. It maybe indicate that serious flooding occurred due to no Nafion addition into the GDE.

3.3 PSSA-catalysts in MCP-half-cells

MCP-electrodes were prepared by depositing the catalyst inks, containing sulfonated catalysts and various amounts of Nafion, on G10BC, a carbon paper with a micro-porous layer on its surface , also called micro-GDL (MGDL). They were named of the amount of PSSA and Nafion percentage, starting with "M", for example, "MP5-100" is the one composed of CL with 5% PSSA grafted Pt/Vulcan catalyst and 100% Nafion layered on MGDL. An electrode with non-functionalized catalyst and 100% Nafion coated onto a MGDL disk, named M0-100, was used as the blank sample.

3.3.1 *ECSA* in MCP-half-cells

ECSA of MCP-electrodes, was also estimated based on the hydrogen desorption on platinum particles, by integrating the surface area of hydrogen desorption peak. That value of each MCP-PSSA-half cell, corresponding to PSSA graft ratio (0, 5, 10 and 20 wt.%) and Nafion loading (0.25 and 0.50 mg·cm^{-2}), was depicted in Figure 3.7.

Compared to the value of non-functionalized catalyst, ECSA of PSSA grafted

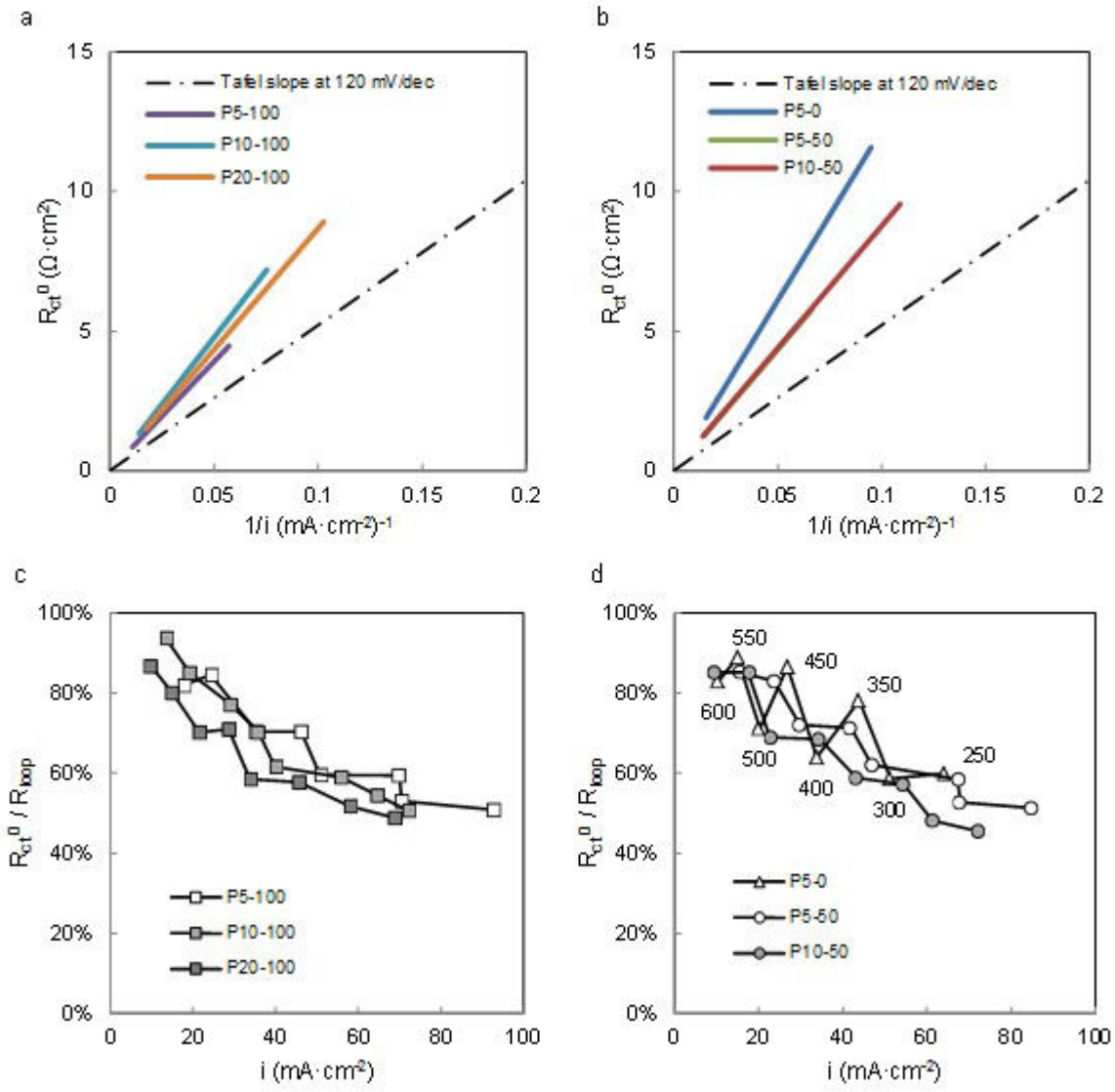

Figure 3.6: The variation of theoretical charge transfer resistance R_{ct}^0 and $R_{ct}^0/R_{loop}$of PSSA-Pt/ Vulcan in CP-half cells

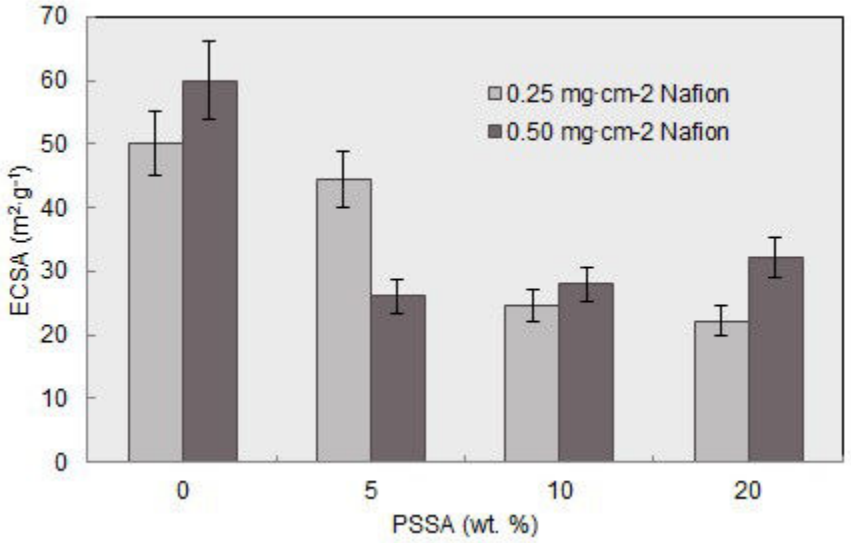

Figure 3.7: *ECSA* s of PSSA-Pt/ Vulcan in MCP-half cells

catalysts was lower. In the series of GDEs with 0.50 mg·cm^{-2}, *ECSA* decreased after the sulfonation, though the value increased slightly as PSSA ratio increased from 5 wt.% to 20 wt.%. Comparatively, *ECSA* was improved due to the sulfonation in CP-electrodes. This phenomenon would be attributed to the presence of the micro-porous layer PTFE impregnated. The PSSA group, behaving hydrophilic, might tend to curl on the surface of MCP, which resulted low hydrogen desorption charge and low *ECSA*.

As Nafion amount decreased in non-functionalized GDEs, the value decreased slightly. As a result of the 5 wt.% PSSA graft, *ECSA* of MP5-50 was higher than that of MP5-100. However, as the PSSA ratio in the catalyst increased up to 10 and 20 wt.%, it decreased a little as the Nafion amount decreased from 0.50 to 0.25 mg·cm^{-2}. It maybe indicated that more PSSA curled in CL with low Nafion addition, reducing *ECSA* .

It was found that most MCP-electrodes had a *ECSA* larger than that of CP-electrodes in Figure 3.2, except MP20-50, whose value was slightly lower than that of P20-50. As we discussed for catalyst layer preparation, as the catalyst ink was deposited to GDL, part of the catalyst likely permeate into the pores of the carbon paper, reducing the activity in fuel cell reaction. When a micro-porous layer is loaded on carbon paper, it protects the catalyst ink from the macro-pores in carbon paper. Therefore, more catalyst is available in hydrogen adsorption/ desorption and higher *ECSA* can be observed in MCP-electrodes.

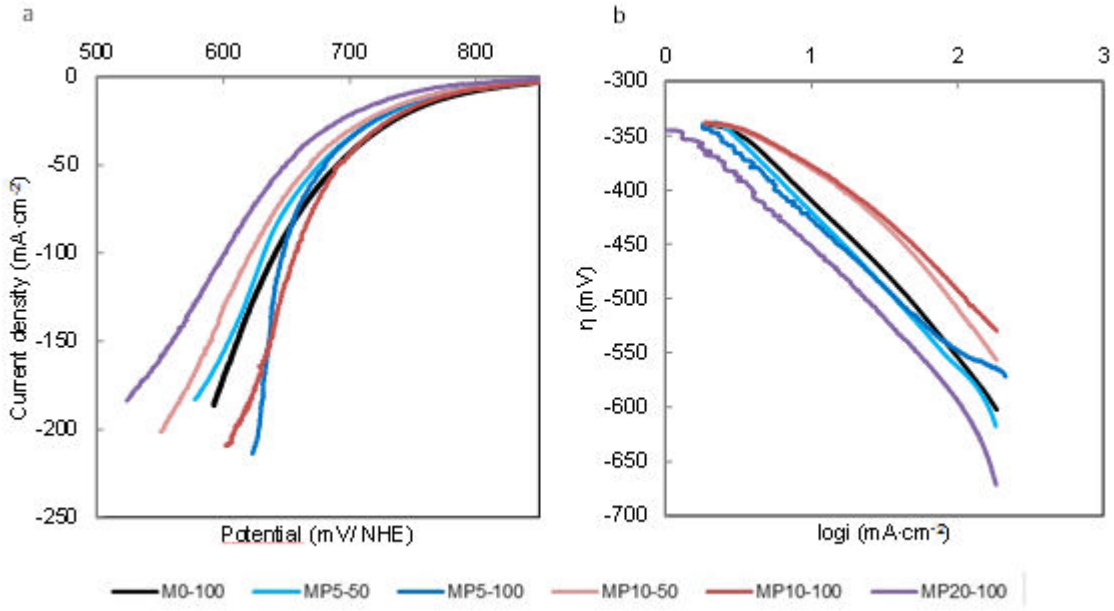

Figure 3.8: LSV curves and η-logi plots of PSSA-Pt/ Vulcan in MCP-half cells

3.3.2 ORR performances in MCP-half-cells

In the polarization curves of MCP-electrodes, as shown in Figure 3.8(a), significant improvements in ORR performances have been observed in MP5-100 and MP10-100, with a current density of 91 and 116 mA·cm^{-2}at 650 mV/NHE, respectively, larger than the value of M0-100. As the PSSA ratio increased to 20 wt.%, ORR current density decreased to 48 mA·cm^{-2} at 650 mV/NHE. It demonstrated that sulfonation of Pt/Vulcan with 5 and 10wt.% PSSA could promote the ORR performances. However, the catalyst with high PSSA grafting ratio in the catalyst, up to 20 wt.%, was highly hydrophilic, which was not beneficial for the water removal from the GDE.

For the discussion of Nafion effect, less Nafion was added into the CL. It was found that less Nafion tended to hinder the ORR. The current densities of MP5-50 and MP10-50 at 650 mV/NHE were around 73 and 66 mA·cm^{-2}.

Compared to the results of CP-GDEs, higher ORR current densities were obtained in MCP-electrodes. It is concluded that the application of MCP as GDL could significantly improve the ORR properties in half-cells tests.

The $\eta - logi$ plots of the MCP-electrodes have been given in Figure 3.8(b), and then the Tafel slope and exchange current density of each electrode could be deduced in Table 3.2. In the current density range of logi= 0-1, while the Tafel slopes of MP10-50 and MP10-100 were around 80 and 70 mV/dec, respectively, the values of

Table 3.2: ORR kinetic parameters of PSSA-Pt/ Vulcan in MCP-half cells

GDEs	i_0(±15%) (logi=0-1) (10^{-3}mA·cm^{-2})	b(±5) (logi =0-1) (mV/dec)	i_0(±15%) (logi=1-2) (mA·cm^{-2})	b(±5) (logi =1-2) (mV/dec)
M0-100	4	120	0.01	140
MP5-50	5	129	0.01	143
MP5-100	3	120	0.005	130
MP10-50	0.1	80	0.02	132
MP10-100	0.04	70	0.01	124
MP20-100	1	115	0.006	140

the other electrodes were higher, around 120 mV/dec. Meanwhile, their values of i_0, were also lower than those of the other GDEs. In the range of logi= 1-2, b varied from 124 to 143 mV/dec, which was only half of those in CP-electrodes. The performance in high overpotential was improved because of the application of MCP.

We measured the EIS plots of MCP-electrodes at 650, 550, 450 and 350 mV/NHE, respectively. The spectra were shown in 3.9, in which the ohmic resistance of each electrode has been subtracted from the impedance spectra. And the average value was applied in the estimation of ohmic drop.

At high frequency, the value of porosity resistance, R_{por}, was estimated, and the value was shown in Figure3.10(e). The magnitude was independent of the current (or overpotential), within 0.01 Ω·cm^2. The highest value was observed by MP5-50, around 0.12 Ω·cm^2.

In the medium and low frequency domains of impedance plots, the kinetic and the diffusion loop overlap each other significantly. In the fitting of the data to the theoretical expression of the impedance established from the equivalent circuit, the distribution of the two loops were not visible. One way is to use circuit (a) (Figure2.9a), in which CPE is in parallel with a loop resistance. Another solution is to calculate the value for the charge transfer resistance, R_{ct}, by analytical derivation of Tafel equation 2.20. The fitting was then carried out by fixing R_{ct} to its theoretical value, which allowed diffusion resistance R_d to be estimated and gave access to the features for the constant phase element Q and n, to be obtained.

In equivalent circuit (a), we estimated R_{loop} and C at various measurement potential, and their variation was shown in Figure 3.10(a) and (b). As depicted in Equation2.20, the slope of $R_{ct} - 1/i$ is equal to $b/2.303$. The Tafel slope estimated from $R_{loop} - 1/i$ in Figure 3.10(a) was higher than 120 mV/dec. Compared to those in CP-GDEs, the values of C in MCP-GDEs were larger, which may be attributed to

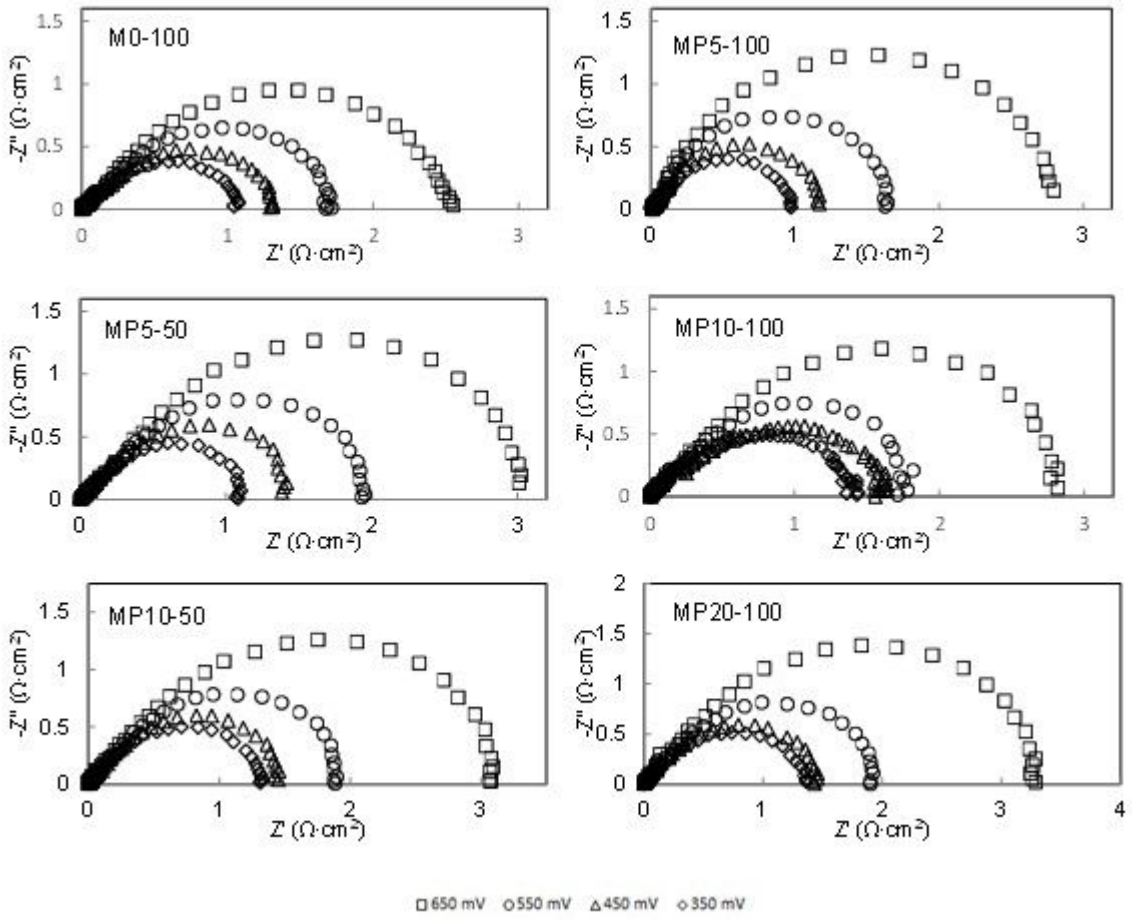

Figure 3.9: EIS plots of PSSA-Pt/ Vulcan in MCP-half cells with the ohmic resistance subtracted

the higher electrochemical surface area of MCP-GDEs. On the other side, C in most GDEs decreased slightly as the current increased, maybe indicating the membrane swelling at high current.

While equivalent circuit (b) was applied with R_{ct} fixed at theoretical value, the variations of C to i were given in Figure 3.10(c). Comparing the value obtained in the two methods, we found that the effect of current density, i.e. the tendency of $C - i$, was consistent in the two figures. In addition, it was shown that the values in Figure 3.10(b) were slightly higher than those in Figure 3.10(c).

R_d, diffusion resistance due to the retardation in the reactant transfer, was estimated in equivalent circuit (b). Its variation with current density were shown in 3.10(d). R_d of MP0-100 increased as the current density increased. As the PSSA ratio in catalyst was equal to 5wt.%, the values in MP5-50 and MP5-100 were nearly independent of reduction current, around $0.30 \pm 0.04\ \Omega{\cdot}\mathrm{cm}^2$. The magnitude in MP10-50 and MP10-100 first decreased as current density increased from 20 to 40 $\mathrm{mA{\cdot}cm^{-2}}$, and then increased as the current density increased, up to around 90 $\mathrm{mA{\cdot}cm^{-2}}$, within the margin of error. As the PSSA ratio increased to 20 wt.%, R_d increased as the current density increased, similar to that of MP0-100. Otherwise, at around 70 $\mathrm{mA{\cdot}cm^{-2}}$, R_d in MP10-100 was higher than that in MP5-100 and MP20-100. Therefore, for reducing the diffusion impedance in ORR, grafting with 5wt.% was recommended.

3.4 PSSA-catalysts in fuel cells

3.4.1 Polarization curves of PSSA-catalysts

Based on the results in half-cells, MCP, with higher performances than CP as the GDL, was selected in the preparation of MEAs. The MEAs, containing various PSSA grafted catalysts and Nafion loading, were studied in a single cell test at room temperature. Each sample was activated by applying CV cycles in the range of 0.1-0.9V, with a scan rate of 5 mV/s, for 50 cycles. And then the polarization properties were measured by chronopotentiometry process.

The obtained polarization curves and corresponding power densities are shown in Figure 3.11. First, among the four electrodes with 0.50 $\mathrm{mg{\cdot}cm^{-2}}$Nafion, potential at 0.4 $\mathrm{A{\cdot}cm^{-2}}$ increased as 5 and 10 wt.% PSSA was grafted onto Pt/Vulcan catalyst. The polarization curves showed that as MEA containing 10 wt.% PSSA in catalysts exhibited relatively higher potential than that of MEA with 5 wt.% PSSA in lower current density range ($<$0.6 $\mathrm{A{\cdot}cm^{-2}}$), its potential decreased rapidly as current increased.

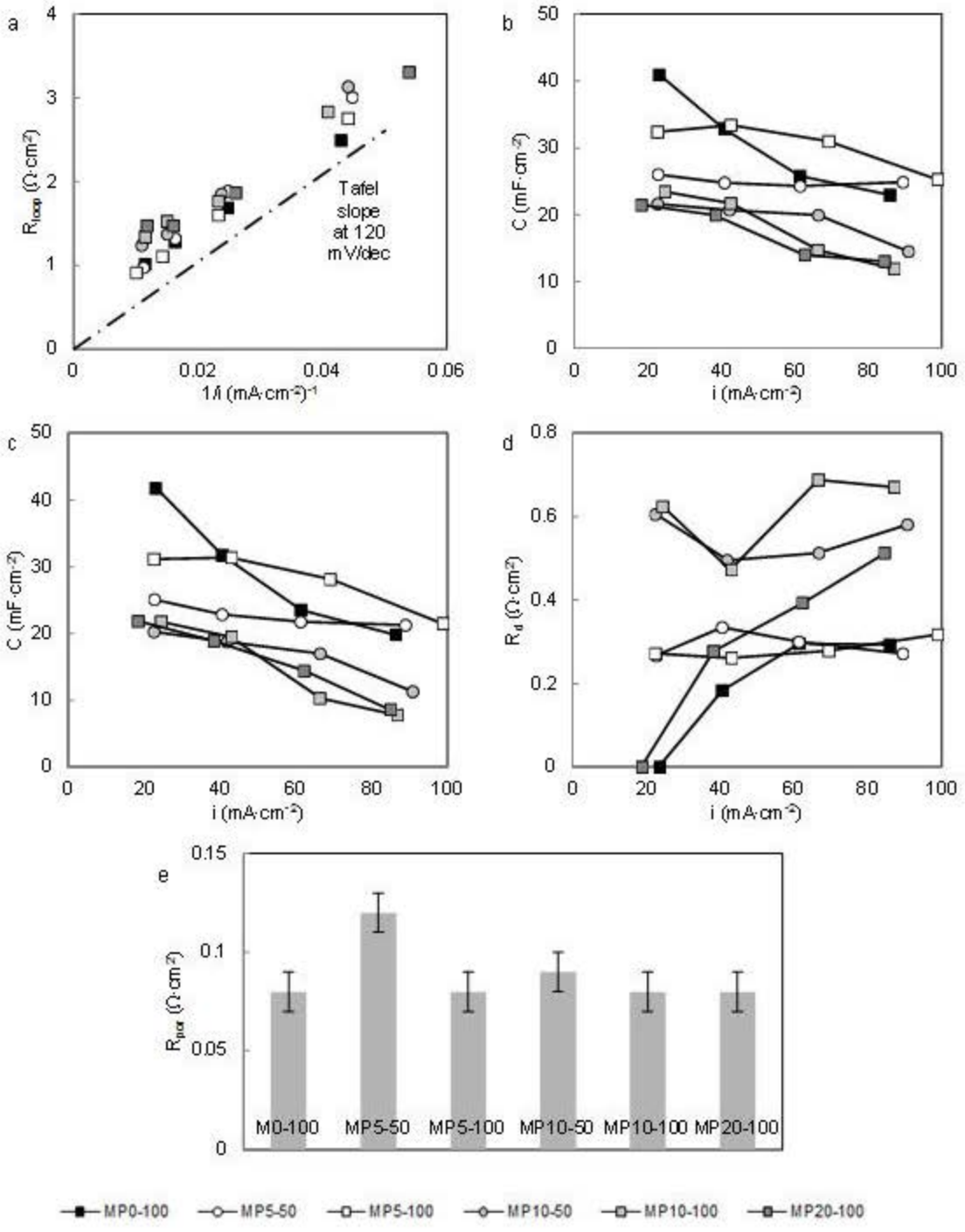

Figure 3.10: EIS parameters of PSSA-Pt/ Vulcan in MCP-half cells

Comparatively, MEA containing 5 wt.% PSSA in catalysts presented slightly higher potential in the high current range. As the PSSA amount in the catalyst increased to 20 wt.%, the fuel cell potential decreased. The presence of PSSA graft might enhance the ionic conductivity and hydrophilicity into the catalyst and the catalyst layer. But 20 wt.% PSSA grafted catalyst, with high hydrophilicity, would not benefit the water transfer in the cathode, and resulted maybe in flooding.

Based on the sulfonated catalyst, less-Nafion MEAs with 0.25 mg·cm^{-2} Nafion and various PSSA graft ratio in the catalysts were prepared, shown in Figure 3.12. As non-functionalized catalyst contributed very low currents in CL with only 0.25 mg·cm^{-2} Nafion, the fuel cell performances were enhanced due to the presence of sulfonated catalysts. A power density, around 201 mW·cm^{-2}, was achieved by the MEA with 10 wt.% PSSA in catalysts.

3.4.2 EIS of PSSA-catalysts

The performances of MEAs with various PSSA grafted catalysts and Nafion loading have also been studied in EIS. The impedance plots tested at 0.05, 0.1, 0.15 and 0.2 A·cm^{-2}, respectively, were shown in Figure 3.13.

For each impedance loop, it was found that the intercept, according to the value of R_m was nearly a constant for each MEA tested at various current, around 0.1 Ω·cm^2. The ohmic resistance was mainly due to the electric resistance of membrane during the fuel cell operation. The consistent value in each single cell presented the similar operation condition, as well as relatively humidification.

In the current density range from 0.05 to 0.2 A·cm^{-2}, the Nyquist plots of PSSA-MEAs presented a half-circle with the following loops overlapping: a charge transfer loop in anode at high frequency, a charge transfer loop in cathode at medium frequency and a diffusion at low frequency. As current increased, the diameter of the half-circle decreased.

The overlapping of the loops resulted the difficulty in distinguishing them from each other. In the fitting, the value of charge transfer resistance at anode $R_{ct,a}$ was fixed at one tenth of that at cathode $R_{ct,c}$ and the exponent of CPE_a , n_a was fixed at 0.8. The estimation of the parameter at cathode was carried out by three steps: the sum of $e(w)$ in high and medium frequency were first minimized and the values of R_m , Q_a , Q_c , n_c, $R_{ct,c}$ were estimated; and then the data in low frequency were minimized to obtain the value of $R_{d,c}$, $\tau_{d,c}$; at last, in overall range, the data was fitted with variable R_m , Q_c , n_c, $R_{ct,c}$, $R_{d,c}$, $\tau_{d,c}$.

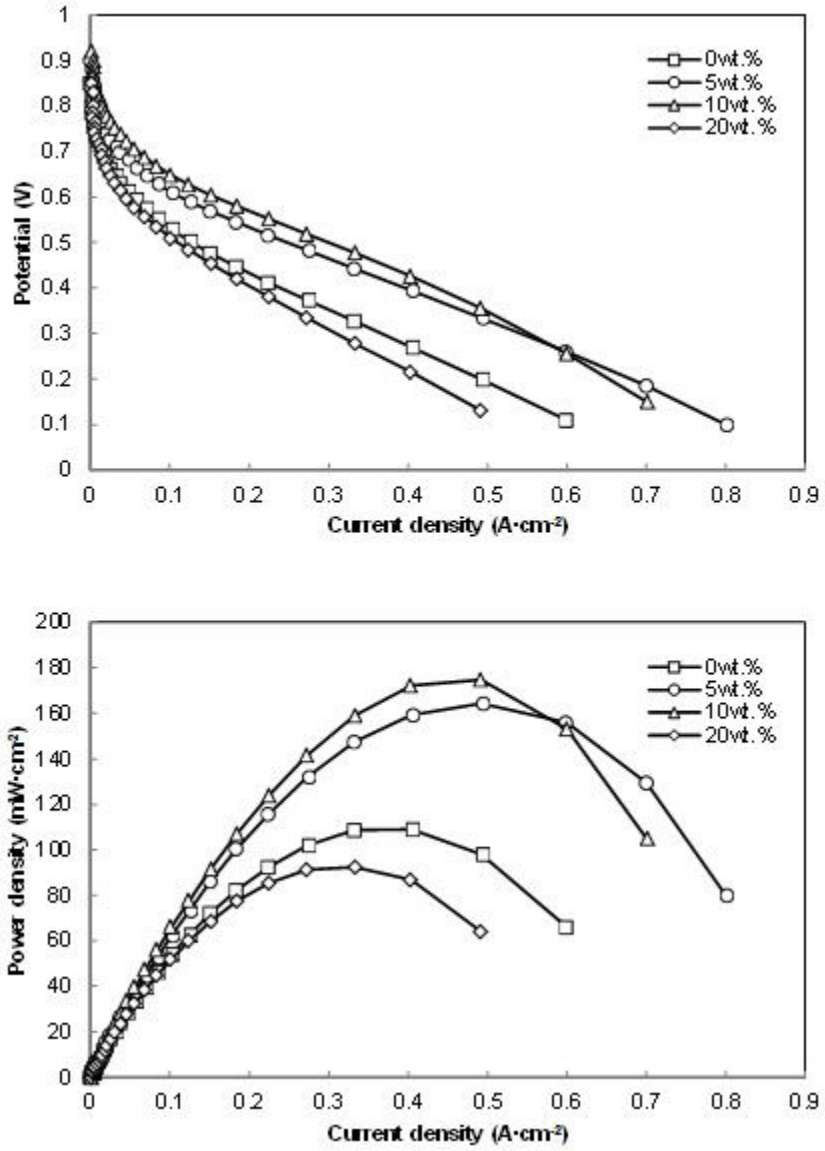

Figure 3.11: Polarization curves and power densities of PSSA-Pt/ Vulcan in MEAs with 0.50 mg·cm^{-2}

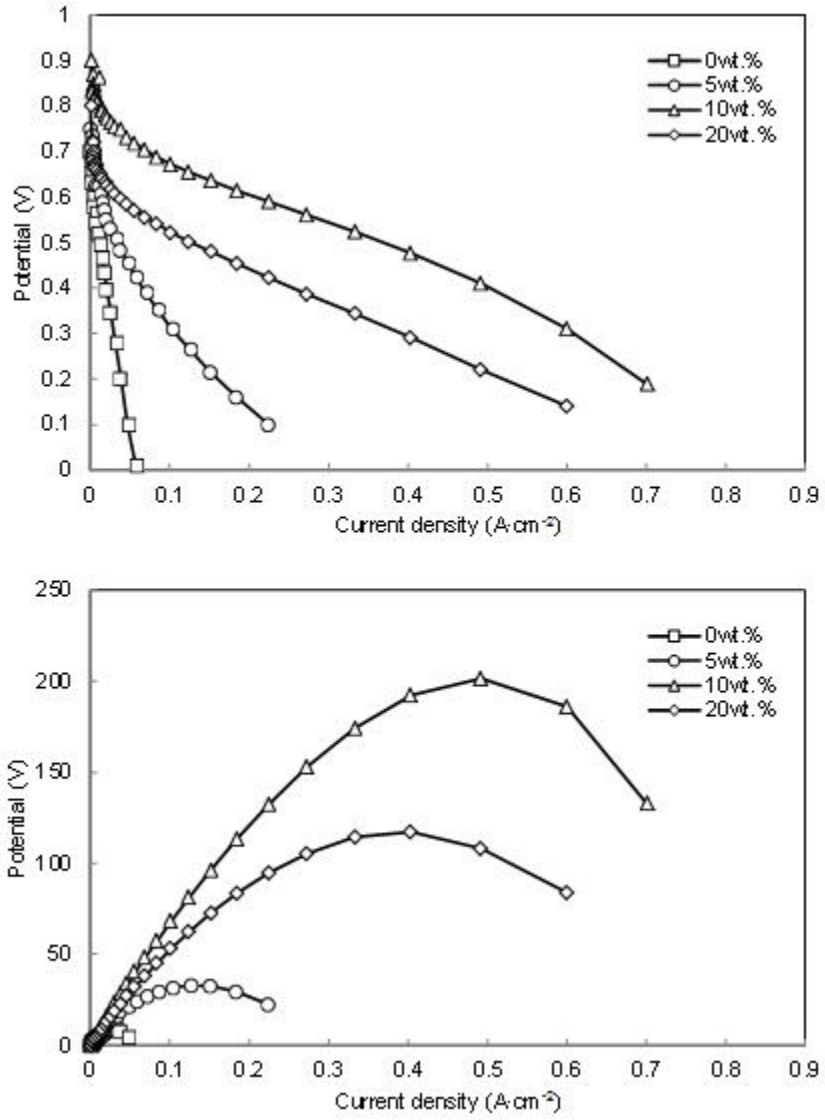

Figure 3.12: Polarization curves and power densities of PSSA-Pt/ Vulcan in MEAs with 0.25 mg·cm^{-2}

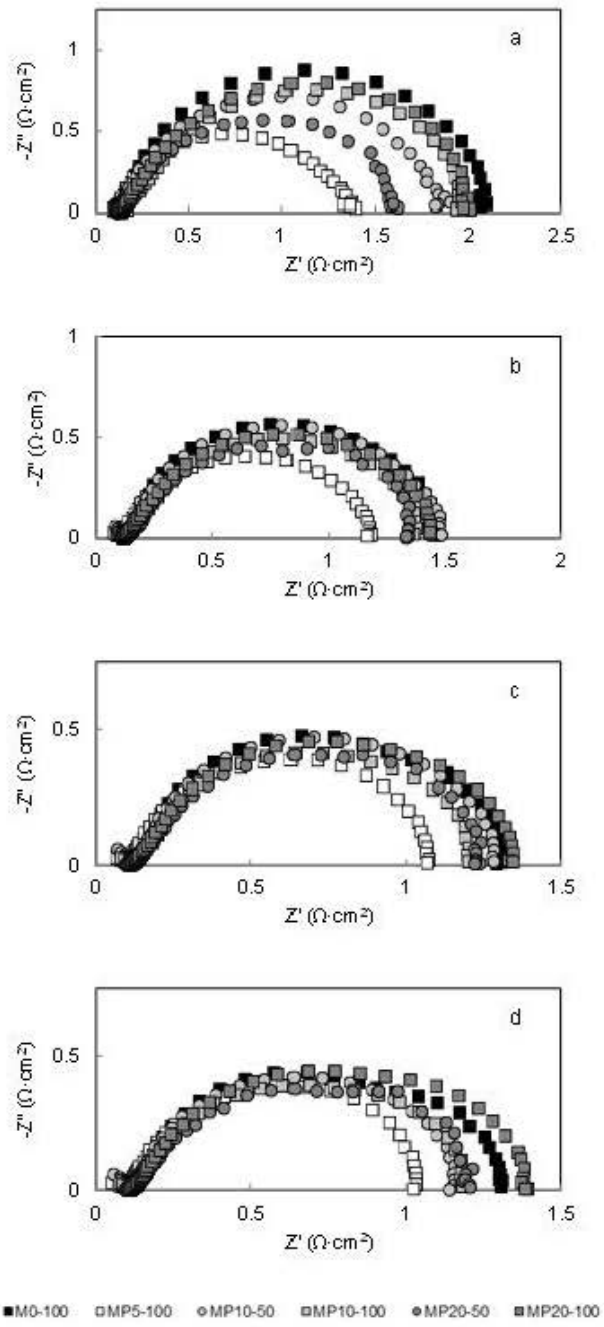

Figure 3.13: EIS plots of PSSA-Pt/ Vulcan in MEAs at (a) 0.05, (b) 0.1, (c) 0.15 and (d) 0.2 mA·cm^{-2}

The value of R_m was relatively constant for each MEA at various current densities, the variation of $R_{ct,c}$, $R_{d,c}$, C_c and $R_{ct,c}/R_{loop}$, with an estimated error in 10%, were presented in Figure3.14.

The variation of $R_{ct,c}$ was shown in Figure3.14(a) with a line of $R_{ct} - 1/i$ as Tafel slope was equal to 120 mV/dec. The Tafel slope of the prepared MEAs in the current range from 0.05 to 0.2 A·cm^{-2} was shown to be higher than 120mV/dec. Relatively lower value of $R_{ct,c}$ were observed in the MEAs with PSSA graft in catalysts.

In Figure 3.14(b), the values of $R_{d,c}$ increased slightly with current density. In the low current range, the main factor in fuel cell reaction was charge transfer control. The percentage of $R_{ct,c}/R_{loop}$ shown in Figure 3.14(d) for most MEAs was higher than 50%.

The variation of C_c to current density was presented in Figure 3.14(c). While the value of M0-100, MP20-100 and MP20-50 decreased as i increased from 0.05 to 0.2 A·cm^{-2}, the value of M5-100, MP10-100 and MP10-50 increased. At 0.2 A·cm^{-2}, the highest value of C_c was observed in MP5-100.

3.5 Conclusions

The prepared PSSA grafted Pt/Vulcan catalysts were studied in XRD and TEM. It was shown that the dispersion of platinum was not influenced by the sulfonation. The diameter of platinum particles remained at around 4nm. The sulfonation process did not result the aggregation of the particles pre-deposited onto Vulcan materials.

Their electrochemical performances were investigated in half-cells and MEAs, respectively. The effect of PSSA graft ratio was discussed, associating with the influence of GDL types and Nafion amount in CL.

In half cell tests, carbon papers (CP) and micro-layered carbon papers (MCP) were applied as the support materials for catalyst ink. The value of $ECSA$ in each electrode was compared and comparatively higher value was observed in MCP based electrodes. In LSV curves, it was shown that the MCP-electrodes exhibited higher current density in ORR. Meanwhile, smaller impedance loops were observed in MCP-half-cells, indicating lower charge transfer resistance during the reaction. The application of MCP was proved to benefit the reaction by increasing the catalytic activity and reducing the charge transfer resistance.

In the two series of half-cells with different GDLs, there is a reasonable concordance in the Nafion effect in CL: less ionomer ratio results in lower current density depicted by LSV and higher charge transfer resistance in EIS.

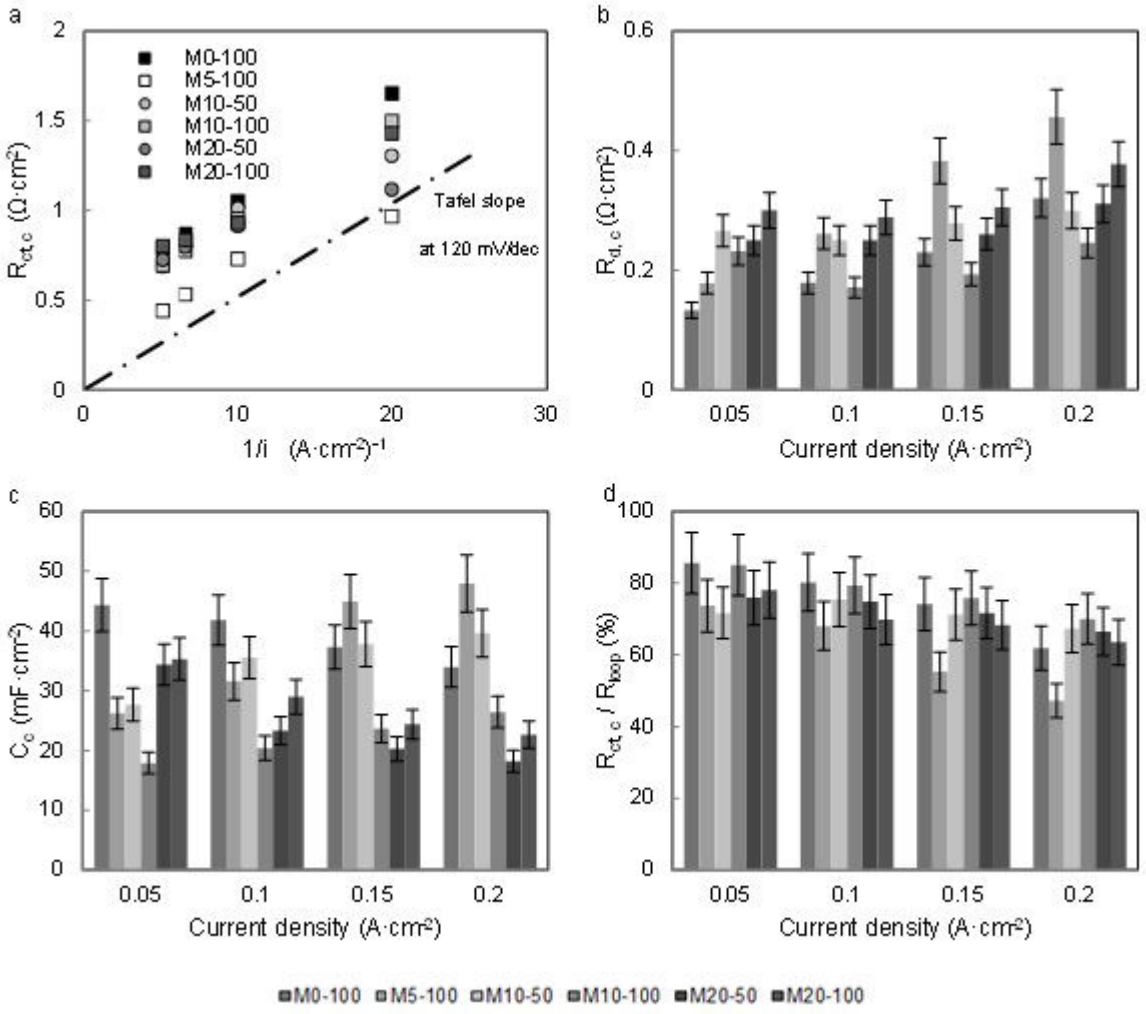

Figure 3.14: The variations of EIS parameters in PSSA-MEAs

As to the influence of PSSA graft ratio, it was found that ORR current increased as the ratio increased from 0 to 5 and 10 wt.%, but decreased at 20 wt.%.

In the investigation of MEAs, improvements in fuel cell performances were achieved after the sulfonation of Pt/ Vulcan catalyst with 5 and 10 wt.% PSSA, which was in agreement with the results in half-cells. In EIS method, it was observed that both charge transfer resistance and diffusion resistance were reduced by the sulfonation of Pt/Vulcan. It concluded that sulfonation of catalyst could improve the fuel cell reaction by promoting the proton transfer in the fuel cell reaction.

The performances of the less-Nafion MEAs, with only 0.25 mg·cm^{-2}Nafion, were obviously improved properties after the sulfonation. And the MEAs with10 and 20 wt.% PSSA grafted onto Pt/Vulcan catalysts performed higher power density than the counterparts with 0.50 mg·cm^{-2}Nafion. The highest power density, 201 mW·cm^{-2} was achieved in the MEAs with 10 wt.% PSSA in catalyst and 0.25 mg·cm^{-2}Nafion in CL.

Chapter 4

PSA grafted Pt/Vulcan catalysts

The Pt/Vulcan catalysts were grafted by diazonium ion reduction with 5.8, 11.6 18.0 and 23.3 wt.% PSA groups per gram of catalyst (around 0.32, 0.64, 0.98 and 1.3 mmol per gram of catalyst) 4-aminobenzene sulfonic acid. They were named as D1, D2, D3 and D4, respectively. XRD and TEM were applied to characterize the platinum distribution before and after the functionalisation. The electrochemical properties of the catalysts were then studied in half-cell mode and in fuel cell.

In half-cell disk, the catalysts with 11.6 or 23.3 wt.% PSA groups were added in the catalyst layer, containing 0.25 or 0.50 mg·cm^{-2} Nafion. Two types of GDL, CP or MCP, were used as the GDL, respectively, to prepare the half-cell disks. The effects of graft ratio, Nafion amount in CL, GDL types on the performances in three-electrode system were presented in section 4.2. Their catalytic activities were estimated by CV in nitrogen. And the ORR properties were studied by LSV and EIS in air feeding. From the polarization curve of each GDE obtained by LSV, the value of Tafel slope and exchange current density were estimated in two current ranges: below and above 10 mA·cm^{-2}, which gave further explanation of the ORR process. EIS measurement presented the impedance of each GDE at various measured potential, which was then fitted to estimate each parameters during the ORR.

MEAs with various catalysts (with 5.8, 11.6 18.0 and 23.3 wt.% PSA groups) and Nafion amounts (0.25 or 0.50 mg·cm^{-2}) were prepared, and investigated in a single cell test at ambient temperature (25^{o}C), under 100% humidification. Their polarization curves and Nyquist plots at various current were presented in section 4.3. Based on the results, we got some conclusions in the optimum amount of PSA graft ratio and Nafion addition in the CL.

4.1 Physical characterization

The prepared PSA grafted Pt/Vulcan catalyst has also been investigated by XRD and TEM. The diameter of platinum particles in each catalyst was found to be around 4nm. As that depicted in PSSA grafted catalysts, no obvious aggregation of platinum particles was observed during the diazonium reaction.

4.2 PSA-catalysts in half-cells

Half-cell electrodes were prepared by coating the inks containing various catalysts and Nafion addition onto the GDL. A Nafion membrane was then hot-pressed onto the CL side at 135^{o}C, 40 bar for 6min. The prepared half-cell disks were named with the percentage of the Nafion addition in the CL. For example, "D2-100" was the sample prepared with 11.6 wt.% PSA grafted Pt/Vulcan catalyst and 100% Nafion addition (0.50 mg·cm^{-2}). The half-cell electrodes prepared were studied in a three-electrode system: 4 disks on carbon paper, D2-50, D2-100, D4-50 and D4-100; and 2 disks on MCP, MD2-100 and MD4-100. For the disks prepared with MCP, those with low Nafion amount were not tested. The membrane hot-pressed onto the surface of CL were found to absorb water and swell after immersed into the liquid solution. The CL containing grafted catalysts had low cohesion on the hydrophobic micro-porous layer on MCP. More than 3 samples containing the same components, including the catalysts, the Nafion addition and GDL types were prepared to obtain repeatable data.

4.2.1 *ECSA* of PSA-catalysts

The catalyst layer, containing Pt/Vulcan catalysts grafted with 11.6 or 23.3 wt.% PSA and 0.50 mg·cm^{-2} Nafion, was coated onto a GDL, CP or MCP. Their electrochemical activities were studied by CV. While no obvious bubble was observed on the surface of half-cell disks D2-50 and D4-50 after its immersion into the solution, the membrane bugled out during the CV cycles, resulting low repeatability of the data. Therefore, only the results of the samples with 0.50 mg·cm^{-2} Nafion in CL were presented in the figure.

The variation of *ECSA* with GDL types and PSA ratio was presented in Figure 4.1. It was shown that higher values were observed in MCP-electrodes.When carbon paper materials were used as the GDL, the catalyst ink was coated on its surface. A part of catalysts would permeate into the macro-pore and lost the catalytic activities.

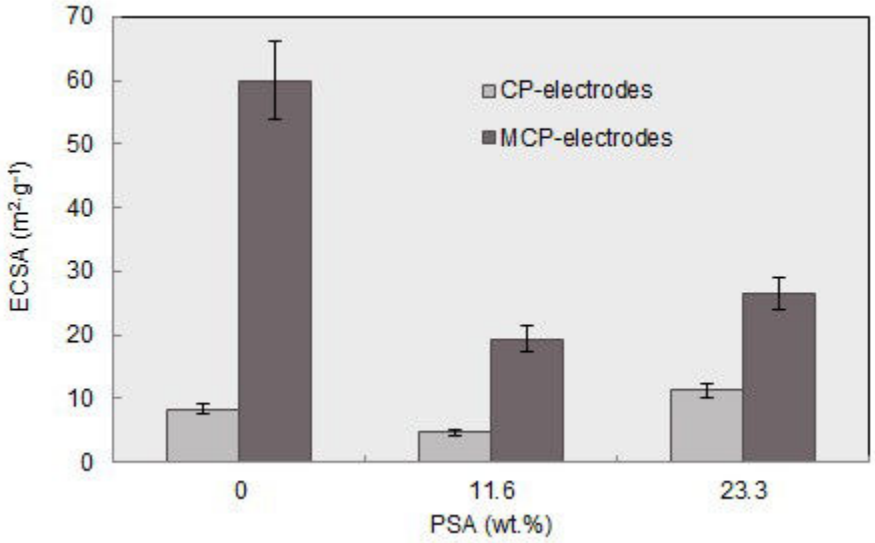

Figure 4.1: *ECSA* PSA-Pt/ Vulcan in half cells with 0.50 mg·cm^{-2}Nafion

Otherwise, the micro-porous layer coated on the carbon paper material would protect the catalyst from falling into the pores of carbon paper. Therefore, more platinum sites were offered for hydrogen adsorption/desorption.

In CP-electrodes and MCP-electrodes, the value of *ECSA* decreased as the PSA graft ratio increased from 0 to 11.6 wt.%. It may be attributed to the hydrophilicity of the grafted catalyst, which have low cohesion with the hydrophobic GDL, reducing the accessibility of platinum particles and the active surface area. The value increased slightly as the ratio increased from 11.6 to 23.3 wt.%. On one side, high amount of PSA groups bring high hydrophilicity of the catalyst, on the other side, the PSA graft could improve the catalytic activity.

4.2.2 ORR performances of PSA-catalysts

In the potential range from -50 mV and 850mV/ NHE, LSV was applied with a scan of 5 mV/s. For each half-cell disk, the scan was carried out for 5 times. And the data, measured potential and current density, in the 5th scan were recorded. The real potential were estimated after subtracting the ohmic drop from the measured potentials and given in the LSV curves following.

First, PSA grafted catalysts, combined with 0.25 and 0.50 mg·cm^{-2} Nafion was studied in CP supported half-cell electrodes. As depicted in Figure 4.2, the real potential of D2-100 and D4-100 at 100 mA·cm^{-2} were around 404 mV/NHE lower than the value of 0-100, non-functionalized Pt/Vulcan catalyst, at 478 mV/NHE.

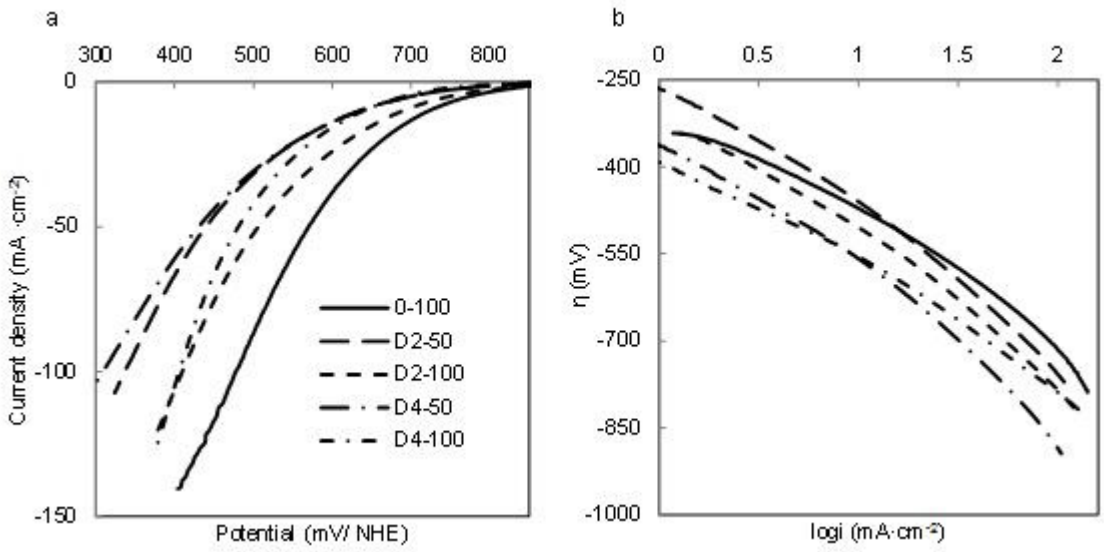

Figure 4.2: LSV curves (a) and $\eta - logi$ plots (b) of PSA-Pt/ Vulcan in CP-half cells

Lower potential, higher overpotential, was required for producing 100 mA·cm^{-2} in the ORR in the presence of PSA groups on the Pt/Vulcan catalyst, indicating that the PSA grafting in catalyst did not facilitate the reduction. As the amount of Nafion decreased to 0.25 mg·cm^{-2}, the potential of D2-50 and D4-50 decreased.

At 25ºC, 1atm, the equilibrium potential E^0 of ORR in 0.5 M H_2SO_4 solution is equal to 1.211V. Therefore, the overpotential, η, the difference between the real and E^0, was estimated. The $\eta - logi$ plots were shown in Figure 4.2 (b), and they were studied in two current density ranges: $logi = 0 - 1$ and $logi = 1 - 2$. The obtained ORR kinetic parameters were given in Table 4.1. In the low current (overpotential) range, the values of b of four GDEs with PSA-grafted catalysts supported on CP-GDL in ORR were between 180 and 208 mV/dec. The value of D4-100, 180 mV/dec, slightly higher than 120mV/dec, corresponding to the 1-elelctron reduction pathway in the rds of ORR (n=1) at 25 °C (298K), with the value of charge transfer coefficient α at around 0.50 [1]. The higher value might be attributed to the mass transfer control in spite of the low current density or to relatively lower α in the ORR. The value of b decreased as the amount of PSA ratio increased , as well as the exchange current density. Meanwhile, both of b and i_0 increased as the Nafion amount decreased from 0.50 to 0.25 mg·cm^{-2}. In high current/ overpotential range, the influence of Nafion addition and PSA graft ratio was observed to be consistent of that in $logi = 0 - 1$. At current over 10 mA·cm^{-2}, mass transfer would play more significant role in the ORR process, resulting higher Tafel slope.

Table 4.1: ORR kinetic parameters of PSA-Pt/ Vulcan in half-cells

GDEs	$i_0(\pm 15\%)$ (logi=0-1) (10^{-3}mA·cm^{-2})	$b(\pm 5)$ (logi =0-1) (mV/dec)	$i_0(\pm 15\%)$ (logi=1-2) (mA·cm^{-2})	$b(\pm 5)$ (logi =1-2) (mV/dec)
0-100	12	160	0.08	220
D2-50	0.06	208	0.2	280
D2-100	0.03	200	0.1	260
D4-50	0.02	200	0.1	285
D4-100	0.008	180	0.06	245
M0-100	4	120	0.01	140
MD2-100	0.01	142	0.09	200
MD4-100	0.007	130	0.007	128

PSA-grafted catalysts had also been studied in MCP based half-cell electrodes by LSV. The two prepared electrodes, MD2-100 and MD4-100, with 0.50 mg·cm^{-2}Nafion in CL, was investigated. Their polarization curves and Tafel plots were shown in Figure 4.3. The real potential at 100 mA·cm^{-2}increased from 580 to 662 mV/NHE as the PSA ratio increased, while the value for M0-100 was around 651 mV/NHE. As MCP was applied, ORR occurred at relatively higher potential (low overpotential). It maybe indicated that higher amount of platinum particles were accessible for the reaction in MCP-electrodes. MD4-100 performed better than M0-100, which demonstrated the feasibility of PSA grafting onto Pt/Vulcan catalysts.

The exchange current density and Tafel slope obtained in the $\eta - logi$ plots shown in Figure 4.3(b) had been presented in Table 4.1. Compared to D2-100 and D4-100, the MCP based electrodes had lower slope in the overall current range , indicating that higher current could be obtained at relatively lower overpotential. The value of b in MD4-100 was almost consistent, around 120 mV/dec, following well the one-electron reduction pathway in the rds of ORR (n=1) at 25 °C , with the electron transfer coefficient around 0.50. It may be concluded that the mass transfer control during the ORR appeared to be less significant in MD4-100. On the other sides, the exchange current density decreased slightly, whose effect on the current density was compromised by the lower Tafel slope.

EIS has also been applied in the investigation of the ORR performance of the four PSA-Pt/Vulcan electrodes D2-100, D4-100, MD2-100 and MD4-100. The impedance plots measured at 550, 450, 350, 400, 500, 600 mV, in sequence, have also been shown in Figure 4.4. While LSV is rapid scan method to estimated the ORR properties, an impedance measurement from 10KHz to 50 mHz, with 60 points, takes around 4

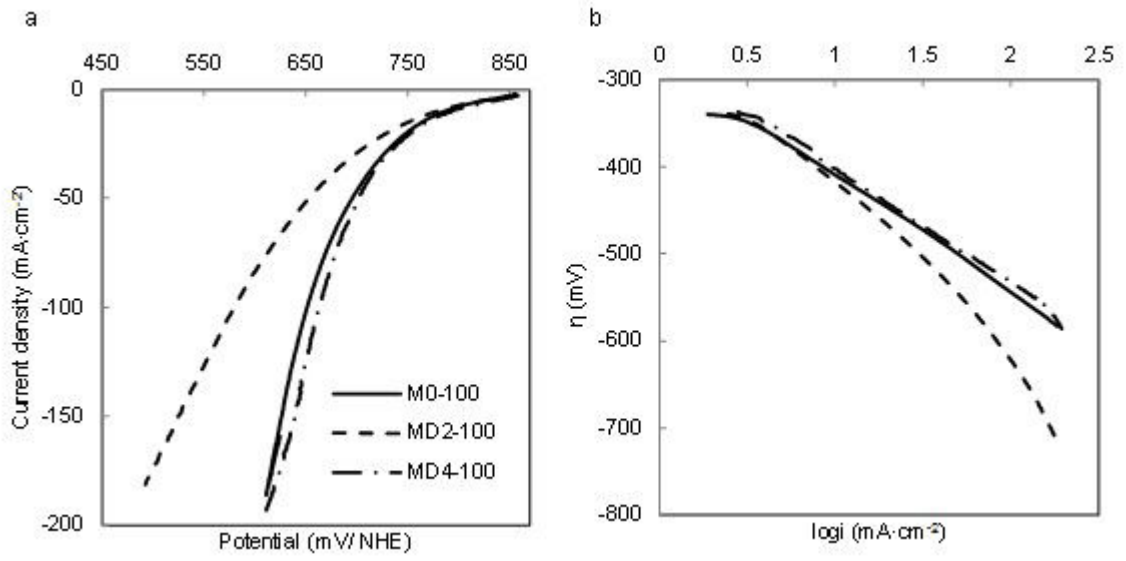

Figure 4.3: LSV curves (a) and η-logi plots (b) of MCP-electrodes with PSA grafted catalysts in air

min. Small bubbles were found on the membrane side of the prepared half-cell disks with low Nafion addition. Therefore, the effect of Nafion were not successfully tested in the three-electrode systems.

As we have presented above, an impedance plot starts from a point of intersection at the real axis Z', whose value equals to the ohmic resistance, R_Ω. It consists the electric resistance of liquid electrolyte between the RE and the WE, depending on their distance, and the membrane-CL resistance. The different components in each electrode, including various catalysts and Nafion ratio in the CL, as well as the GDL type, resulted the membrane resistance. The ohmic resistance estimated differed in the prepared electrodes. Meanwhile, it was found that the value varies within 0.5 $\Omega{\cdot}cm^2$ in the same sample at different measured potentials, while may be due to the accumulation of water at higher overpotential. The value of intercept increased as the measured potential decreased from 550 to 250 mV/NHE (overpotential increasing).

In figure 4.4, the intercept at high frequency has been subtracted from each Nyquist plot and the loops started from the origin. The value of R_Ω of each electrode was obtained from the average value at various potential, based on which, E_r in LSV was estimated. In EIS measurement, the value of E_r was obtained according to $R_\Omega \cdot i$ at each measurement potential. The relationship of $E_r - i$ for each electrode has been shown in Figure 4.5(a). It was shown that at around 40 $mA{\cdot}cm^{-2}$, the potential of MD4-100 was higher than the values of the other three. In partially, the MD grade was depicted to be far more efficient than regular D grade, as observed by LSV exper-

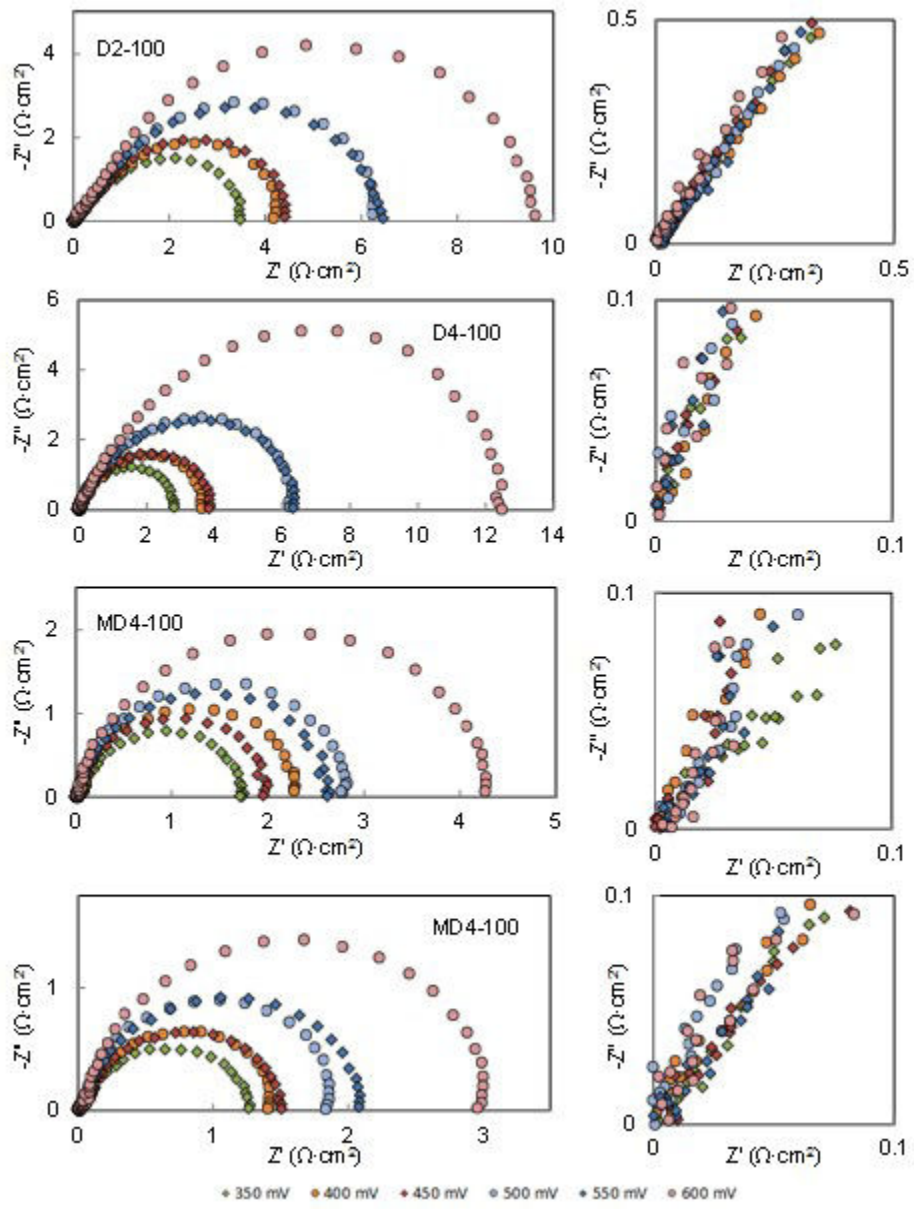

Figure 4.4: EIS of PSA-Pt/Vulcan in half-cells measured at various potential with ohmic resistance subtracted

iments. The data shown in Figure 4.5(a) was different from those in Figure 4.2 and Figure 4.3(b). Compared to LSV process, the EIS measurement partially corresponds to steady state.

The circuit shown in Figure 2.9 (a) was used as the model to fit the experimental data. The equivalent circuit was composed of the interception resistance R_{in} , the overall loop resistance R_{loop} , a CPE (Q, n) replacing the double layer resistance. For considering the porosity effect in high current density. Reliable fitting was obtained by minimizing the sum of $e(w)$ (the variance between the experimental data and those in mode) in the frequency range. However, porosity factor was not considered in the equivalent circuit which appearing as a 45^{0} line at high frequency from 3KHz to 30Hz. Therefore, for the estimation of porosity resistanceR_{por}, the sum of $e(w)$ was considered from 30Hz to 50mHz, and obtain an interception resistance R_{in}. The value of R_{por} was estimated from the difference between R_{in}. and R_{Ω}. Its variation to ORR current density have been shown in Figure 4.5(b). It was observed that the value was independent to current, which agreed with the theory of Hitz et al [136]. Among the four electrodes, the highest R_{por} was found in D2-100, $0.38 \pm 0.01\Omega{\cdot}\mathrm{cm}^2$, while the value was $0.12 \pm 0.01\Omega{\cdot}\mathrm{cm}^2$, $0.06 \pm 0.01\Omega{\cdot}\mathrm{cm}^2$, and $0.07 \pm 0.01\Omega{\cdot}\mathrm{cm}^2$, for D4-100, MD2-100 and MD4-100, respectively. The higher value of D2-100 and D4-100 indicated the higher porosity in CP-GDEs. As MCP was applied, lower porosity resistance was detected.

The value of the double-layer capacity, C, based on CPE, was estimated. The value of n ranged from 0.9 to 1, indicating an interface close to that of an ideal capacitor. As shown in 4.5(c), the values of each electrode changed within an error range, and those of D4-100 were comparatively lower. Comparatively, the values of D2-100, was close to those of MCP-GDEs, higher than D4-100. The magnitude of capacity maybe presented the different characterizations in the double-layer of various CL-membrane interface..

The variation of R_{loop} was shown in Figure 4.5(d). According to Tafel's law, at high overpotential, R_{ct} is in linear with 1/i, with a slope equal to 1/2.303 of Tafel slope. Here, the slope of $R_{loop} - 1/i$ was higher than that of 1/2.303 of Tafel slope, which was obtained in LSV. The highest slope was observed in D2-100, whose Tafel slope was also higher than the values of the other three GDEs. And the lowest magnitude was observed in electrode MD4-100.

The theoretical value of R_{ct}^{0} was estimated based on the Tafel slope in $logi = 1-2$ obtained in LSV, and its variation to 1/i in the current range was shown in Figure 4.5(e). The contribution of diffusion phenomenon during ORR was evaluated in

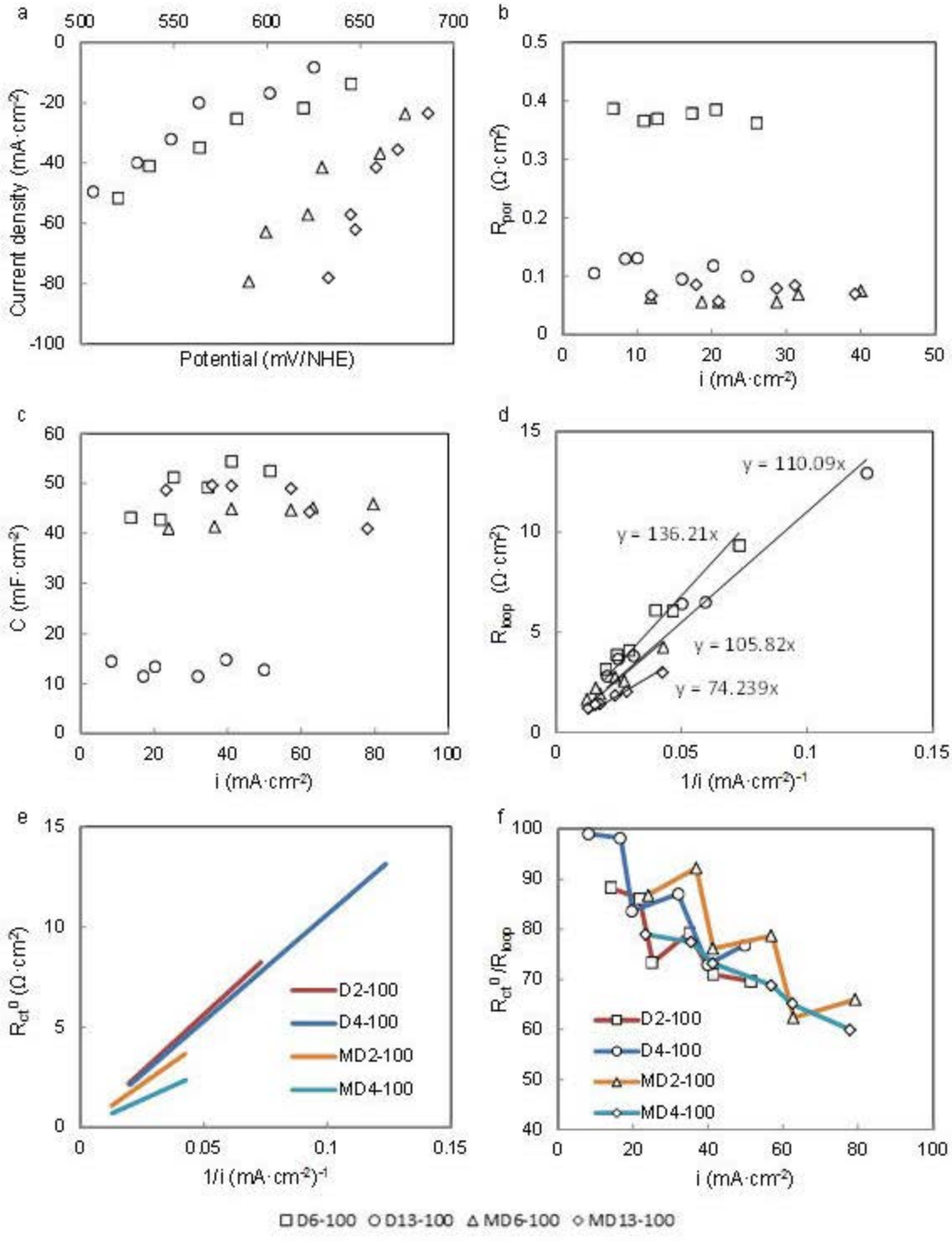

Figure 4.5: EIS parameters with ORR current of PSA-Pt/ Vulcan in half cells

$R_{ct}/R_{loop} - i$, presented in Figure 4.5(f). As the current density increased, the percentage of R_{ct} decreased. As discussed in chapter 3, the measurement procedure resulted in the zigzag lines along current density, where water accumulated in one measurement increased the reactant retard in next measurement. It demonstrated that the contribution of diffusion in the Nyquist loop increased with the current density, as expected.

4.3 PSA-catalysts in fuel cells

4.3.1 Polarization curves of PSA-catalysts

As MCP was used as the GDL, MEAs prepared with various PSA grafted catalyst and Nafion loading have been studied in single cell tests. The prepared MEAs were activated in the 50 CV cycles between 0.1 and 0.9V, and then the polarization properties were measured. The polarization curves and the power densities were shown in Figure 4.6 and 4.7, with 0.50 and 0.25 mg·cm^{-2} Nafion in the CL, respectively. Obvious improvements in the cell performances were observed after the PSA graft with 5.8, 11.6, 18.0 and 23.3 wt.% on Pt/Vulcan catalysts. The fuel cell potential at 0.4 A·cm^{-2} increased as the graft ratio increased from 0 to 5.8 wt.%. As the ratio attained at 11.6, 18.0 and 23.3 wt.%, the polarization curves were very close. The power density of MEA with 18.0 wt.% PSA in the CL was slightly higher than the others, around 223 mW·cm^{-2} .

The Nafion effect has also been discussed in MEAs with 18.0 and 23.3 wt.% PSA grafted Pt/ Vulcan catalysts . Two less-Nafion MEAs with 0.25 mg·cm^{-2} Nafion added into the cathodes, were tested. In Figure 4.7, it was shown that the potential decreased rapidly to current in the less Nafion MEAs. As the ratio of PSA increased from 18.0 and 23.3 wt.% PSA, the potential increased slightly, especially in the low current range.

4.3.2 EIS of PSA-catalysts

The performances of MEAs with PSA grafted catalysts and various Nafion loading were studied in EIS. Their Nyquist plots tested at 0.1, 0.2 A·cm^{-2}, respectively, were shown in Figure 4.8. It was shown that in the four MEAs with 0.5 mg·cm^{-2} Nafion in CL, the diameter of the impedance loops were close. The overall resistance, corresponding to the diameter of the loop, was around 0.8 Ω·cm^{2}at 0.1 A·cm^{-2}, 0.5 Ω·cm^{2}at 0.2 A·cm^{-2}. As the Nafion amount in CL was reduced to 0.25 mg·cm^{-2}, larger loops

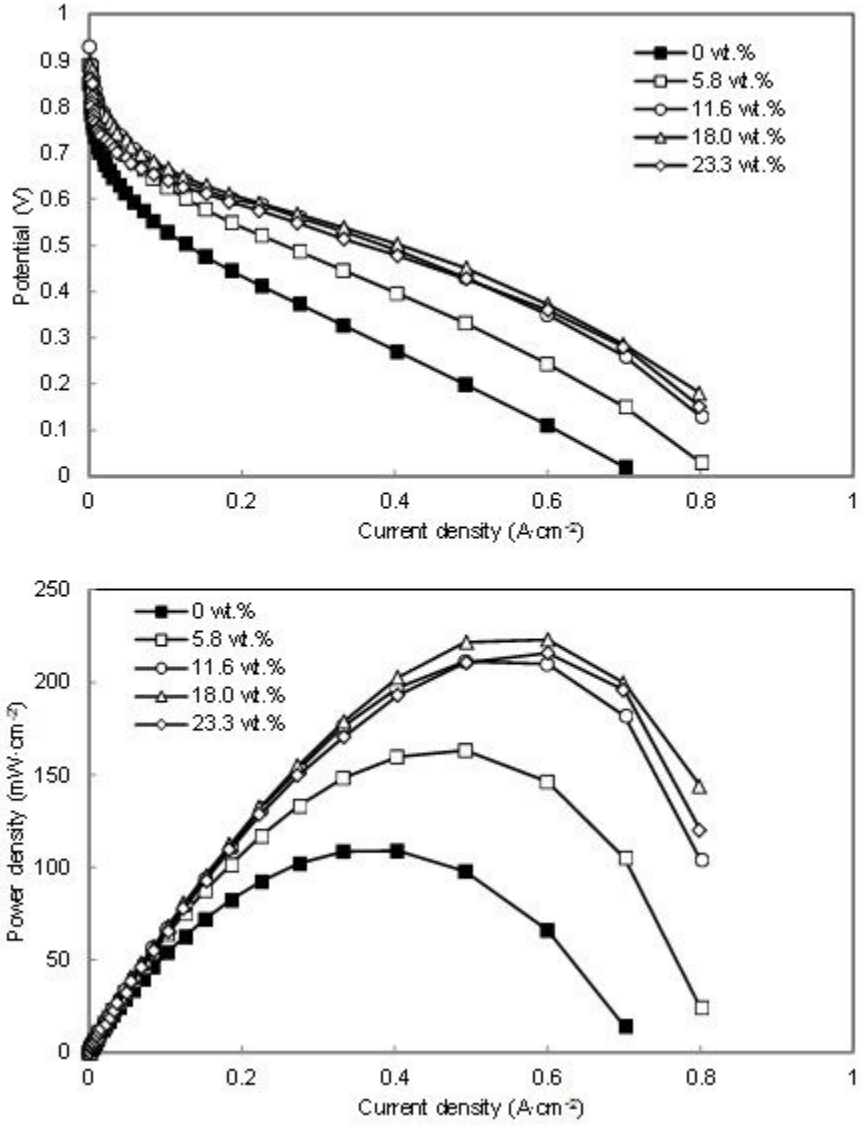

Figure 4.6: Polarization curves and power densities of PSA-Pt/ Vulcan MEAs 0.50 mg·cm^{-2}

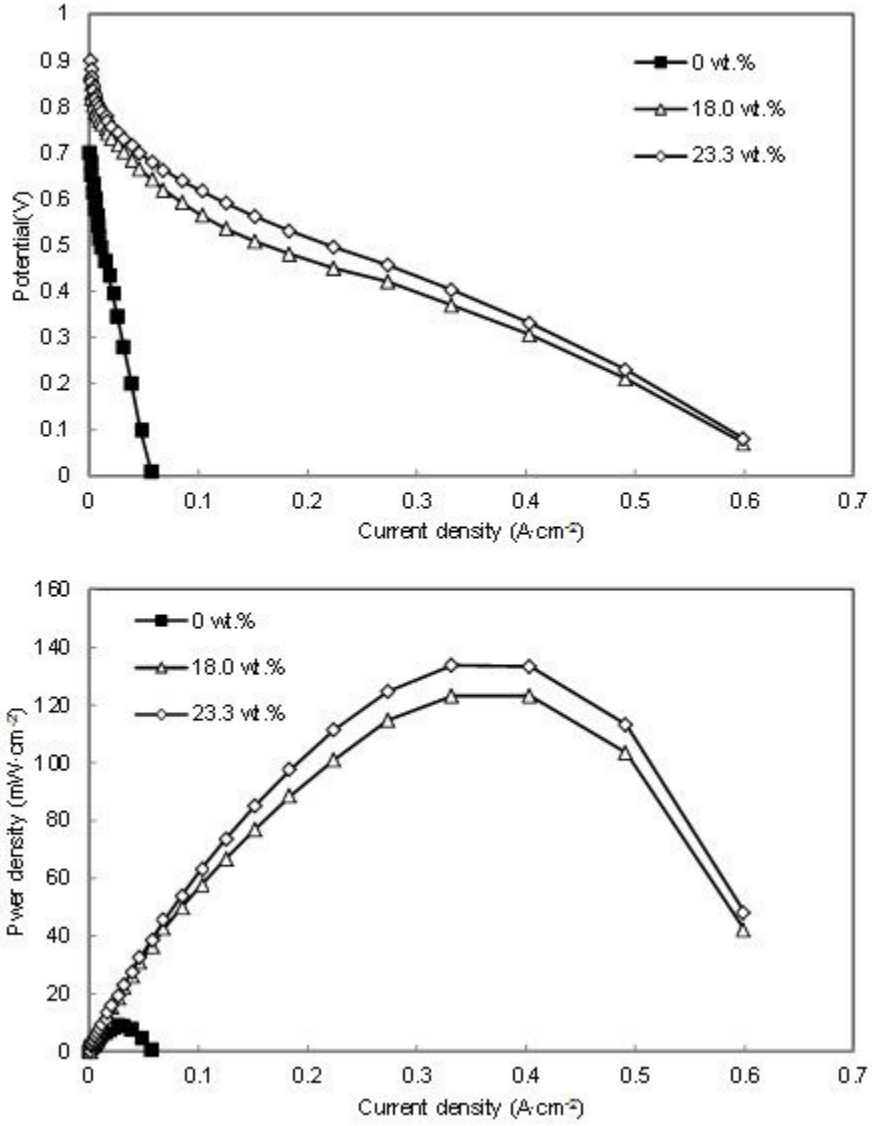

Figure 4.7: Polarization curves and power densities of PSA-Pt/ Vulcan MEAs 0.50 mg·cm^{-2}

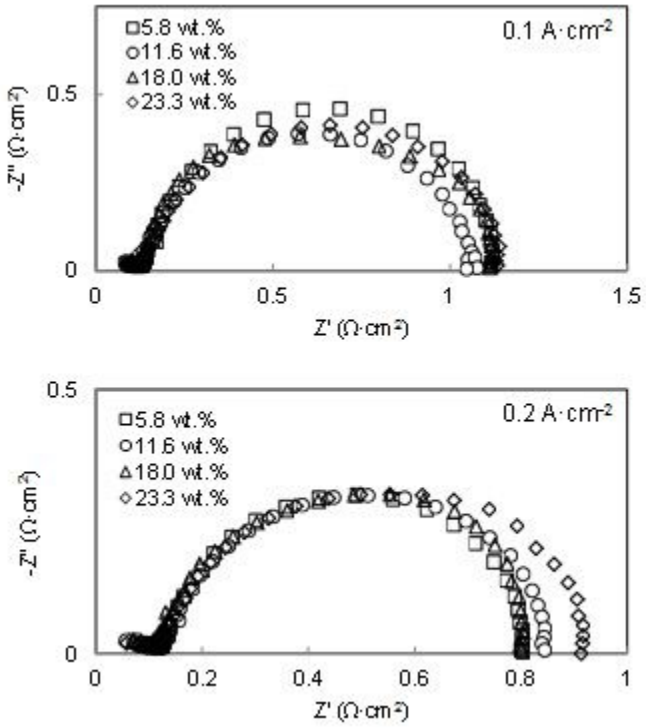

Figure 4.8: EIS plots at 0.1 and 0.2 A·cm^{-2} of PSA-Pt/ Vulcan MEAs with 0.50 mg·cm^{-2} Nafion in CL

were observed in MD3-50 and MD4-50, which resulted large potential loss in the fuel cell reaction.

The Nyquist plots shown in Figure 4.8 presented only one loop. The method for estimating the parameters in EIS has been introduced in chapter 3. At anode, the value of charge transfer resistance $R_{ct,a}$ was fixed at 10% of $R_{ct,c}$ and the exponent of CPE_a , n_a was fixed at 0.8. The parameters at cathode was estimated out by three steps. The variation of $R_{ct,c}$, $R_{d,c}$, C_c and $R_{ct,c}/R_{loop}$, with an estimated error in 10%, in PSA grafted MEAs, have been presented in Figure4.10.

Figure 4.10(a) showed the variation of $R_{ct,c}$ to i . In the PSA-MEAs with 0.5 mg·cm^{-2} Nafion in CL, the magnitude of $R_{ct,c}$ was relatively independent of PSA graft ratio. As the Nafion amount was reduced to 0.25 mg·cm^{-2}, the value of $R_{ct,c}$ increased, indicating low proton transfer efficient in less Nafion MEA.

The variation of $R_{d,c}$ was shown in Figure 4.10(b). At low current density, 0.1 and 0.2 A·cm^{-2}, the mass transfer effect was nearly negligible. The value at 0.1 A·cm^{-2}was around 0.15 Ω·cm^2. It increased slightly with current density, around 0.25 Ω·cm^{2}at 0.2 A·cm^{-2}. As PSA graft ratio increased from 5.8 to 23.3 wt.% , slight increase in

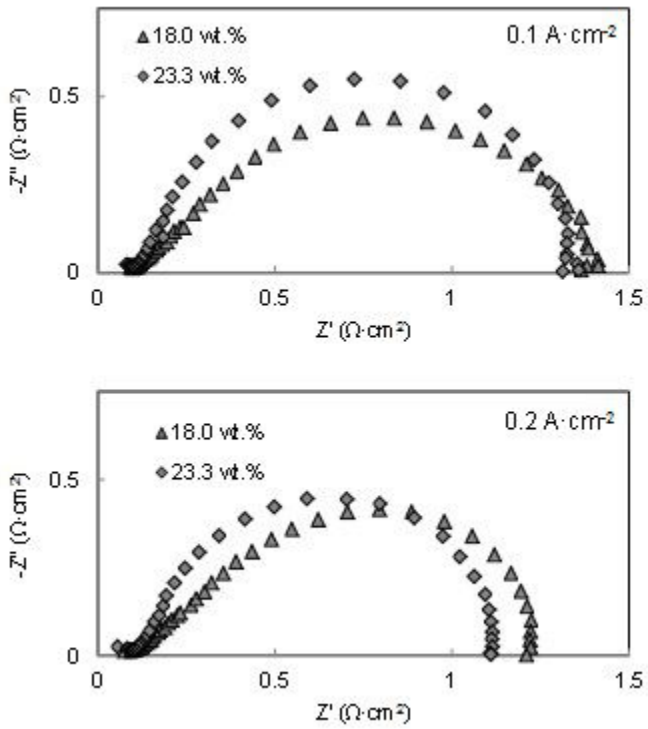

Figure 4.9: EIS plots at 0.1 and 0.2 A·cm^{-2} of PSA-Pt/ Vulcan MEAs with 0.20 mg·cm^{-2} Nafion in CL

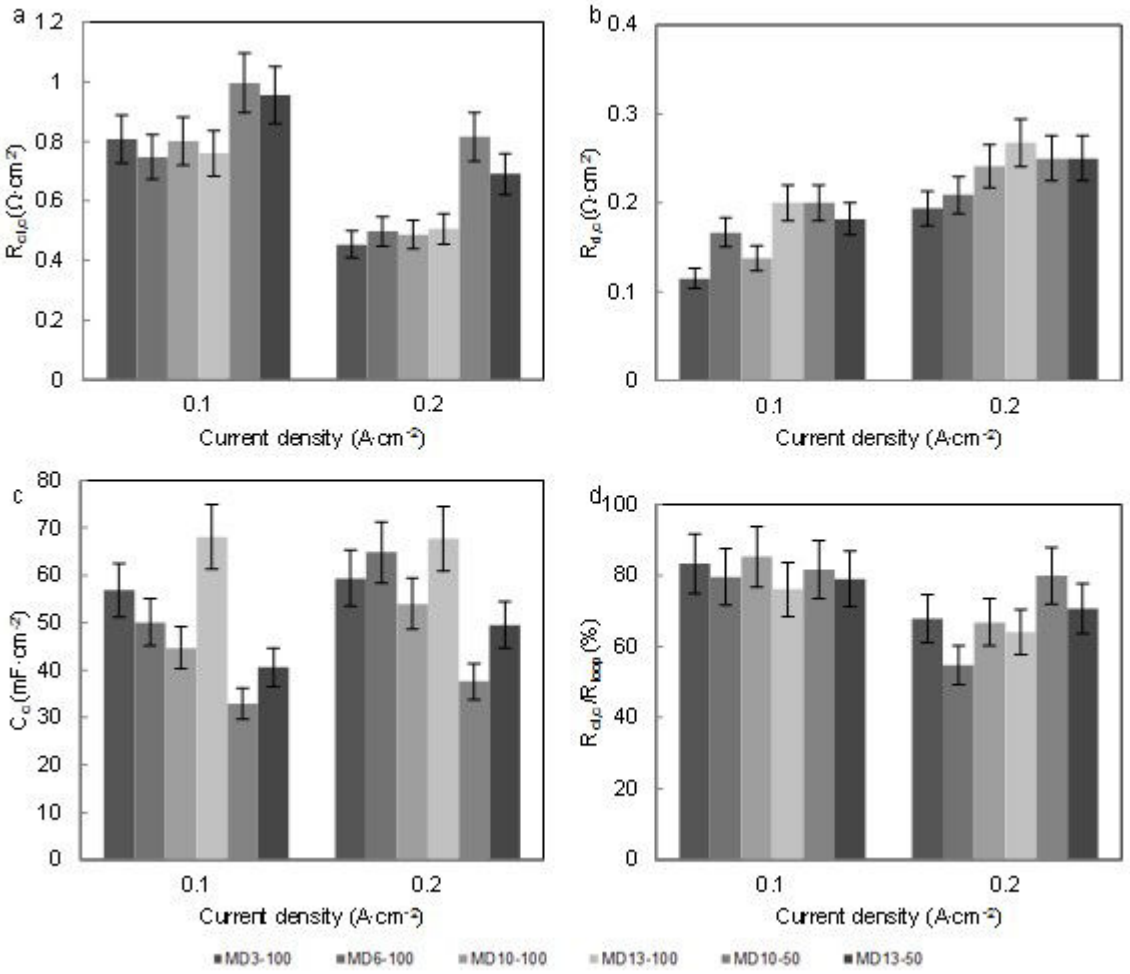

Figure 4.10: The variation of EIS parameters in PSA- MEAs

$R_{d,c}$ was presented, which might be associated with the hydrophilicity of PSA in the catalyst.

In Figure 4.10(c), it was shown the value of C_c increased slightly as current increased. The reduction in C_c in less-Nafion MEAs might be due to the membrane swelling in the double layer, where the connection between membrane and CL was relatively looser.

In Figure 4.10(d), the percentage of $R_{ct,c}/R_{loop}$ has been shown. In the current density at 0.1 and 0.2 A·cm^{-2}, charge transfer was the dominated factor in the cathodic reaction, consisting more than 50% of R_{loop}. As i increased, the ratio of $R_{ct,c}$ in R_{loop} decreased. At 0.2 A·cm^{-2}, the highest ratio was found in MD3-50, around 50%, as a result of its high charge transfer resistance as low amount of Nafion was added.

4.4 Ageing performance of MD3-100

The fuel cell investigation showed that the highest power density in fuel cell reaction was achieved by MEA MD3-100. Its ageing performances were studied in accelerated tests: H_2 and air were supplied to the anode and the cathode, and CV cycles were applied between 0.1 to 0.9V with a scan rate of 5 mV/s. The polarization curves after every 250 cycles were recorded in the chronopotentialmetry, by adjusting the current density (i) in a logarithm variations. MEA power densities, equal to the i.E, were plotted as a function of current density, accordingly. The impedance plots at 0.1, 0.2 and 0.4 $A{\cdot}cm^{-2}$ were also measured. ECSA of Pt catalysts during the ageing process were estimated by CV as N_2 supplied to the cathode. Also, the crossover of hydrogen in the MEA was evaluated by LSV, indicating change in the membrane during the ageing experiments.

4.4.1 Polarization properties of MD3-100

Figure4.11 showed the polarization curves after every 250 cycles, where the four cd regions according to different control factors during the fuel cell reaction were obviously depicted: open circuit voltage, activation process, ohmic loss process and mass transfer process. From 250 to 1500 cycles, visible improvements in the performances were observed in the four regions. First, OCV increased slightly from 0.88 to 0.91V. The difference between the real OCV and the theoretical value was due to the mixed potential and to existence of fuel crossover. The increase in OCV could be attributed to activation of the fuel cell system during the 1500 cycles, as a result of the humidification of membrane and the electrodes by water product. In the low density region from 0 to $0.1A{\cdot}cm^{-2}$, the cell potential drops sharply due to activation loss. The fuel cell potential at 0.02 $A{\cdot}cm^{-2}$ also increased during the ageing process from 250 to 1500 cycles. The increase in potential at 0.4 $A{\cdot}cm^{-2}$ indicated that relatively lower ohmic loss contributed the fuel cell reaction during the ageing – which appears here as a maturation. In the meanwhile, higher potential at 0.8 $A{\cdot}cm^{-2}$ was recorded after 1250 cycles could attain around 315 $mW{\cdot}cm^{-2}$.

In the polarization curves from 1750 to 3000 cycles, the OCV was around 0.91 and 0,92 V. The potential at 0.4 $A{\cdot}cm^{-2}$ was around 0.60V, with no obvious change in the ohmic loss process. The highest power density was observed after 1750 cycles, around 318 $mW{\cdot}cm^{-2}$, and the value after 3000 cycles was around 311 $mW{\cdot}cm^{-2}$. The ageing performances were further studied in EIS.

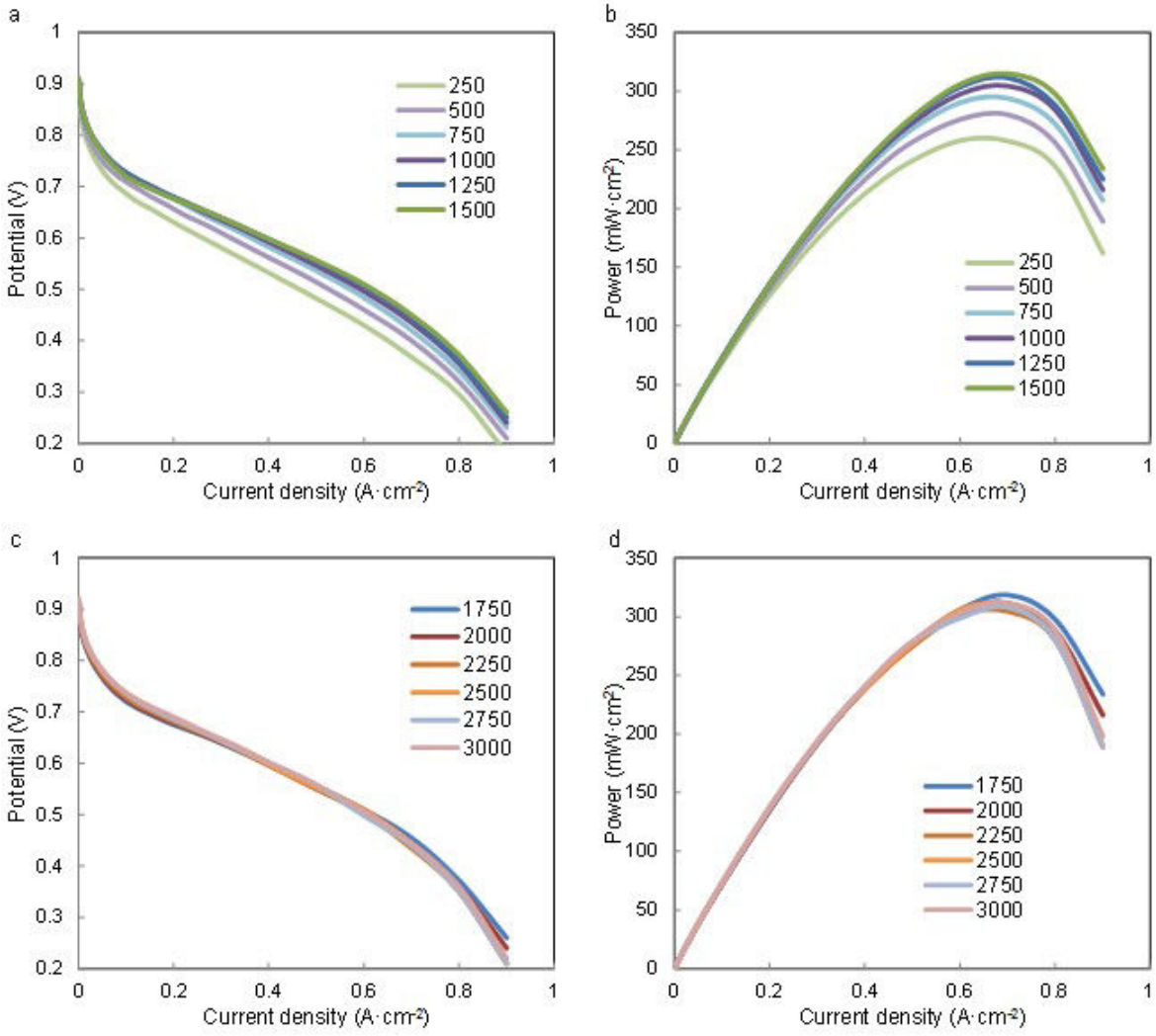

Figure 4.11: The polarization curves and power densities of MEA D3-100 in accelerated tests

4.4.2 EIS of MD3-100

The electrochemical spectra after every 250 cycles were measured at 0.1, 0.2 and 0.4 A·cm^{-2} and the Nyquist plots were shown in Figure4.12 and 4.13. In Figure4.12, the impedance loops after 250 cycles were obviously larger than the others. The diameter of the loops decreased as the cycle number increased – corresponding to the above mentioned maturation, with an exception of the impedance loops at 0.2 A·cm^{-2}. The diameters after 1250 and 1500 cycles were slightly larger than that after 1000 cycles. We further compared the impedance plots at 0.2 A·cm^{-2} from 1750 and 2000 cycles in Figure4.13, where the diameter decreased with the cycle number, as well as the loops at 0.1 A·cm^{-2}. The spectrum at 0.4 A·cm^{-2} after 3000 cycles was larger than that after 2500 cycles, which is linked to the degradation of the overall MEA.

The impedance spectra, with charge transfer loop and diffusion loop overlapping each other, were fitted to the equivalent circuit described above and the parameters in cathode were estimated. While the value of ohmic resistance was relatively independent of current or CV cycles, the variation of of $R_{ct,c}$, $R_{d,c}$, C_c and $R_{ct,c}/R_{loop}$, with an error estimated at 5%, were presented in Figure 4.14.

First, the value of $R_{ct,c}$ in Figure 4.14(a) decreased as measured current increased from 0.1 and 0.4 A·cm^{-2}. While the value at 0.1 and 0.2 A·cm^{-2} decreased slightly with cycling number, the fuel cell performances were activated in the low current range, in agreement with the results of polarization curves. $R_{ct,c}$ at 0.4 A·cm^{-2} was nearly constant during the ageing tests, whose value during the cycles fluctuated within 0.05 Ω·cm^{-2}. It may be concluded that no obvious loss in the charge transfer process in the reaction after 3000 cycles.

The variation of C_c was depicted in Figure 4.14(c): the value slightly increased as the measurement current increased from 0.1 to 0.4 A·cm^{-2}. After 3000 cycles, the value decreased a little, which may correspond to degradation of the catalyst.

In Figure 4.14(d), the variation of percentage of $R_{ct,c}/R_{loop}$ to the measured current density was shown. In the current range from 0.1 to 0.4 A·cm^{-2}, the main factor in the cathodic reaction was the charge transfer process, where $R_{ct,c}$ consisted more than 50% of R_{loop}. The ratio at 0.4 A·cm^{-2} was slightly lower that at 0.1 and 0.2 A·cm^{-2}. After 3000 cycles, the percentage at 0.4 A·cm^{-2} was around 56%. The EIS investigation showed that the main degradation after 2000 cycles would be attributed to the increase in diffusion resistance.

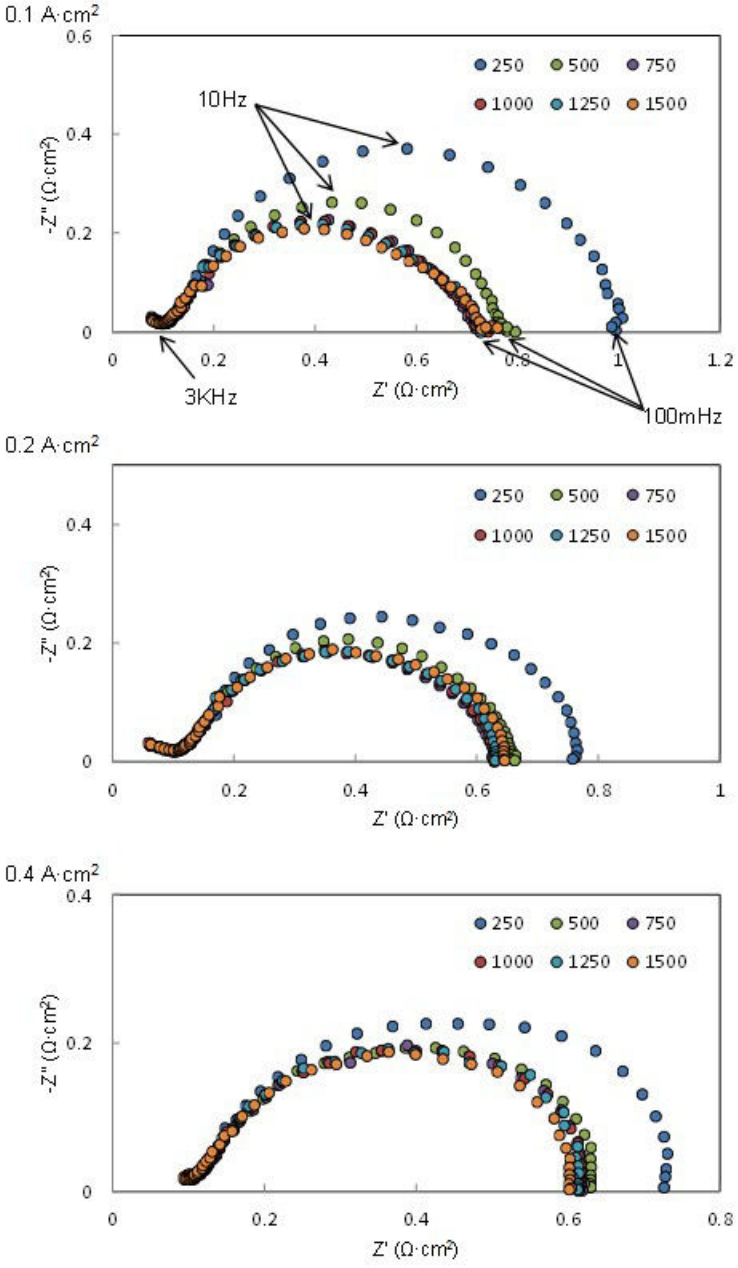

Figure 4.12: The Nyquist plots of MD3-100 after 250, 500, 750 and 1000, 1250 and 1500 cycles

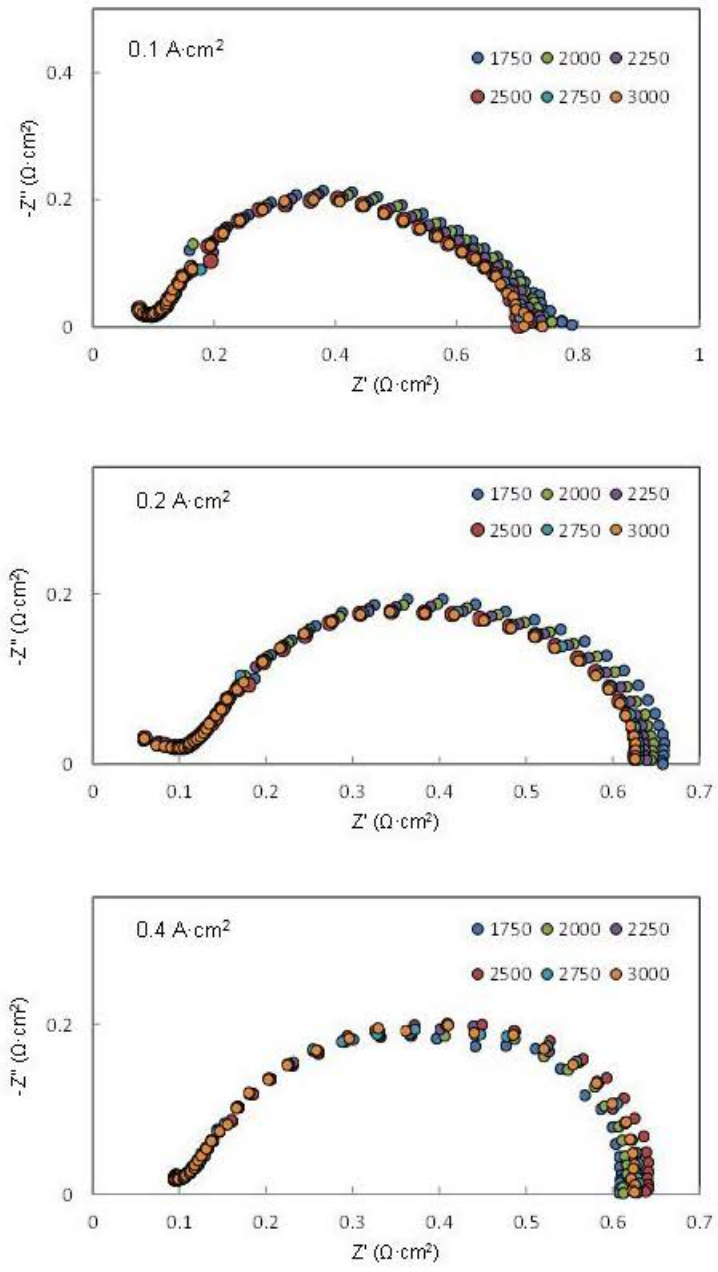

Figure 4.13: The Nyquist plots of MD3-100 after 1750, 2000, 2250, 2500, 2750 and 3000 cycles

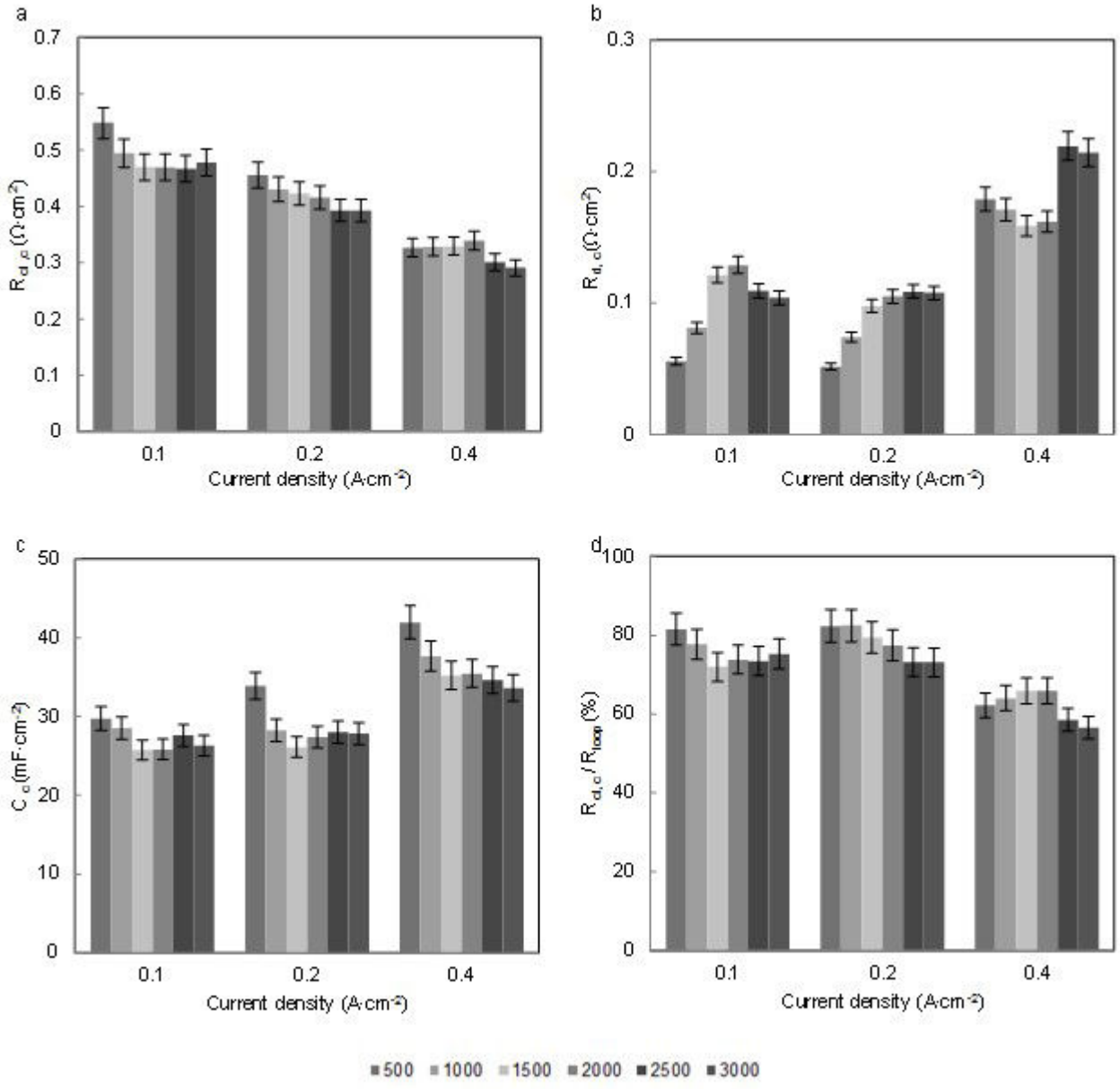

Figure 4.14: The EIS parameters of MD3-100 at 0.1, 0.2 and 0.4 A·cm^{-2} after 500, 1000, 1500, 2000, 2500 and 3000 cycles

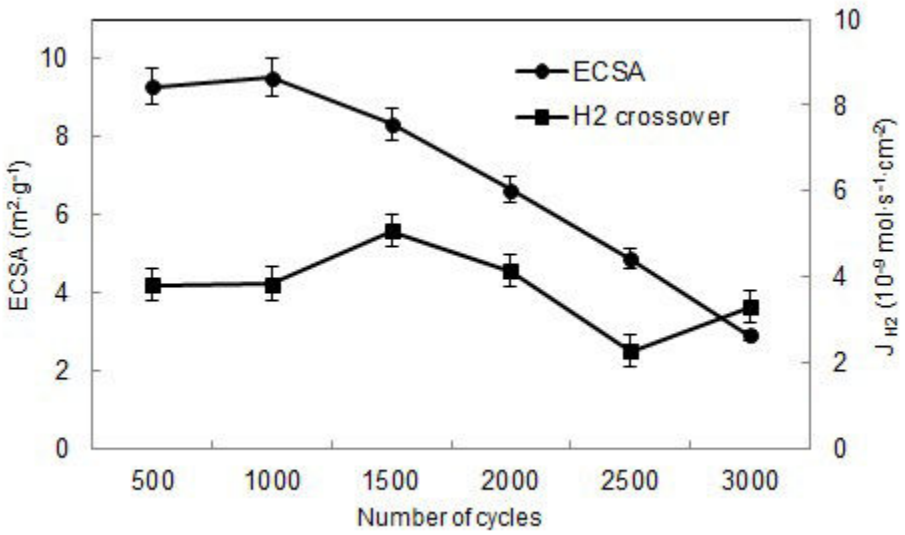

Figure 4.15: The variation of ECSA and hydrogen crossover rate of MD3-100 after 500, 1000, 1500, 2000, 2500 and 3000 cycles

4.4.3 ECSA and hydrogen crossover of MD3-100

After every 250 cycles, CV in nitrogen was carried out in the potential range from 0.05 to 0.5V with a scan rate of 50 mV/s. The hydrogen desorption peaks were integrated and the values of ECSA after every 500 cycles were given in Figure 4.15. In the first 1000 cycles, ECSA increased slightly. However, the value of ECSA decreased with time after 1000 cycles. After 3000 cycles, ECSA was around 2.9 $m^2 \cdot g^{-1}$, only 31% of that evaluated after 500 cycles, although no significant degradation in the power density was observed after 3000 cycles. According to Equation 1.31, the theoretical potential of the platinum oxidation was 0.88V/NHE. In the potential cycles between 0.1 to 0.9V, especially at high potential, a part of platinum particles was oxidized and lost the activity in the hydrogen adsorption/desorption tests.

LV method in nitrogen, scanning from 0.05 to 0.5V with a scan rate of 2 mV/s, was used to investigate the hydrogen crossover after the ageing tests, associated to the degradation of the membrane. It was presented in Figure 4.15 that, during the tests, the value of J_{H_2} was relatively constant during the CV cycles, around 4×10^{-9} $mol \cdot s^{-1} \cdot cm^{-2}$. Therefore, no obvious membrane degradation was revealed in the ageing test.

In conclusion, MEA D3-100 exhibited high stability during the 3000 CV cycles. The fuel cell properties were first activated during the first 1000 cycles, which demonstrated by the increase in ECSA. After that, although ECSA started to decrease, in

accordance with the decrease in the electrode capacitance, the power density in the fuel cell reaction increased, and the highest power density was obtained after 1750 cycles. As following, ageing of the catalysts started to be depicted in the polarization curves, which was attributed to the increase of diffusion resistance. The power density after 3000 cycles was around 311 $mW \cdot cm^{-2}$, depicted higher durability during the ADT process.

4.5 Conclusions

The influence of PSA graft on the surface characterization of Pt/Vulcan was first investigated in XRD and TEM. There was no obvious aggregation of platinum particles observed due to the diazonium reaction.

In half-cell test, the influence of GDL type and Nafion ratio in CL have been discussed in the electrodes with PSA grafted catalysts.

As Nafion ratio decreased, ORR performance was reduced. While carbon paper with a micro-porous layer on the surface was used as GDL, significant improvement was observed during ORR.

Deposited on CP-GDL, Pt/Vulcan catalyst grafted with 11.6 and 23.3 wt.% PSA showed lower ORR current density than that of non-functionalized catalyst. With the presence of MCP, the improved ORR performance of 23.3 wt.% PSA grafted Pt/Vulcan catalyst proved feasibility of PSA sulfonation. Higher reduction current was obtained, with relatively lower Tafel slopes. The diameter of the impedance loops were shown to be lower than the others.

The prepared MEAs with PSA grafted catalyst were studied in a single cell at ambient temperature. Developments in fuel cell performances were achieved because of the sulfonation of PSA graft onto the carbon support. The highest power density was obtained in the MEA with 18.0 wt.% PSA graft. Compared with non-functionalized catalyst, the fuel cell performances was significantly improved because of comparatively lower charge transfer resistance presented in EIS. The fuel cell performance decreased as Nafion amount decreased from 0.50 to 0.25 $mg \cdot cm^{-2}$. However, the performances of less-Nafion MEAs were still improved by the sulfonation of catalysts.

The MEA prepared with 18.0% PSSA grafted catalysts and 0.50 $mg \cdot cm^{-2}$Nafion exhibited high stability during the ADT cycles. The power density in the fuel cell reaction increased, and attained the top after 1750 cycles, around $318 mW \cdot cm^{-2}$. After that, the increase of diffusion resistance resulted in the degradation of the fuel cell. The polarization curves presented that, after 3000 cycles, the power density was

around 311 $mW \cdot cm^{-2}$, slightly lower than the maximum value.

Conclusions

Pt/ Vulcan catalyst, grafted with polystyrene sulfonate (PSSA) and 4-phenysulfonic acid (PSA), respectively, was studied in XRD and TEM. No obvious aggregation was observed due to the sulfonation.

In the half-cell tests, comparatively higher $ECSA$ was observed in MCP supported electrodes. In ORR investigation, MCP-electrodes exhibited higher current density, as well as smaller impedance loops presented in the Nyquist plots. Therefore, MCP was selected as the GDL in the preparation of MEA.

As to the influence of PSSA graft ratio, it was found that ORR current increased as the ratio increased from 0 to 5 and 10 wt.% , but decreased at 20 wt.%. In the fuel cell tests of the MEAs with PSSA grafted catalysts, improved performances were achieved after the sulfonation of Pt/ Vulcan catalyst with 5 and 10 wt.% PSSA, which was consistent with the researches in half-cells. In EIS method, it was observed that both charge transfer resistance and diffusion resistance were reduced by the sulfonation of catalysts. It was concluded that the functionalization of catalysts with PSSA graft could improve the fuel cell reaction by promoting the proton transportation in the fuel cell reaction and also water diffusion during the operation.

In half-cell tests of PSA grafted catalysts, only the one grafted with 23.3 wt.% PSA exhibited higher performance than non-functionalized catalysts, with higher reduction current in LSV and relatively low Tafel slope. The diameter of the impedance loops were shown to be lower than the others. The prepared MEAs with 5.8, 11.6, 18.0 and 23.3 wt.% PSA grafted catalysts were studied in a single cell and their polarization curves presented that the current density obviously improved because of the PSA graft. The ageing performances of the MEA with 18.0 wt.% PSSA grafted catalysts were studied in cycles between 0.1 and 0.9V. The polarization curves presented that, after 3000 cycles, the power density was around 311 $mW \cdot cm^{-2}$, slightly lower than the maximum value, 318 $mW \cdot cm^{-2}$ after 1750 cycles.

As the Nafion ratio in CL decreased from 0.50 to 0.25 $mg \cdot cm^{-2}$, the ORR current in half-cells was reduced. In fuel cell tests, the performances of less-Nafion MEAs

were improved by the sulfonation of catalysts, though most of them performed lower power density than their counterparts with 0.50 mg·cm^{-2}in CL. With an exception, the MEAs, with 10 and 20 wt.% PSSA graft in the catalysts, exhibited higher power density with low Nafion addition.

In conclusion, because of the presence of PSSA or PSA, the performances of MEAs with low amount of Nafion addition were improved. The sulfonation of catalysts with PSSA successfully reduced the Nafion amount in CL. The one, containing 0.25 mg·cm^{-2}Nafion in CL and 10 wt.% PSSA in catalyst, performed a power density, 201 mW·cm^{-2}, higher than that with 0.50 mg·cm^{-2}Nafion.

Due to the presence of liquid solution in there-electrode system, the accuracy of the half-cells was highly dependent on the stability of the prepared half-cell electrodes. In the discussion of the Nafion effect in half cell, less Nafion electrodes resulted loose interface between membrane and CL, which would absorb water during the half-cell test and affect the results. The application of less Nafion in CLs with sulfonated grafted catalysts was verified in the investigation of MEAs.

Acknowledgment

My deepest gratitude goes first to François Lapicque and Carolline Bonnet, my supervisors, for their constant encouragement, patience and expert advice.

I also wish to extend my thanks to Thi-Thao Nguyen, Sébastien Fontana, Alexandre Desforges, Jean-François Maréché from IJL (Institut Jean Lamour), who supplied my work with electrode matrials. My work also owes much to Gaël Maranzana and Thomas Gaumont from LEMTA (Laboratoire d'Energétique et de Mécanique Théorique et Appliquée) for their great helps in fuel cell tests.

Special thanks go to financil support from Institut Carnot (ICEEL) and China Scholarship Council (CSC).

My thanks would go to all the collegues in group Syspol, for their kindness and helps during the last three years.

And in the end, I would like express my gratitude to to my families, to my husband for their endless love and selfless support.

Bibliography

[1] Zhang, J. (2008). PEM fuel cell electrocatalysts and catalyst layers: fundamentals and applications, Springer.

[2] Yuan, X.-Z., C. Song, et al. (2010). "Electrochemical impedance spectroscopy in PEM fuel cells." Fundamentals and ApplicationsSpringer-Verlag, London.

[3] Larminie, J., A. Dicks, et al. (2003). Fuel cell systems explained, Wiley New York.

[4] Ramaswamy, N., N. Hakim, et al. (2008). "Degradation mechanism study of perfluorinated proton exchange membrane under fuel cell operating conditions." Electrochimica Acta 53(8): 3279-3295.

[5] Kim, S. and I. Hong (2010). "Membrane performance comparison in a proton exchange membrane fuel cell (PEMFC) stack." Journal of Industrial and Engineering Chemistry 16(6): 901-905.

[6] Schlick, S. (1996). Ionomers: characterization, theory, and applications, CRC Press.

[7] Ijeri, V., L. Cappelletto, et al. (2010). "Nafion and carbon nanotube nanocomposites for mixed proton and electron conduction." Journal of Membrane Science 363(1): 265-270.

[8] Kim, Y., K. Y. Kang, et al. (2011). "A composite electrolyte membrane containing high-content sulfonated carbon spheres for proton exchange membrane fuel cells." Carbon 49(4): 1367-1373.

[9] Peighambardoust, S., S. Rowshanzamir, et al. (2010). "Review of the proton exchange membranes for fuel cell applications." International Journal of Hydrogen Energy 35(17): 9349-9384.

[10] Strathmann, H. (1995). "Electrodialysis and related processes." Membrane Science and Technology 2: 213-281.

[11] Cappadonia, M., J. W. Erning, et al. (1995). "Conductance of Nafion 117 membranes as a function of temperature and water content." Solid State Ionics 77: 65-69.

[12] Beattie, P. D., F. P. Orfino, et al. (2001). "Ionic conductivity of proton exchange membranes." Journal of Electroanalytical Chemistry 503(1): 45-56.

[13] Wang, S., Y. Zhang, et al. (2012). "Portable PEMFC stack using sulfonated poly (fluorenyl ether ketone) ionomer as membrane." International Journal of Hydrogen Energy 37(5): 4539-4544.

[14] Chen, S.-L., A. Bocarsly, et al. (2005). "Nafion-layered sulfonated polysulfone fuel cell membranes." Journal of Power Sources 152: 27-33.

[15] Alberti, G., M. Casciola, et al. (2007). "Novel Nafion–zirconium phosphate nanocomposite membranes with enhanced stability of proton conductivity at medium temperature and high relative humidity." Electrochimica Acta 52(28): 8125-8132.

[16] Nam, S.-E., S.-O. Kim, et al. (2008). "Preparation of Nafion/sulfonated poly (phenylsilsesquioxane) nanocomposite as high temperature proton exchange membranes." Journal of Membrane Science 322(2): 466-474.

[17] Santiago, E., R. Isidoro, et al. (2009). "Nafion-TiO_2 hybrid electrolytes for stable operation of PEM fuel cells at high temperature." Electrochimica Acta 54(16): 4111-4117.

[18] Amjadi, M., S. Rowshanzamir, et al. (2010). "Investigation of physical properties and cell performance of Nafion/TiO_2 nanocomposite membranes for high temperature PEM fuel cells." International Journal of Hydrogen Energy 35(17): 9252-9260.

[19] Wang, Z., H. Tang, et al. (2011). "Self-assembly of durable Nafion/TiO_2 nanowire electrolyte membranes for elevated-temperature PEM fuel cells." Journal of Membrane Science 369(1): 250-257.

[20] Ke, C.-C., X.-J. Li, et al. (2011). "Investigation on sulfuric acid sulfonation of in-situ sol–gel derived Nafion/SiO_2 composite membrane." International Journal of Hydrogen Energy 36(5): 3606-3613.

[21] Paul, D. K., A. Fraser, et al. (2011). "Towards the understanding of proton conduction mechanism in PEMFC catalyst layer: Conductivity of adsorbed Nafion films." Electrochemistry Communications 13(8): 774-777.

[22] Yu, D., I. Sung, et al. (2013). "Properties of Sulfonated Poly (Arylene Ether Sulfone)/Functionalized Carbon Nanotube Composite Membrane for High Temperature PEMFCs." Fuel Cells 13(5): 843-850.

[23] Wang, Y., K. S. Chen, et al. (2011). "A review of polymer electrolyte membrane fuel cells: technology, applications, and needs on fundamental research." Applied Energy 88(4): 981-1007.

[24] Perng, S.-W. and H.-W. Wu (2010). "Effect of the prominent catalyst layer surface on reactant gas transport and cell performance at the cathodic side of a PEMFC." Applied Energy 87(4): 1386-1399.

[25] Şayin, E. S., A. Bayrakçeken, et al. (2012). "Durability of PEM fuel cell electrocatalysts prepared by microwave irradiation technique." International Journal of Hydrogen Energy 37(21): 16663-16672.

[26] Yazdanpour, M., A. Esmaeilifar, et al. (2012). "Effects of hot pressing conditions on the performance of Nafion membranes coated by ink-jet printing of Pt/MWCNTs electrocatalyst for PEMFCs." International Journal of Hydrogen Energy 37(15): 11290-11298.

[27] Sode, A., N. Ingle, et al. (2011). "Controlling the deposition of Pt nanoparticles within the surface region of Nafion." Journal of Membrane Science 376(1): 162-169.

[28] Mehmood, A. and H. Y. Ha (2012). "An efficient decal transfer method using a roll-press to fabricate membrane electrode assemblies for direct methanol fuel cells." International Journal of Hydrogen Energy 37(23): 18463-18470.

[29] Jung, H.-Y., J.-Y. Kim, et al. (2011). "Effect of Nafion dispersion solvent on the interfacial properties between the membrane and the electrode of a polymer electrolyte membrane-based fuel cell." Solid State Ionics 196(1): 73-78.

[30] Bayrakçeken, A., S. Erkan, et al. (2008). "Effects of membrane electrode assembly components on proton exchange membrane fuel cell performance." International Journal of Hydrogen Energy 33(1): 165-170.

[31] Song, C. and P. Pickup (2004). "Effect of hot pressing on the performance of direct methanol fuel cells." Journal of applied electrochemistry 34(10): 1065-1070.

[32] Jung, H.-Y., K.-Y. Cho, et al. (2007). "Sulfonated poly (arylene ether sulfone) as an electrode binder for direct methanol fuel cell." Electrochimica Acta 52(15): 4916-4921.

[33] Zhang, F., H. Zhang, et al. (2011). "Poly (vinylidene fluoride) based anion conductive ionomer as a catalyst binder for application in anion exchange membrane fuel cell." Journal of Power Sources 196(6): 3099-3103.

[34] An, L., T. Zhao, et al. (2013). "Agar chemical hydrogel electrode binder for fuel-electrolyte-fed fuel cells." Applied Energy 109: 67-71.

[35] Su, H., S. Pasupathi, et al. (2013). "Optimization of gas diffusion electrode for polybenzimidazole-based high temperature proton exchange membrane fuel cell: evaluation of polymer binders in catalyst layer." International Journal of Hydrogen Energy 38(26): 11370-11378.

[36] Wang, X., Y. Feng, et al. (2010). "Power generation using adjustable Nafion/PTFE mixed binders in air-cathode microbial fuel cells." Biosensors and Bioelectronics 26(2): 946-948.

[37] Velayutham, G. (2011). "Effect of micro-layer PTFE on the performance of PEM fuel cell electrodes." International Journal of Hydrogen Energy 36(22): 14845-14850.

[38] Oh, K.-H., W.-K. Kim, et al. (2011). "A hydrophobic blend binder for anti-water flooding of cathode catalyst layers in polymer electrolyte membrane fuel cells." International Journal of Hydrogen Energy 36(21): 13695-13702.

[39] Gharibi, H., M. Javaheri, et al. (2011). "Optimization of the amount of Nafion in multi-walled carbon nanotube/Nafion composites as Pt supports in gas diffusion electrodes for proton exchange membrane fuel cells." International Journal of Hydrogen Energy 36(20): 13325-13334.

[40] Scibioh, M. A., I.-H. Oh, et al. (2008). "Investigation of various ionomer-coated carbon supports for direct methanol fuel cell applications." Applied Catalysis B: Environmental 77(3): 373-385.

[41] Du, S., B. Millington, et al. (2011). "The effect of Nafion ionomer loading coated on gas diffusion electrodes with in-situ grown Pt nanowires and their durability in proton exchange membrane fuel cells." International Journal of Hydrogen Energy 36(7): 4386-4393.

[42] Antolini, E., L. Giorgi, et al. (1999). "Influence of Nafion loading in the catalyst layer of gas-diffusion electrodes for PEFC." Journal of Power Sources 77(2): 136-142.

[43] Passalacqua, E., F. Lufrano, et al. (2001). "Nafion content in the catalyst layer of polymer electrolyte fuel cells: effects on structure and performance." Electrochimica Acta 46(6): 799-805.

[44] Lai, C.-M., J.-C. Lin, et al. (2008). "Contribution of Nafion loading to the activity of catalysts and the performance of PEMFC." International Journal of Hydrogen Energy 33(15): 4132-4137.

[45] Lee, D. and S. Hwang (2008). "Effect of loading and distributions of Nafion ionomer in the catalyst layer for PEMFCs." International Journal of Hydrogen Energy 33(11): 2790-2794.

[46] Gostick, J. T., M. A. Ioannidis, et al. (2009). "On the role of the microporous layer in PEMFC operation." Electrochemistry Communications 11(3): 576-579.

[47] Yang, H., H.-C. Tu, et al. (2010). "Carbon cloth based on PAN carbon fiber practicability for PEMFC applications." International Journal of Hydrogen Energy 35(7): 2791-2795.

[48] Chun, J. H., K. T. Park, et al. (2011). "Development of a novel hydrophobic/hydrophilic double micro porous layer for use in a cathode gas diffusion layer in PEMFC." International Journal of Hydrogen Energy 36(14): 8422-8428.

[49] Park, S., J.-W. Lee, et al. (2012). "A review of gas diffusion layer in PEM fuel cells: materials and designs." International Journal of Hydrogen Energy 37(7): 5850-5865.

[50] Gostick, J. T., M. A. Ioannidis, et al. (2009). "Wettability and capillary behavior of fibrous gas diffusion media for polymer electrolyte membrane fuel cells." Journal of Power Sources 194(1): 433-444.

[51] Debe, M. K. (2012). "Electrocatalyst approaches and challenges for automotive fuel cells." Nature 486(7401): 43-51.

[52] Wikander, K., H. Ekström, et al. (2007). "On the influence of Pt particle size on the PEMFC cathode performance." Electrochimica Acta 52(24): 6848-6855.

[53] Xu, Z., H. Zhang, et al. (2012). "Effect of particle size on the activity and durability of the Pt/C electrocatalyst for proton exchange membrane fuel cells." Applied Catalysis B: Environmental 111: 264-270.

[54] Sarma, L. S., T. D. Lin, et al. (2005). "Carbon-supported Pt–Ru catalysts prepared by the Nafion stabilized alcohol-reduction method for application in direct methanol fuel cells." Journal of Power Sources 139(1): 44-54.

[55] Jha, N., A. Leela Mohana Reddy, et al. (2008). "Pt–Ru/multi-walled carbon nanotubes as electrocatalysts for direct methanol fuel cell." International Journal of Hydrogen Energy 33(1): 427-433.

[56] Vila, N., M. V. Brussel, et al. (2007). "Metallic and bimetallic Cu/Pt species supported on carbon surfaces by means of substituted phenyl groups." Journal of Electroanalytical Chemistry 609(2): 85-93.

[57] Zhou, Z.-M., Z.-G. Shao, et al. (2010). "Durability study of Pt–Pd/C as PEMFC cathode catalyst." International Journal of Hydrogen Energy 35(4): 1719-1726.

[58] Garcia, A. C., V. A. Paganin, et al. (2008). "CO tolerance of PdPt/C and PdPtRu/C anodes for PEMFC." Electrochimica Acta 53(12): 4309-4315.

[59] Trongchuankij, W., K. Pruksathorn, et al. (2011). "Preparation of a high performance Pt–Co/C electrocatalyst for oxygen reduction in PEM fuel cell via a combined process of impregnation and seeding." Applied Energy 88(3): 974-980.

[60] Lin, R., C. Cao, et al. (2013). "Synthesis and application of core–shell CoPt/C electrocatalysts for proton exchange membrane fuel cells." Journal of Power Sources 223: 190-198.

[61] Antolini, E., J. Salgado, et al. (2005). "Effects of geometric and electronic factors on ORR activity of carbon supported Pt–Co electrocatalysts in PEM fuel cells." International Journal of Hydrogen Energy 30(11): 1213-1220.

[62] Othman, R., A. L. Dicks, et al. (2012). "Non precious metal catalysts for the PEM fuel cell cathode." International Journal of Hydrogen Energy 37(1): 357-372.

[63] Liu, G., X. Li, et al. (2009). "Development of non-precious metal oxygen-reduction catalysts for PEM fuel cells based on N-doped ordered porous carbon." Applied Catalysis B: Environmental 93(1): 156-165.

[64] Hussein, L., Y. Feng, et al. (2011). "Functionalized-carbon nanotube supported electrocatalysts and buckypaper-based biocathodes for glucose fuel cell applications." Electrochimica Acta 56(22): 7659-7665.

[65] Calvillo, L., M. Gangeri, et al. (2011). "Synthesis and performance of platinum supported on ordered mesoporous carbons as catalyst for PEM fuel cells: effect of the surface chemistry of the support." International Journal of Hydrogen Energy 36(16): 9805-9814.

[66] Guo, S., S. Zhang, et al. (2013). "Tuning nanoparticle catalysis for the oxygen reduction reaction." Angewandte Chemie International Edition 52(33): 8526-8544.

[67] Lo, A.-Y., C.-T. Hung, et al. (2012). "Syntheses of carbon porous materials with varied pore sizes and their performances as catalyst supports during methanol oxidation reaction." Applied Energy 100: 66-74.

[68] Carmo, M., T. Roepke, et al. (2009). "A novel electrocatalyst support with proton conductive properties for polymer electrolyte membrane fuel cell applications." Journal of Power Sources 191(2): 330-337.

[69] Sugawara, Y., A. P. Yadav, et al. (2011). "Dissolution and surface area loss of platinum nanoparticles under potential cycling." Journal of Electroanalytical Chemistry 662(2): 379-383.

[70] Niu, J. J. and J. N. Wang (2010). "Temperature and structural dependence of electrochemical activity and fuel cell performance." Acta Materialia 58(2): 408-414.

[71] Sharma, S. and B. G. Pollet (2012). "Support materials for PEMFC and DMFC electrocatalysts—a review." Journal of Power Sources 208: 96-119.

[72] Saha, M. S. and A. Kundu (2010). "Functionalizing carbon nanotubes for proton exchange membrane fuel cells electrode." Journal of Power Sources 195(19): 6255-6261.

[73] Mamat, M., S. Grigoriev, et al. (2010). "The performance and degradation of Pt electrocatalysts on novel carbon carriers for PEMFC applications." International Journal of Hydrogen Energy 35(14): 7580-7587.

[74] Saha, M. S., R. Li, et al. (2009). "3-D composite electrodes for high performance PEM fuel cells composed of Pt supported on nitrogen-doped carbon nanotubes grown on carbon paper." Electrochemistry Communications 11(2): 438-441.

[75] Balgis, R., G. M. Anilkumar, et al. (2012). "Nanostructured design of electrocatalyst support materials for high-performance PEM fuel cell application." Journal of Power Sources 203: 26-33.

[76] Saha, M. S., V. Neburchilov, et al. (2013). "Nanomaterials supported Pt catalysts for proton exchange membrane fuel cells." Wiley Interdisciplinary Reviews: Energy and Environment 2(1): 31-51.

[77] Yang, H., J. Lee, et al. (2012). "Effect of functionalization for carbon molecular sieve (CMS) synthesized using zeolite template on the incorporation of Pt nanoparticle and performance of the electrodes in PEMFC." Microporous and Mesoporous Materials 152: 148-156.

[78] Duksh, Y. S., B. K. Kaushik, et al. (2010). "Performance comparison of carbon nanotube, nickel silicide nanowire and copper VLSI interconnects: Perspectives and challenges ahead." Journal of Engineering, Design and Technology 8(3): 334-353.

[79] Dameron, A. A., S. Pylypenko, et al. (2012). "Aligned carbon nanotube array functionalization for enhanced atomic layer deposition of platinum electrocatalysts." Applied Surface Science 258(13): 5212-5221.

[80] Peng, F., L. Zhang, et al. (2005). "Sulfonated carbon nanotubes as a strong protonic acid catalyst." Carbon 43(11): 2405-2408.

[81] Gharibi, H., M. Javaheri, et al. (2011). "Optimization of the amount of Nafion in multi-walled carbon nanotube/Nafion composites as Pt supports in gas diffusion electrodes for proton exchange membrane fuel cells." International Journal of Hydrogen Energy 36(20): 13325-13334.

[82] Yin, S., P. K. Shen, et al. (2009). "Functionalization of carbon nanotubes by an effective intermittent microwave heating-assisted HF/ H_2O_2 treatment for electrocatalyst support of fuel cells." Electrochimica Acta 54(27): 6954-6958.

[83] Sato, Y., K. Shibata, et al. (2005). "Strict preparation and evaluation of water-soluble hat-stacked carbon nanofibers for biomedical application and their high biocompatibility: influence of nanofiber-surface functional groups on cytotoxicity." Mol. BioSyst. 1(2): 142-145.

[84] Álvarez, G., F. Alcaide, et al. (2011). "Electrochemical stability of carbon nanofibers in proton exchange membrane fuel cells." Electrochimica Acta 56(25): 9370-9377.

[85] Álvarez, G., F. Alcaide, et al. (2012). "Electrochemical performance of low temperature PEMFC with surface tailored carbon nanofibers as catalyst support." International Journal of Hydrogen Energy 37(1): 393-404.

[86] Sebastián, D., J. Calderón, et al. (2010). "Influence of carbon nanofiber properties as electrocatalyst support on the electrochemical performance for PEM fuel cells." International Journal of Hydrogen Energy 35(18): 9934-9942.

[87] Calvillo, L., M. Gangeri, et al. (2009). "Effect of the support properties on the preparation and performance of platinum catalysts supported on carbon nanofibers." Journal of Power Sources 192(1): 144-150.

[88] Guha, A., T. A. Zawodzinski Jr, et al. (2007). "Evaluation of electrochemical performance for surface-modified carbons as catalyst support in polymer electrolyte membrane (PEM) fuel cells." Journal of Power Sources 172(2): 530-541.

[89] Suzuki, S. (2013). Synthesis and applications of carbon nanotubes and their Composites, InTech.

[90] Chen, X., S. Zhang, et al. (2003). "Mechanics of a carbon nanocoil." Nano Letters 3(9): 1299-1304.

[91] Sevilla, M., C. Sanchís, et al. (2009). "Highly dispersed platinum nanoparticles on carbon nanocoils and their electrocatalytic performance for fuel cell reactions." Electrochimica Acta 54(8): 2234-2238.

[92] Park, K.-W., Y.-E. Sung, et al. (2004). "Origin of the enhanced catalytic activity of carbon nanocoil-supported PtRu alloy electrocatalysts." The Journal of Physical Chemistry B 108(3): 939-944.

[93] Ju, S.-P., J.-S. Lin, et al. (2014). "A molecular dynamics study of the mechanical properties of a double-walled carbon nanocoil." Computational Materials Science 82: 92-99.

[94] Barranco, V., V. Celorrio, et al. (2012). "Carbon nanocoils as unusual electrode materials for supercapacitors." Journal of The Electrochemical Society 159(4): A464-A469.

[95] Hyeon, T., S. Han, et al. (2003). "High-performance direct methanol fuel cell electrodes using solid-phase synthesized carbon nanocoils." Angewandte Chemie 115(36): 4488-4492.

[96] Lázaro, M., V. Celorrio, et al. (2011). "Influence of the synthesis method on the properties of Pt catalysts supported on carbon nanocoils for ethanol oxidation." Journal of Power Sources 196(9): 4236-4241.

[97] http://www.aerogel.org/?p=71

[98] Pekala, R., J. Farmer, et al. (1998). "Carbon aerogels for electrochemical applications." Journal of non-crystalline solids 225: 74-80.

[99] Moreno-Castilla, C. and F. Maldonado-Hódar (2005). "Carbon aerogels for catalysis applications: An overview." Carbon 43(3): 455-465.

[100] Smirnova, A., X. Dong, et al. (2005). "Novel carbon aerogel-supported catalysts for PEM fuel cell application." International Journal of Hydrogen Energy 30(2): 149-158.

[101] Job, N., J. Marie, et al. (2008). "Carbon xerogels as catalyst supports for PEM fuel cell cathode." Energy Conversion and Management 49(9): 2461-2470.

[102] Marie, J., R. Chenitz, et al. (2009). "Highly porous PEM fuel cell cathodes based on low density carbon aerogels as Pt-support: Experimental study of the mass-transport losses." Journal of Power Sources 190(2): 423-434.

[103] C. Ahn, J. Cheon, S. Joo, J. Kim. Effects of ionomer content on Pt catalyst/ordered mesoporous carbon support in polymer electrolyte membrane fuel cells. Journal of Power Sources 222 (2013) 477e482

[104] Joo, S. H., C. Pak, et al. (2006). "Ordered mesoporous carbons (OMC) as supports of electrocatalysts for direct methanol fuel cells (DMFC): effect of carbon

precursors of OMC on DMFC performances." Electrochimica Acta 52(4): 1618-1626.

[105] Nores-Pondal, F., I. Vilella, et al. (2009). "Catalytic activity vs. size correlation in platinum catalysts of PEM fuel cells prepared on carbon black by different methods." International Journal of Hydrogen Energy 34(19): 8193-8203.

[106] Yoshitake, T., Y. Shimakawa, et al. (2002). "Preparation of fine platinum catalyst supported on single-wall carbon nanohorns for fuel cell application." Physica B: Condensed Matter 323(1): 124-126.

[107] Antolini, E. (2003). "Formation, microstructural characteristics and stability of carbon supported platinum catalysts for low temperature fuel cells." Journal of materials science 38(14): 2995-3005.

[108] Larsen, M. J. and E. M. Skou (2012). "ESR, XPS, and thin-film RRDE characterization of nano structured carbon materials for catalyst support in PEM fuel cells." Journal of Power Sources 202: 35-46.

[109] Antolini, E. (2009). "Carbon supports for low-temperature fuel cell catalysts." Applied Catalysis B: Environmental 88(1): 1-24.

[110] Rivin, D. (1969). Sulfonated carbon blacks, United States Patent.

[111] Aboytes, P. (1970). Sulfonated carbon black, United States Patent.

[112] Kitano, M., K. Arai, et al. (2009). "Preparation of a sulfonated porous carbon catalyst with high specific surface area." Catalysis Letters 131(1-2): 242-249.

[113] Hung, T., S. Liao, et al. (2011). "Effect of sulfonated carbon nanofiber-supported Pt on performance of Nafion based self-humidifying composite membrane for proton exchange membrane fuel cell." Journal of Power Sources 196(1): 126-132.

[114] Wang, H., H. Yu, et al. (2006). "Methanol electrocatalytic oxidation on highly dispersed Pt/sulfonated-carbon nanotubes catalysts." Electrochemistry Communications 8(3): 499-504.

[115] Du, C., T. Zhao, et al. (2008). "Sulfonation of carbon-nanotube supported platinum catalysts for polymer electrolyte fuel cells." Journal of Power Sources 176(1): 9-15.

[116] Sun, Z.-P., X.-G. Zhang, et al. (2008). "A simple approach towards sulfonated multi-walled carbon nanotubes supported by Pd catalysts for methanol electro-oxidation." Journal of Power Sources 185(2): 801-806.

[117] Sun, Z.-P., X.-G. Zhang, et al. (2009). "Sulfonation of ordered mesoporous carbon supported Pd catalysts for formic acid electrooxidation." Journal of colloid and interface science 337(2): 614-618.

[118] Kim, H., W. Lee, et al. (2007). "Functionalized carbon support with sulfonated polymer for direct methanol fuel cells." Electrochimica Acta 52(7): 2620-2624.

[119] Pozio, A., M. De Francesco, et al. (2002). "Comparison of high surface Pt/C catalysts by cyclic voltammetry." Journal of Power Sources 105(1): 13-19.

[120] Navessin, T., S. Holdcroft, et al. (2004). "The role of membrane ion exchange capacity on membrane| gas diffusion electrode interfaces: a half-fuel cell electrochemical study." Journal of Electroanalytical Chemistry 567(1): 111-122.

[121] Géniès, L., Y. Bultel, et al. (2003). "Impedance study of the oxygen reduction reaction on platinum nanoparticles in alkaline media." Electrochimica Acta 48(25): 3879-3890.

[122] Burgess, K. S. D., J. W. Kable, et al. (1999). "Rotating disk electrode voltammetry applied to the kinetics of uptake and efflux in wild-type and mutant catecholamine transporters." Electroanalysis 11(5): 337-343.

[123] Catlin, G., S. G. Advani, et al. (2011). "Optimization of polymer electrolyte membrane fuel cell flow channels using a genetic algorithm." Journal of Power Sources 196(22): 9407-9418.

[124] http://www.scientific-computing.com/features/feature.php?feature_id=126

[125] http://www.futureenergies.com/modules.php?op=modload&name=News&file=article&sid=959

[126] Franck-Lacaze, L., C. Bonnet, et al. (2009). "Effects of ozone on the performance of a polymer electrolyte membrane fuel cell." Fuel Cells 9(5): 562-569.

[127] Franck-Lacaze, L., C. Bonnet, et al. (2010). "Ageing of PEMFC's due to operation at low current density: Investigation of oxidative degradation." International Journal of Hydrogen Energy 35(19): 10472-10481.

[128] Weissmann, M., S. Baranton, et al. (2010). "Modification of hydrophobic/hydrophilic properties of Vulcan XC72 carbon powder by grafting of trifluoromethylphenyl and phenylsulfonic acid groups." Carbon 48(10): 2755-2764.

[129] Hyde, T. (2008). "Final Analysis: Crystallite Size Analysis of Supported Platinum Catalysts by XRD." Platinum Metals Review 52(2): 129-130.

[130] Williams, D. B. and C. B. Carter (1996). The Transmission Electron Microscope, Springer.

[131] Inaba, M., T. Kinumoto, et al. (2006). "Gas crossover and membrane degradation in polymer electrolyte fuel cells." Electrochimica Acta 51(26): 5746-5753.

[132] Kocha, S. S., J. Deliang Yang, et al. (2006). "Characterization of gas crossover and its implications in PEM fuel cells." AIChE journal 52(5): 1916-1925.

[133] Baik, K. D., I. M. Kong, et al. (2013). "Local measurements of hydrogen crossover rate in polymer electrolyte membrane fuel cells." Applied Energy 101: 560-566.

[134] Wu, J., X. Z. Yuan, et al. (2008). "Diagnostic tools in PEM fuel cell research: Part I Electrochemical techniques." International Journal of Hydrogen Energy 33(6): 1735-1746.

[135] Wang, H., X.-Z. Yuan, et al. (2011). PEM fuel cell diagnostic tools, CRC press.

[136] Hitz, C. and A. Lasia (2001). "Experimental study and modeling of impedance of the her on porous Ni electrodes." Journal of Electroanalytical Chemistry 500(1): 213-222.

[137] Chatillon, Y. (2013). Méthodes électrochimiques pour la caractérisation des piles à combustible de type PEM en empilement. Nancy, Lorraine University. Doctor.

[138] Huang, B. (2012). Mécanismes de vieillissement de l'Assemblage-Membrane-Electrodes dans une pile à combustible de type PEM par approche expérimentale. Nancy, Lorraine University. Doctor.

[139] Lapicque, F., C. Bonnet, et al. (2012). "5 Analysis and Evaluation of Aging Phenomena in PEMFCs." Advances in Chemical Engineering 41: 265.

[140] Garland, N., T. Benjamin, et al. (2007). "DOE fuel cell program: durability technical targets and testing protocols." ECS Transactions 11(1): 923-931.

[141] Y. Xia, T.-T. Nguyen, et al. (2014). "Development of half-cells with sulfonated Pt/Vulcan catalyst for PEM fuel cells." Journal of Electroanalytical Chemistry 724: 62-70.

[142] L. Giorgi, E. Antolini, et al. (1998). "Influence of the PTFE content in the diffusion layer of low-Pt loading electrodes for polymer electrolyte fuel cells." Electrochimica Acta 43: 3675-3680

[143] Weast, R. C., M. J. Astle, et al. (1985-1986). CRC handbook of chemistry and physics, CRC press Boca Raton, FL.

Carbone fonctionnalisé pour une meilleure performance des piles à combustible

Dans le contenu de l'amélioration des performances des piles à combustible, des catalyseurs Pt/Vulcan ont été greffés soit avec du polystyrène sulfonate (PSSA) soit avec de l'acide 4-phenysulfonique (PSA). L'influence du ratio du greffage, de la couche de diffusion de gaz et de la qualité de Nafion, sur les performances électrochimiques ont été étudiées en demi-pile et en assemblage membrane-électrodes (AME). La surface électrochimique du catalyseur a été améliorée en présence de la couche microporeuse sur le papier carboné en tant que couche de diffusion de gaz, aussi une densité de courant supérieure et une résistance de transfert de charge inférieure ont été observées. Pt/Vulcan catalyseurs ont été greffés des chaines PSSA avec 5, 10 et 20 wt.% 4-styrènesulfonate de sodium. Les résultats en demi-pile et en pile ont montré que des taux de sulfonation de 5 à 10 wt.% étaient optimaux. La sulfonation des catalyseurs a aussi été effectuée avec 5.8, 11.6, 18.0 et 23.3 wt.% PSA. Des résultats meilleurs ont été obtenus par la sulfonation. L'AME ayant 18.0 wt.% PSA a présenté une excellente stabilité pendant 3000 cycles de test de vieillissement accéléré. Moins de Nafion a entraîné une plus faible performance des demi-piles, aussi des AMEs ayant catalyseurs des greffé de 5 wt.% PSSA ou PSA. Cependant, celles contenant 10 et 20 wt.% de PSSA, ont montré un une densité de puissance élevé lors que la quantité de Nafion a diminué de 0.50 à 0.25 $mg{\cdot}cm^{-2}$.

Mots-clés: Piles à combustible, Demi-pile, Catalyseurs, Carbone sulfoné, Vieillissement

Functionalized carbon materials for higher performances of PEM fuel cells

In the development of the performances of PEM fuel cell, sulfonated Pt/Vulcan catalysts were prepared by grafting with either polystyrene sulfonate (PSSA) or with 4-phenysulfonic acid (PSA). The influences of the graft ratio, the amount of Nafion and the gas diffusion layer, on the electrochemical performances were studied in a half-cell and membrane electrode assemblage (MEA). Larger electrochemical surface area of the catalyst was obtained in the presence of microporous layer on the carbon paper, as well as higher ORR current and lower charge transfer resistance. PSSA was grafted onto Pt/Vulcan catalysts by in-situ radical polymerization with 5, 10 and 20 wt.% sodium styrene sulfonate. It was presented in the half-cell tests and fuel cell tests that the catalysts grafted with 5 and 10 wt.% sulfonated groups performed improved properties. Pt/Vulcan catalysts were also grafted with 5.8, 11.6 18.0 and 23.3 wt.% PSA. Compared with non-functionalized catalysts, significant developments were achieved because of the sulfonation. The MEA with 18.0 wt.% PSA was studied in accelerated durability tests and showed excellent durability after 3000 cycles. For half-cells and MEAs with catalysts grafted with 5 wt.% PSSA or PSA groups, low Nafion addition resulted in lower performances. However, the MEAs with 10 and 20 wt.% PSSA exhibited an enhanced performance than the counterparts with 0.50 $mg{\cdot}cm^{-2}$ Nafion.

Keywords: Fuel cell, Half-cell , Catalysts , Sulfonated carbon, Ageing